ADVANCED MODELS FOR SLIDING SEISMIC ISOLATION AND APPLICATIONS FOR TYPICAL MULTI-SPAN HIGHWAY BRIDGES

A Dissertation
Presented to
The Academic Faculty

by

Murat Eröz

In Partial Fulfillment
of the Requirements for the Degree
Doctor of Philosophy in the
School of Civil and Environmental Engineering

Georgia Institute of Technology
December 2007

ADVANCED MODELS FOR SLIDING SEISMIC ISOLATION AND APPLICATIONS FOR TYPICAL MULTI-SPAN HIGHWAY BRIDGES

Approved by:

Dr. Reginald DesRoches, Advisor
School of Civil and Environmental Engineering
Georgia Institute of Technology

Dr. Laurence Jacobs
School of Civil and Environmental Engineering
Georgia Institute of Technology

Dr. Barry Goodno
School of Civil and Environmental Engineering
Georgia Institute of Technology

Dr. Jeffrey Streator
School of Mechanical Engineering
Georgia Institute of Technology

Dr. Donald White
School of Civil and Environmental Engineering
Georgia Institute of Technology

Date Approved: November 5, 2007

In loving memory of Russell and Wylene Sohn

ACKNOWLEDGEMENTS

I would like to express my deepest gratitude to my advisor Dr. Reginald DesRoches for the support, guidance and friendship he has extended. I would like to thank Dr. Barry Goodno, Dr. Donald White, Dr. Laurence Jacobs, and Dr. Jeffrey Streator for their time and effort in serving on my Ph.D. committee. I am grateful for the unconditional love and support of my parents. Their inspiration and guidance has made this dream a reality.

TABLE OF CONTENTS

LIST OF TABLES

LIST OF FIGURES

SUMMARY

The large number of bridge collapses that have occurred in recent earthquakes has exposed the vulnerabilities in existing bridges. One of the emerging tools for protecting bridges from the damaging effects of earthquakes is the use of isolation systems. Seismic isolation is achieved via inserting flexible isolator elements into the bridge that shift the vibration period and increase energy dissipation. To date, the structural performance of bridges incorporating sliding seismic isolation is not well-understood, in part due to the lack of adequate models that can account for the complex behavior of the isolators. This study investigates and makes recommendations on the structural performance of bridges utilizing sliding type seismic isolators, based on the development of state-of-the-art analytical models. Unlike previous models, these models can account simultaneously for the variation in the normal force and friction coefficient, large deformation effects, and the coupling of the vertical and horizontal response during motion. The intention is to provide support for seismic risk mitigation and insight for the analysis and design of seismically isolated bridges by quantifying response characteristics. The level of accuracy required for isolator analytical models used in typical highway bridges are assessed. The comparative viability of the two main isolator types (i.e. sliding and elastomeric) for bridges is investigated. The influence of bridge and sliding isolator design parameters on the system's seismic response is illustrated.

CHAPTER I

INTRODUCTION

1.1 Background

Bridges are a crucial part of the overall transportation system and their performance during earthquakes is important for continued functioning of a community. The large number of bridge collapses during the 1971 San Fernando earthquake exposed the deficiencies of the 1965 AASHTO and previous bridge design codes. There are approximately 575,000 bridges in the United States with approximately 60% having been constructed prior to 1970 with little or no consideration given to seismic resistance (Cooper et al.1994). A series of revisions to the design guidelines were accompanied by the launching of substantial retrofitting programs following the 1971 San Fernando earthquake. Until the mid-1980s, bridge retrofitting techniques in the U.S. only incorporated individualized strengthening schemes such as steel jacketing of columns, casting of in-fill walls between columns, strengthening of footings and bearing elements, widening of the pier caps and abutments, and the use of restraining cables (Yashinsky 1998). Seismic bridge design focused on increasing the lateral strength to resist inertial forces that occurred from ground shaking (Yashinsky and Karshenas 2003). However, this increase was found to be self-defeating, since strengthened members attracted larger forces that severely damaged other elements along the bridge's lateral load path.

The root cause of the damaging effects of earthquakes is the unfortunate correlation between the fundamental periods of vibration of major structures and the frequency content of the seismic input (Priestley et al. 1996). Seismic isolation decouples the structure from the horizontal components of the ground motion with elements that have a low horizontal stiffness (Naeim and Kelly 1996) (Figure 1.1).

Figure 1.1 Typical seismic isolation example in the American River Bridge at Lake Natoma in Folsom, California (courtesy of Earthquake Protection Systems, Inc.).

Isolation shifts the response of the structure to a higher fundamental period and increases the damping, thus reducing the corresponding pseudo-acceleration in the design spectrum and attracting smaller earthquake-induced forces, as illustrated in Figure 1.2. The philosophy of seismic isolation for improving earthquake resistance of a structure departs from conventional retrofit measures because the latter attempts to strengthen individual elements of bridges while the former improves structural performance by reducing the overall earthquake forces that the structure acquires.

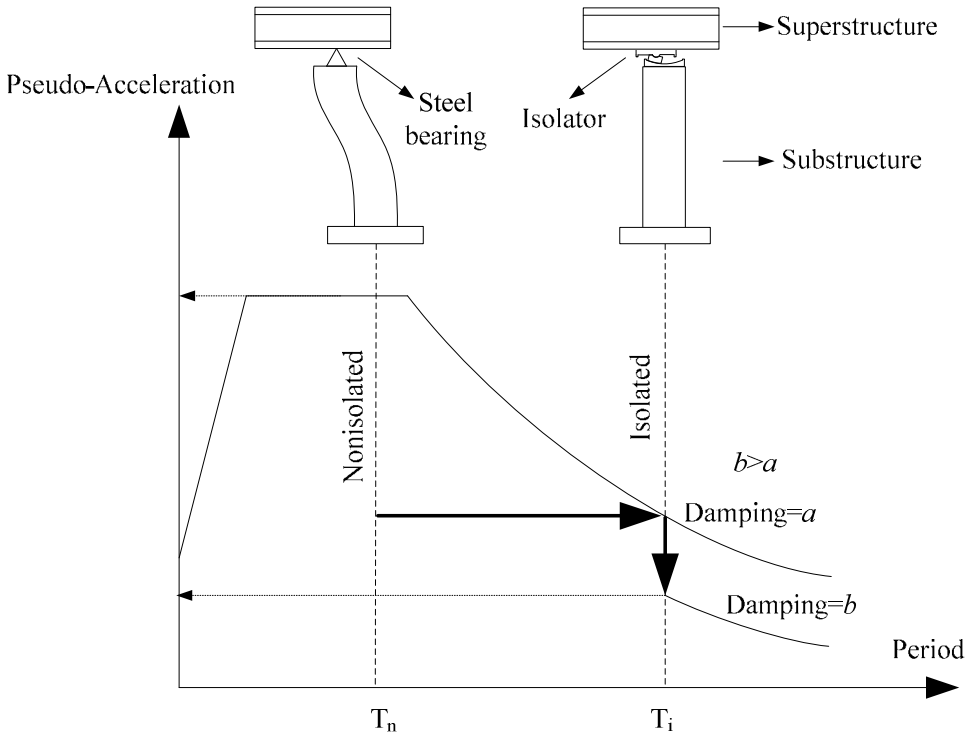

Figure 1.2 Design spectrum and the shift of spectral ordinates for an isolated structure.

Various isolators have been manufactured with the similar objective of providing a period shift and additional energy dissipation to structures. Isolators can be classified as sliding and elastomeric (Taylor and Igusa 2004; AASHTO 1999). Among others, two isolator types that are representative of sliding and elastomeric systems are the Friction Pendulum System (FPS) and the Lead-Rubber Bearings (LRB), respectively. This study focuses on the seismic response of bridges with emphasis on the FPS. The mechanism of the FPS is primarily based on its concave geometry and the surface properties. The supported structure is administered into a pendulum motion as the isolators simultaneously glide on its concave surfaces and dissipate hysteretic energy via these frictional surfaces (Dicleli and Mansour 2003).

(a) (b) (c)

Figure 1.3 The Friction Pendulum System (FPS) (a) exterior view (b) internal components (c) interior elevation.

1.2 Statement of the Problem

Bridge seismic isolation in the U.S. is a relatively new phenomenon that was addressed by the AASHTO with the Seismic Isolation Guide Specification for the first time in 1991. By this time elastomeric bearings were primarily used in bridge seismic isolation (Stanton 1998). As new isolator types became available by 1995, the first Seismic Isolation Guide Specification was essentially rewritten in 1997 to address the advances in the industry. However, the Specification still does not provide guidance about selecting the optimal isolator type for different bridge applications. Despite recent advances in base isolation research, the widespread application of this technology is still impeded by over-conservative attitudes (Mayes 2002; Naeim and Kelly 1996; Clark et al. 1999). The responses of state bridge engineers on a survey asking why base isolation is not more widely used revealed that engineers are not comfortable with seismic isolation because they view it as a black box and that there is a lack of certainty on choosing the optimum type of seismic isolation (Mayes 2002). Furthermore, sliding seismic isolators make up less than 25% of the total number of isolated bridges in North America (Buckle et al. 2006). A better understanding of the impact of isolators on the seismic behavior of bridge response is necessary.

The individual response of isolators is well understood but there are limited studies investigating the response of seismically isolated bridges (SIBs) via detailed three-dimensional (3-D) models. In particular, questions such as the relative benefits of different isolator systems for different bridge types have yet to be adequately addressed. Also, it is not clear what parameters in a typical bridge govern the effectiveness of various isolation systems. Finally, since isolators have a highly nonlinear response involving the simultaneous action of multiple components, detailed models are needed to capture the intricate behavior of these highly nonlinear elements. The influence of the level of accuracy in the modeling assumptions of isolators for bridges has received narrow attention. This thesis is aimed at addressing some of these issues.

1.3 Objectives and Scope

The objectives of this study are to assess the performance of bridges seismically isolated with the FPS, with a particular emphasis on the modeling parameters of the isolators which govern the seismic response of typical bridges. This is accomplished by developing rigorous analytical models of isolators with particular emphasis on the FPS and using these models to investigate the response of SIBs. The intention is to provide support for seismic risk mitigation and insight for the analysis and design of SIBs by quantifying response characteristics. The research tasks to accomplish these objectives are the following:

- Identify the characteristic aspects of the FPS that contribute to the force-deformation response. Develop the nonlinear kinematics formulation of the isolator model.
- Implement the model into a nonlinear dynamic evaluation platform and validate response using experimental data.

- Develop detailed 3-D bridge models isolated with the FPS and identify the influence of the modeling assumptions of the isolator on the response of the bridge.
- Modify the FPS model to represent the Lead-Rubber Bearings (LRB) force-deformation response.
- Compare and quantify the response of bridges as a function of isolator type with emphasis on FPS and LRB.
- Investigate parametrically the influence of bridge geometric and material properties, and isolator design parameters on the system's response. If applicable, propose modifications for design of the isolator to improve bridge seismic performance.

1.4 Thesis Outline

The content of the dissertation is organized into the following chapters:

Chapter 2 provides a literature review on bridge seismic isolation. Particular emphasis is given to the modeling aspects of the FPS, structural sensitivity to different modeling parameters, comparative studies among different isolators, and parametric analyses. A critical assessment of the current-state-of-the-art is presented.

Chapter 3 presents the application of seismic isolation into bridges. The dynamics of bridge seismic isolation is explained on a simplified model. Analysis methods in current Guide Specifications are outlined. An overview of common isolators is presented.

Chapter 4 explains the development of the FPS isolator model. Modeling aspects of the FPS are highlighted and the nonlinear kinematics of the response is generated. The model is incorporated into an open source finite element platform. The model is validated using experimental data.

Chapter 5 examines the response of a three dimensional (3-D) SIB as a function of FPS modeling assumptions. Friction Pendulum System (FPS) models developed with different assumptions are incorporated into bridges and subjected to time-history analyses.

Chapter 6 compares the performance of a typical bridge with elastomeric isolation versus sliding isolation. An LRB model modified from the previous FPS model is developed. The differences of the FPS and LRB response are highlighted. The responses of two bridge models isolated with each isolator are examined under time-history analyses.

Chapter 7 provides a parametric investigation on the seismic response of an FPS-isolated bridge. The response of the bridge is monitored as a function of varying design parameters.

Chapter 8 presents a summary of the research, major conclusions drawn from this study, and recommendation for future research.

CHAPTER 2

CRITICAL REVIEW OF THE CURRENT STATE-OF-THE-ART

2.1 Introduction

The introduction of seismic isolation as a practical tool has provided a rich source of experimental and theoretical work both in the dynamics of the isolated structural systems and in the mechanics of the isolators themselves. This chapter presents a summary of the previous studies that address the modeling and analysis aspects of bridge seismic isolation with particular emphasis on the Friction Pendulum System (FPS) isolator. The basics and historical development of seismic isolation is outlined. Experimental and analytical research conducted on the response characteristics of the FPS is elaborated. Analytical research aimed at comparing the two main classes of isolators, the sliding and the elastomeric, are reviewed. Parametric studies conducted on isolator and bridge design properties are summarized. A critical appraisal of the current literature is presented.

2.2 Seismic Isolation for Bridges: Basics

Recent earthquakes have illustrated the vulnerability of bridges to damage and collapse (Cooper and Friedland 1994; Yashinsky 1998). One of the emerging tools for protecting bridges from the damaging effects of earthquakes is the use of seismic isolation systems. An insightful definition of 'seismic isolation' given by Skinner et al. (1993) is as follows:

'*Seismic isolation consists essentially of the installation of mechanisms which decouple the structure, and/or its contents, from potentially damaging earthquake*

induced, ground or support, motions. This decoupling is achieved by increasing the flexibility of the system, together with providing appropriate damping.'

The two fundamental structural improvements provided by seismic isolation is the reduction of lateral forces and the concentration of lateral displacements at the isolation interface (Taylor and Igusa 2004). Seismic isolators are typically installed between piers, abutments, and deck (Priestley et al. 1996). Although patents for seismic isolation schemes were obtained as early as 130 years ago, only in the last four decades has industrial capabilities enabled the manufacturing of practical isolation devices, and only in the last decade has seismically isolated structural design been widely adopted (Taylor and Igusa 2004). Currently, isolation systems are most commonly classified as elastomeric and sliding. The fundamental concept of base isolation was first studied on an example building on balls by Professor John Milne who was a faculty member in the Mining Engineering Department of Tokyo University between 1876 and 1895 (Naeim and Kelly 1996). The first building that employed a rubber isolation system was a school at Skopje, Yugoslavia in 1969 (Naeim and Kelly 1996). The first seismically isolated building in the U.S.A. was the Foothill Communities Law and Justice Center in 1984-1985 in California, which was located only 19.3 km west of the San Andreas Fault (Taylor and Igusa 2004). The California Department of Transportation (Caltrans) was the first U.S. transportation agency to use seismic isolation on a bridge at the Sierra Point Overlook in 1985 (Taylor and Igusa 2004).

Currently seismic isolation is well-integrated into the code provisions in the U.S. for both buildings and bridges (International 2003; NEHRP 2003; AASHTO 1999; FEMA 356). However, provisions developed for seismic isolation of bridges are unique due to fundamental differences in the structural response of bridges compared to buildings. Taylor and Igusa (2004) identified the distinct properties of the structural response of bridges from that of buildings as the following:

1. Spatial variations in the ground motion may become important because bridges are long in one direction
2. Bridges are supported by flexible piers while buildings often have relatively rigid foundations
3. The flexibility of the substructure may change significantly in bridges due to the need of accommodating variations in terrain
4. Bridges are typically more flexible in the vertical direction compared to buildings because of long spans. This makes vertical ground motions important for bridges.
5. The philosophy in building isolation is to limit the forces in the superstructure while the primary concern in bridges is typically the substructure.

In addition to these factors, bridge isolators are subjected to more severe routine live load conditions than those observed in buildings and may be more exposed to environmental conditions such as, freezing, rain, sun light, salt water, and debris compared building isolators located at the foundation levels.

2.3 The Friction Pendulum System (FPS)

The Friction Pendulum System (FPS) is a sliding type seismic isolator that was developed in 1986 by Earthquake Protection Systems, Inc. (Zayas et al. 1987). The FPS was first used to retrofit an apartment building in California in 1989 (Naeim and Kelly 1996). Since than, the FPS have been used to isolate buildings (Washington State Emergency Operations Center at Camp Murray, the U.S. Court of Appeals Building in San Francisco), bridges (Benicia-Martinez Bridge in the San Francisco Bay Area, American River Bridge at Lake Natoma in Folsom), and storage tanks (LNG storage tanks on Revithoussa Island near Athens) (Jangid 2005) (Figure 2.1). The FPS has been incorporated into the design codes (AASHTO 1999; International 2000).

(a)

Figure 2.1 Applications of FPS seismic isolation at (a) Bolu Viaduct; (a) Rio Hondo Busway Bridge; (b) Kodiak-Near Island Bridge; (c) Ataturk International Airport Terminal; and (d) liquefied natural gas (LNG) storage tanks in Greece (courtesy of Earthquake Protection Systems).

(b)

(c)

Figure 2.1 continued

(d)

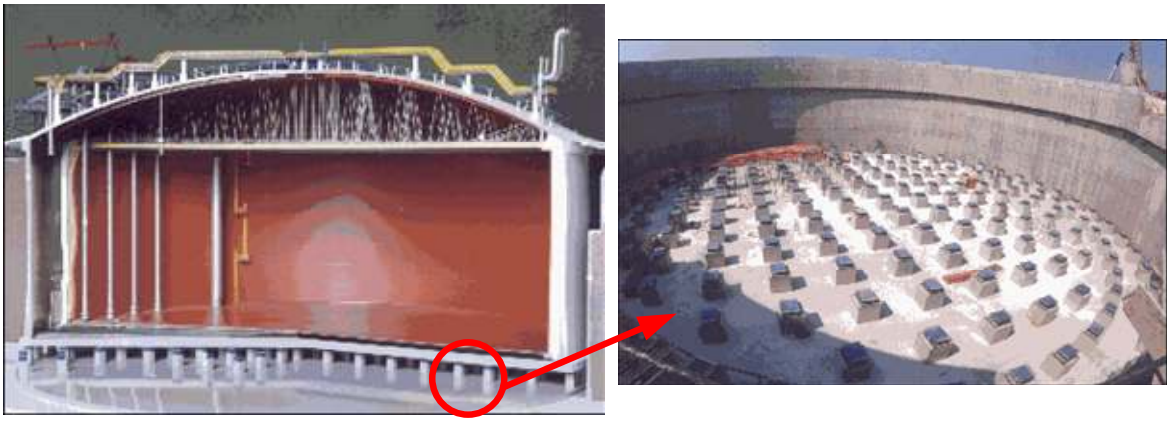

(e)

Figure 2.1 continued

The FPS consists of a spherical stainless steel surface, an articulated slider and a housing plate (Zayas et al. 1987) (Figure 2.2). The sliding surface of the FPS consists of stainless steel and a Teflon-based custom material. The radius of the FPS isolator controls the concavity related stiffness and the isolation period of the structure (Naeim and Kelly 1996). As the slider displaces over the concave surface, a continuous recentering force is provided by the gravity load of the supported mass. Simultaneously, the friction force opposes the motion of the slider and dissipates hysteretic energy.

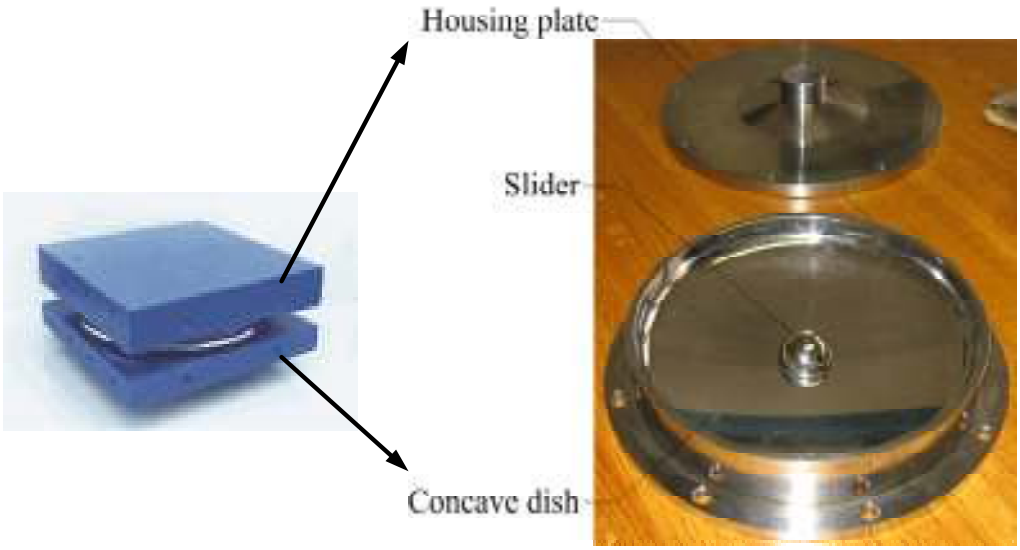

Figure 2.2 Components of the FPS.

Findings of previous research provide ample evidence that the dynamic response of seismically isolated structures is governed by the characteristics of the mechanisms of the isolators (Dicleli 2002). This is an indication that the modeling assumptions adopted for the response of the FPS will affect the estimated response quantities of SIBs. The force-deformation response of the FPS is typically modeled using a unidirectional idealization (Zayas et al. 1987):

$$f = \overbrace{N\,\mu \text{sgn}(\dot{\delta})}^{f_\mu} + \overbrace{\frac{N}{R}\delta}^{f_R} \tag{2.1}$$

where N is the normal force acting on the sliding surface, μ is the friction coefficient between the sliding surfaces, R is the radius of the concave surface, δ is the sliding deformation, $\dot{\delta}$ is the sliding velocity, and $\text{sgn}(\dot{\delta})$ is the signum function. The signum function is equal to +1 or -1 depending on whether $\dot{\delta}$ is negative or positive, respectively. The force-deformation response of the FPS is further elaborated in Chapter 4. However, it is important to underline the fundamental assumptions inherent in this equation: (1) N is constant; (2) μ is constant; (3) the horizontal response is uncoupled in the orthogonal directions; and (4) isolator deformations are small and planar. The following sections describe theoretical and experimental research performed to quantify the influence of these simplifications.

2.3.1. Normal Force, *N*

The restoring mechanism of the FPS is dependent on the normal force, N (see Equation 1). Takashi et al. (2000) identified three sources for the fluctuation of N in the isolators of bridges: (1) inertial forces due to vertical ground motions; (2) rocking behavior of the girder due to horizontal ground motion; and (3) deflection vibration of the girder due to vertical ground motion service loads and curvature (Figure 2.3).

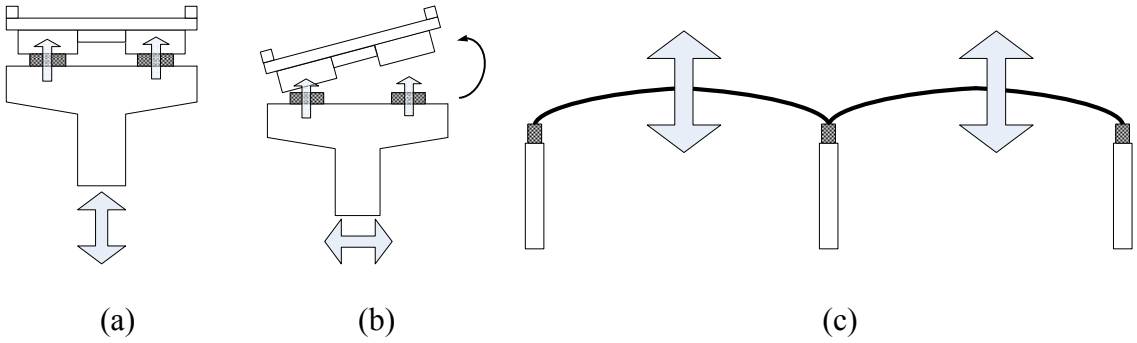

Figure 2.3 Sources of normal force, *N*, fluctuations in bridge isolators (a) vertical inertial forces (b) lateral inertial forces (c) vibration forces due to traffic.

There is a general tendency among bridge engineers to neglect the effects of vertical ground motions on the structural response (Button et al. 2002). Although the vertical components of ground motions typically have lower energy content compared to the horizontal components, the energy content is concentrated in a narrow, high frequency band which may inflict considerable structural damage (Collier and Elnashai 2001). For near-field earthquakes (<10-15 km), the vertical spectra may significantly exceed the horizontal spectra for short periods (Silva 1997). This is illustrated in Figure 2.4 for the Gazli record taken 3 km from the source. Button et al. (2002) reported that the vertical component of the earthquake may be consequential for bridges located within 60 km of the source.

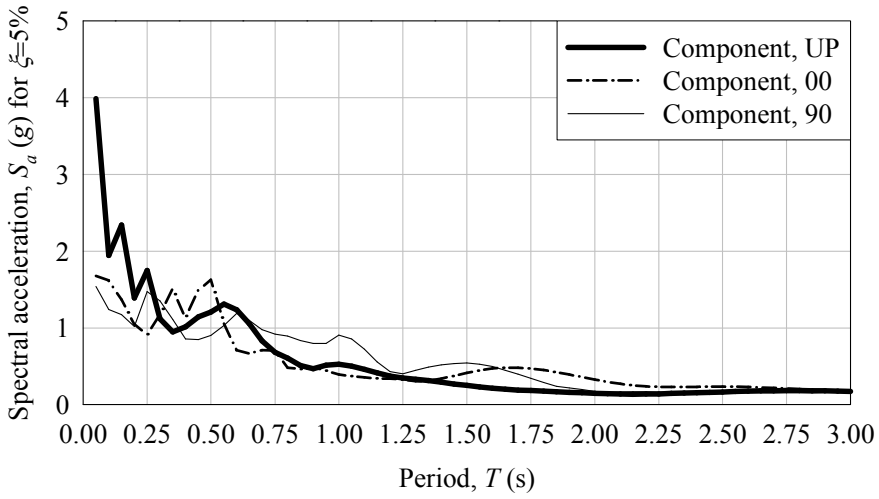

Figure 2.4 Response spectra for Gazli (1976) earthquake record.

Serious substructure damage was observed in bridges during the Northridge and Kobe earthquakes (Papazoglou and Elnashai 1996) (Figure 2.5). It was shown that the design values for dynamic response increases for bridge members with the inclusion of the vertical components of the ground motions (Gloyd 1997; Yu 1996). However, structural damage was noted in bridge members only at relatively high magnitudes of accelerations in the vertical direction. For example, Saadeghvaziri (1991) concluded that considerable damage would occur in columns if the vertical component of the ground motions exceeded 0.7g.

Figure 2.5. Compression failure and bulging of piers along bent 3. Bull Creek Canyon Channel Bridge. Photograph courtesy of Earthquake Engineering Research Institute (Papazoglou and Elnashai 1996).

The aforementioned studies focus on non-isolated bridges. Since structures are inherently stronger and stiffer in the vertical direction compared to the horizontal directions, they are normally not isolated from vertical earthquake motions (Taylor and Igusa 2004). However, theoretical and experimental evidence suggests that the horizontal response of the FPS is coupled with the vertical response. Takashi et al. (2000) performed shaking table tests on a girder model supported by a set of four frictional isolators and two rubber buffers to assess the dependency of the structural response to vertical and horizontal excitations. The authors reported that although the rocking of the structure altered the normal force and behavior of individual isolators, it did not have considerable influence on the overall response. Takashi et al. mentioned that the sum of the areas of the hysteretic loops for cases with and without vertical ground motion was acutely similar, and concluded that the effect of vertical ground motion on the overall response was trivial. The authors have imposed vertical ground motion five times higher than that of initial test input to assess the effects of extremely large vertical

ground motion on the response. Takashi et al. reported that a loss of normal force on the isolators emanated, but the overall horizontal response did not languish even under extremely large vertical ground motions.

Nakajima et al. (2004) performed pseudo-dynamic tests to verify the effect of vertical motions on the response of sliding isolators. The experimental setup consisted of a sliding bearing that generated friction damping and of a rubber bearing that provided restoring force. The authors concluded that although the friction coefficient of the bearings alternated as a function of the bearing pressure, the effect of vertical motion was inconsequential in the overall response. It was observed that the friction coefficient increased proportionally with the sliding velocity and virtually flattened after exceeding a certain velocity. The authors stated that the friction coefficient decreased linearly with increasing bearing pressure.

Mosqueda et al. (2004) performed unidirectional and tri-directional tests on a rigid-block frame supported by four FPS. The authors concluded from the results of the tri-directional tests that the vertical component of the ground motion had negligible effect on the force-deformation response of the FPS. However, the authors noted that rotation of the superstructure in bridges caused by lateral ground motions could significantly influence the behavior of FPS.

Almazan et al. (1998) generated the exact analytical equations of motions for the FPS, which considered the large deformation effects. The authors analyzed four-story building models under horizontal and vertical ground motion. It was concluded that the global response of the structure might be estimated within the vicinity of 20% error if vertical motions are disregarded. The authors further mentioned that uplift occurred at several instants of the response and column base shears were 3 times larger when vertical motion is considered.

Dicleli (2002) performed modal and nonlinear time-history analyses on a six span slab-on-girder deck isolated with the FPS. Analysis results showed that the first modes

of vibrations were those involving the isolation system, with Modes 1, 2 and 4 being the transverse modes of vibration and mode 3 being the longitudinal. In the longitudinal direction, all isolator were found to have a uniform displacement due to the large axial rigidity of the deck in this direction. However, in the transverse direction, bearing displacements varied along the bridge caused by the unusual flexibility of the bridge in his direction. Furthermore, the dead load reactions at the abutments were only 20% of those at the piers due to smaller tributary weight of shorter end spans and uplift reactions created by much longer adjacent spans. Since the lateral resistance of the FPS is directly proportional to the dead load reactions acting on the bearings, a very small equivalent stiffness was obtained at the abutments. This was found to produce even larger bearing displacements as the seismically induced forces acquired the shape of the deflected structure. Although the abutments were structurally stronger than the piers due to their massive size, only 7% of the total seismic force was transferred to the abutments. It was concluded that hybrid isolation of the bridge using FPS and laminated elastomeric bearings produced results that are more favorable than the bridge isolated with FPS alone.

Iemura et al. (2005) performed shake table tests on scaled models of two highway bridges seismically isolated with a combined rubber and sliding bearings, a system referred as 'resilient sliding isolation (RSI)' (Figure 2.6). The objective was to quantify the effects of the vertical accelerations and rocking of the deck on sliding isolators. The authors concluded that the rocking motion had considerable effect on the individual response of the RSI however this effect was dampened in the response of the total system.

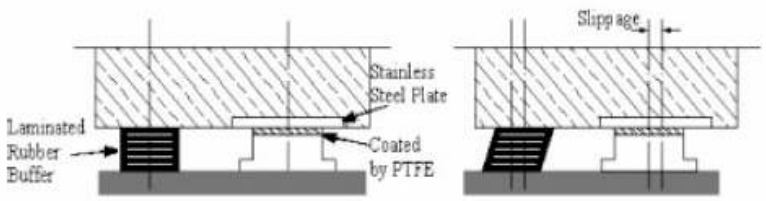

Figure 2.6 Resilient sliding isolation (RSI) (Iemura et al. 2005).

2.3.2. Coefficient of Friction, μ

Sliding isolators typically employ interfaces of steel and Polytetrafluoroethylene (PTFE or Teflon) (Mokha et al. 1991). Teflon is extremely resistant to attack by corrosive reagents or solvents (Billmeyer 1984). Furthermore, this polymer is not hard, but is slippery and waxy to touch, and has very low coefficient of friction on most substances. For all practical purposes the polymer is completely unaffected by water. Its thermal stability is such that its mechanical properties do not change for long intervals (months) at temperatures as high as $250^{o}\mathrm{C}$. Resistance to wear and to deformation under load, stiffness, and compressive strength of Teflon can be enhanced by the use of different fillers such as glass fibers, graphite, carbon and bronze. The sliding of the two surfaces of the FPS is an integral part of the force-deformation response.

Mokha et al. (1990) underlined the absence of experimental data on the sliding response of Teflon surfaces for velocities that are of interest to seismic isolation bearings. The authors performed experiments to investigate the characteristics of the steel-Teflon sliding surfaces (Figure 2.7). The following conclusions were made from the test results:

1) The coefficient of friction increases and reaches a flat plateau beyond a certain point with increasing velocity (Figure 2.8).

2) Sliding initiates at initial motion of the isolator and motion reversals (stick-slip). The magnitude of the static friction coefficient attained at these instances is substantially larger than the magnitude during sliding.
3) The magnitude of the friction coefficient reduced with increasing normal force acting on the plane of the sliding motion.
4) The effect of the dwell of the load, acceleration of the ground motion, and the specimen size is negligible to the magnitude of the coefficient of friction

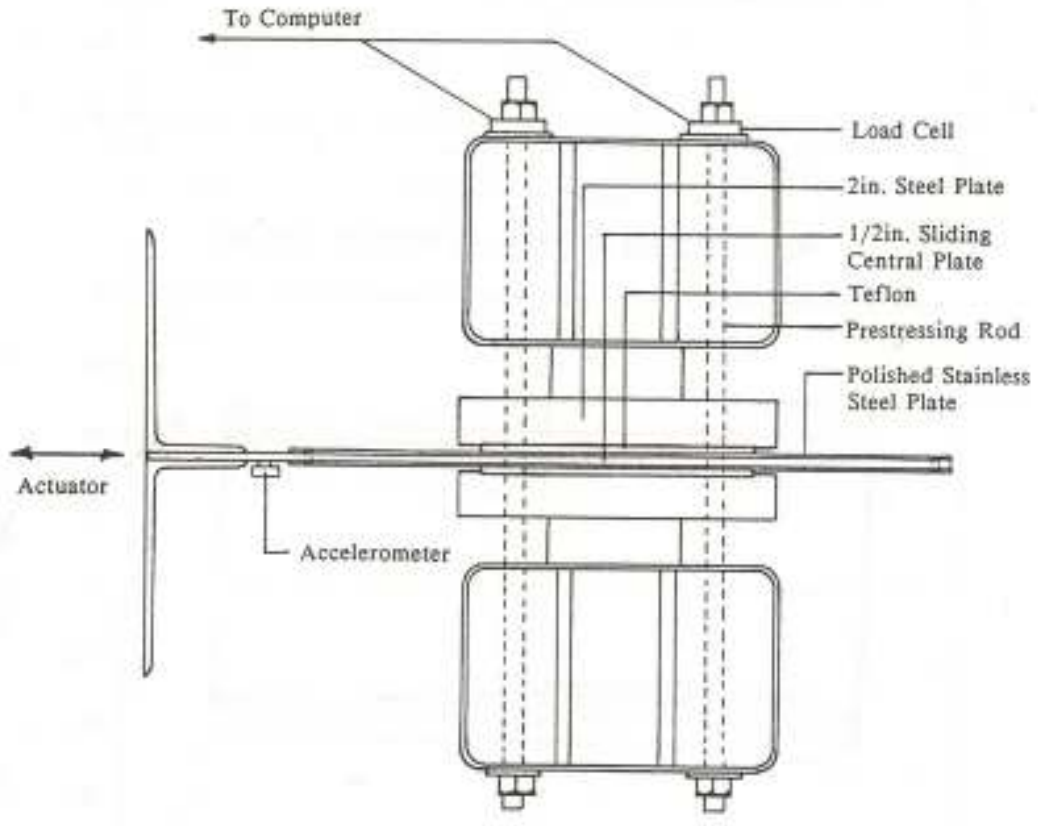

Figure 2.7 Test setup for Teflon-steel sliding surfaces (Mokha et al. 1990).

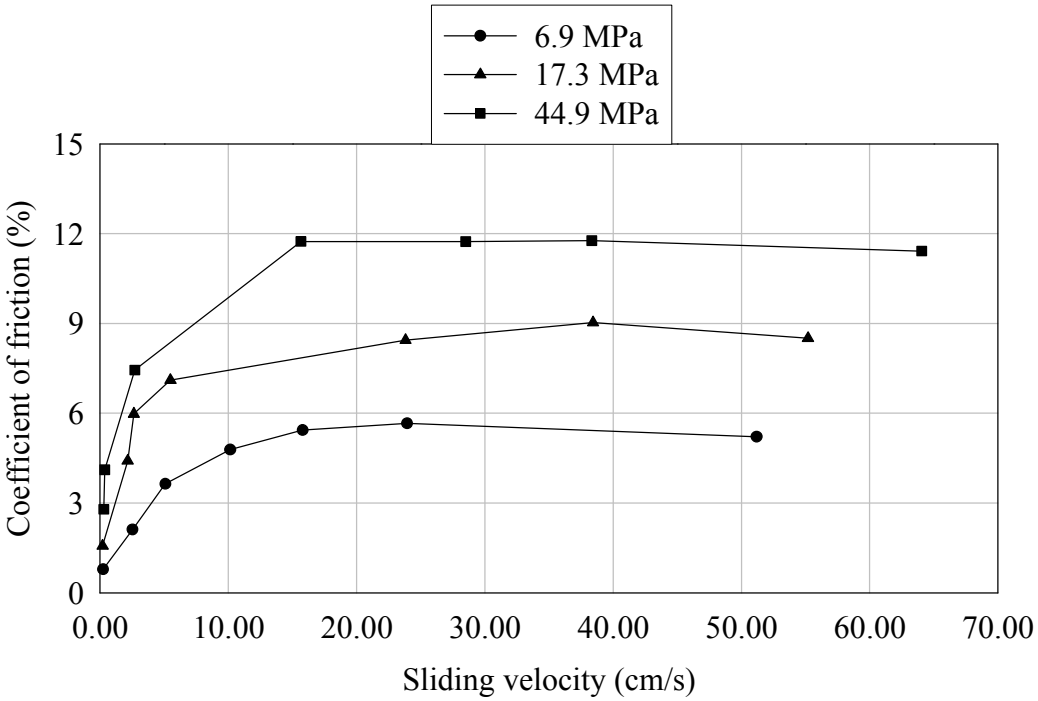

Figure 2.8 Dependency of the coefficient of friction on sliding velocity (Mokha et al. 1990).

Mosqueda et al. (2004) examined the effect of sliding velocity on the coefficient of friction by tests performed on four FPS isolators under a rigid frame that was subjected to bidirectional load histories. The velocity dependence of the coefficient of friction was similar to the one depicted by Mokha et al. (1990) with the exception of a slight decrease after 25.4 cm/s. The authors associated the reduction of the friction coefficient at high velocities with the escalation of the temperature, and the deposition of the composite material on the stainless steel surface. Test results showed that the steady state response of the friction coefficient started to develop after 2.54 cm/s, which was earlier than 12.7 cm/s reported by Mokha et al. (1990). The authors concluded this steadiness favorable for describing the coefficient of friction as a constant value postulated by the Coulomb's law of friction.

Jangid (2004) performed a parametric study to ascertain the effect of the friction coefficient of FPS on the seismic response of buildings and bridges to near-fault ground motions. The author analyzed a multi-storey building model and a three span continuous deck bridge model under near fault ground motions. Jangid (2004) concluded from the analyses that there exists an optimum value of the coefficient of friction for the FPS that reduces isolator displacements, which simultaneously minimizes the superstructure acceleration. The bridge model revealed similar results to those obtained for buildings which implied the presence an optimum value for the friction coefficient of the FPS that minimizes pier base shear and deck accelerations. The author suggested the use of coefficient of friction values between 0.07 and 0.19 for bridge isolators, and 0.05 to 0.15 for building isolators where the near-fault ground motions are expected.

Nakajima et al. (2000) analyzed a one degree-of-freedom model with a natural period equivalent to their test setup. The authors stated that omitting the variation of the friction coefficient as a function of the velocity in the modeling process caused inconsistency with experimental results.

2.3.3 Bidirectional Coupling

Available earthquake records indicate that the horizontal ground motions are two dimensional (PEER 2000). Theoretical studies have confirmed that there exists significant coupling between the orthogonal components of the response in structures that extend into the nonlinear range. Mokha et al. (1993) showed that neglecting the orthogonal coupling of the steel-Teflon interfaces in models results in underestimation of displacements and overestimation of forces. Similar theoretical and experimental research performed with the FPS confirmed these findings.

The AASHTO Guide Specifications (1999) provide a method for estimating effects of bidirectional input by combining 100% plus 30% of orthogonal maxima. Warn and Whittaker (2004) performed nonlinear time-history analyses on an FPS-isolated

bridge model to quantify the effect of bidirectional excitation and reviewed the accuracy of the AASHTO Guide Specifications (1999) estimating maximum isolator displacements. The authors concluded that bidirectional excitation produces significantly larger isolator displacements than unidirectional excitation. The authors associated these results with two factors, namely, the orthogonal component of excitation and the coupled behavior of seismic isolators. It was concluded that the AASHTO Guide Specifications (1999) procedures underestimate the isolator deformations. Anderson and Mahin (2004) analyzed generalized bridge models to asses the accuracy of the AASHTO Guide Specifications (1999) method to account for bidirectional response effects and reached similar conclusions with Warn and Whittaker (2004).

Mosqueda et al. (2004) performed unidirectional and tridirectional tests on a rigid-block frame supported by four FPS and examined how different mathematical models conjectured the response of these bearings under different excitations. The authors underlined that unidirectional tests overestimate the reduction of the friction coefficient because the friction is computed from the motion over an invariable path that accumulates the temperature. The authors stated that the bearings of full-scale bridges abide a chaotic bidirectional path that endures lower temperatures and consequently higher friction coefficients.

2.3.4 Large Deformation Effects

The large deformation aspects pertaining to FPS seismic isolation have been theoretically addressed by Almazan and Llera (2002). The authors later cast the nonlinear kinematic equations of the FPS response into an element format (Almazan and LLera 2003). The authors reported that large deformation effects in the FPS was influential on individual isolator response rather than the substructure response. It was also noted that the orientation of the FPS was a controlling parameter in transferring large deformation moments to the substructure or superstructure.

2.3.5 Other Parameters

The dynamic performance characteristics of FPS, specifically, stiffness, damping and energy dissipation was found to have relatively low sensitivity to temperature extremes (Zayas and Stanley 1999; HITEC 1998). The performance of the isolators did not change at $49^{o}\mathrm{C}$ and $-40^{o}\mathrm{C}$. Fatigue tests performed by 10,000 cycles of service movements showed that deterioration from fatigue and wear was not evident (HITEC 1998). Test results showed that the FPS was mildly frequency dependent. The stiffness and energy dissipation characteristics of the FPS generally increased with increasing periods of the excitation.

2.4 Comparative Studies

Seismic isolators serve the common objective of decoupling the structure from the horizontal components of the ground motion to minimize the seismic loads on the load-carrying components. However, there exist considerable differences in the vertical response characteristics of elastomeric and sliding isolators. The Lead-Rubber Bearing is a widely used elastomeric isolator (Buckle and Mayes 1990). The details of the LRB characteristics are elaborated in Chapters 3 and 6. The conventional FPS is essentially rigid under compression and has no tensile load capacity while the LRB has relatively less compression stiffness and able to resist a limited amount of tensile loading (Kelly 2003; Almazan et al. 1998; Naeim and Kelly 1996). Both the post-yield stiffness and the yield force of the two types of isolators are known to be affected by the normal force being imposed, but at a different rate and form (Almazan et al. 1998; Ryan and Chopra 2003). Normal force-dependent FPS models have been developed previously to show that this effect may result in considerable variation on the estimated isolator response (Almazan et al. 1998). However, LRB models that account for bi-directional coupling

has not yet been extended to account for normal force-dependency and implemented in bridge analyses to the authors` knowledge. High variation of the normal loads may result in fracture and a considerable change in the horizontal response of the isolators (Priestley et al. 1996). It has been shown that excluding the in-plane coupling of the orthogonal response for the isolators may result in significant underestimation of the displacements and forces for both type of isolators (Mosqueda et al. 2004; Jangid 2004). The bilinear force-deformation idealization of isolators allowed by the Specifications is based on the assumptions that the response is unidirectional and the normal force acting on the isolators is constant. Consequently, the unique response of the isolators may not be adequately captured with this simplified modeling approach.

Dicleli and Buddaram (2005) compared the response of an idealized bridge substructure utilizing seismic isolation devices that have the characteristic stiffness values of lead-rubber, high damping rubber and friction-based bearings. The authors highlighted that the peak isolator displacements decrease and forces increase as the post-yield stiffness of isolators increase. The effects of post-yield stiffness on isolator response were more pronounced for ground motions with low frequency content. Initial stiffness of the isolators was noted to have negligible affects on the seismic response.

Matsagar and Jangid (2004) analyzed the effects of different yield displacement and yield force properties in bilinear force-deformation models of elastomeric and friction isolators for a multi-story building model. A higher yield displacement resulted in substantial decrease in peak superstructure accelerations and marginal increase in bearing displacement. An increase of the yield strength resulted in higher superstructure accelerations and lower bearing displacements. This was attributed to the structure remaining within the elastic range for a longer period of time thus decreasing the amount of energy dissipation.

Ordonez et al. (2003) investigated the earthquake response of a two-degree of freedom model as a function of different isolators. The four types of isolators were the pure friction system, the friction pendulum system, the laminated rubber isolator, and the New Zealand (lead-rubber) isolator. The authors reported base displacements in descending order as the lead-rubber isolator, the laminated rubber isolator, the pure friction system and the friction pendulum system. Ordonez et al. (2003) concluded that base displacements are smaller but inter-story drifts are larger for frictional systems compared to neoprene systems.

Barrosso et al. (2002) compared the seismic performance of three different structural control methods employed on steel frame buildings. The three schemes of structural control were the: (1) friction pendulum system; (2) linear viscous dampers; and (3) active tendon brace system. The authors identified normalized hysteretic energy and interstory drifts as a definitive measure for describing the response of the frame. It was concluded from the analysis that no control system was consistently better than another, and that they all reduced the amount of energy dissipated by the structural system and inter-story drifts to negligible values.

Jangid and Kelly (2001) analyzed a two degree-of-freedom isolated building model. The separate isolation schemes included elastic rubber isolators, the high-damping rubber bearings, the lead-rubber bearing, and Electric-de-France system under near-fault ground motions. Linear rubber and lead rubber bearings resulted in almost the same response that corresponded to larger deformations but smaller superstructure accelerations compared to other isolators. The authors concluded from the study that high-damping rubber bearings was influential in reducing bearing displacement but transmitted higher accelerations into the structure compared to other isolators. It was concluded that there existed an optimal value of isolator damping when caused higher accelerations to the superstructure exceeded. The authors showed that the Electric-de-

France acquires lower deformations compared to the rubber isolators but transmits similar accelerations to the superstructure.

Sugiyama (2000) compared the seismic response of a continuous steel box girder bridge isolated either with sliding or rubber isolation. The author reported higher superstructure accelerations with sliding isolators compared to rubber isolators for strong earthquakes, which is conversely different from the case in buildings. Additionally, the author underlined that the difference of the bridge isolated was negligible for weak earthquakes.

2.5. Parametric Studies

Studies aimed at investigating the effects of different design parameters in SIBs are limited. Ghobarah (1988) investigated the parametric effects of LRB isolator stiffness, pier stiffness and pier eccentricity on the response of SIB models. The author showed that the increase of the flexibility of piers results in an increase in the force and displacement demands at the abutments and reduced shears at the pier. The forces and displacements at the abutments became larger as the pier offset was increased. Larger elastic stiffness of the isolators reduced the deck displacements and the behavior approached to a case of hinged supports.

Ghobarah and Ali (1988) compared the response of a seismically LRB isolated and non-isolated bridge model and investigated the effects of different design parameters in the response of the SIB response. The authors parametrically quantified the error for assuming a rigid superstructure in the models in the fundamental period as a function of deck to pier stiffness ratio. It was observed that the rigid deck assumption underestimated the fundamental period and the error is more pronounced for stiffer isolators. However, the error was within the order of 6% for typical highway bridges. The authors parameterized the location of the effect of energy dissipation of the isolators throughout the bridge. Isolation schemes involving higher energy dissipation at the

abutments compared to the piers resulted in considerable reduction in the seismic forces acting on the piers. A parametric investigation of the magnitude of the yield force of isolators showed that higher yield forces result in reduced shear forces in the pier and the displacements of the deck.

Turkington et al. (1989) performed parametric analyses on a bridge seismically isolated with combined LRB and elastomeric bearings to develop a design method. This study investigated the effects of a range of isolator characteristics and the strengths of various components of the bridge on the overall response. It was concluded that as long as the isolators' yield strength remained within 4-10% of the superstructure weight, the seismic response is not significantly affected. The effectiveness of the isolators reduced considerably as the superstructure flexibility increased. Increasing the LRB height, which is equivalent to increasing the post-yield stiffness, was found to result in greater period shifts of the bridge.

Bridges may be constructed with a skew angle to accommodate traffic and site conditions. Nielson (2005) defined bridge skew, θ, as "the angle measured between the center line of the bridge supports and the line perpendicular to the bridge center line. It was also noted that a 15.3% to 53% of all the bridge types considered in the Central and Southeastern United states are skewed. An important structural aspect of skewed bridges is that their vibrational modes do not uncouple in orthogonal directions as in the case of non-skewed bridges (Maleki 2001b). Meng and Lui (2000) analyzed the response of a skew concrete box girder bridge by accounting for deck flexibility and column boundary conditions. The models of the same bridge were generated either as elastic shell elements, as rigid deck or elastic beam elements. The authors noted that large skewness may lead to torsional and lateral vibrations. Maleki (2001a) derived closed form solutions for the translational and torsional periods of skewed bridges supported on elastomeric bearings and have cross-frame diaphragms. The author showed that the

fundamental period of the bridges with elastomeric bearings increases as the skew angle increases and the second translational period is independent from the skew angle.

Dicleli et al. (2005) investigated the effects of soil-structure interaction (SSI) in SIBs using iterative multimode response spectrum analyses. This study considered two bridge types that had different superstructure and substructure weights. It was concluded that SSI effects were negligible for SIBs with heavy superstructure and light superstructure located on stiff soil. However, SSI effects were influential on isolator forces and displacements for SIBs with light superstructure and heavy substructure regardless of the stiffness of the soil.

Vlassis and Spyrakos (2001) performed parametric analyses to asses the influence of SSI on the dynamic response of a SIB pier located over shallow soil stratum overlying a rigid bedrock. The authors proposed closed form solutions to account for SSI effects in design equations used by the AASHTO. It was shown that including the SSI effects reduced the estimated base obtained from the AASHTO design procedures. Additionally, it was concluded that the fundamental period of the structure may increase substantially by accounting for SSI effects.

Thakkar and Maheshwari (1995) compared the response of a SIB model located on soft, medium and hard soil. The authors concluded that stiffer soil resulted in higher isolator forces but lower bending moments at the base of the piers.

2.6 Critical Appraisal

A review of the current state-of-the-art illustrates that the mechanism of the FPS has been thoroughly studied. The individual response of the conventional FPS has been established with experimental and analytical research. However, there are still issues pertaining to bridge seismic isolation, in particular with the FPS that need further clarification. The three main gaps in the literature were identified as the following:

1) The FPS has a highly nonlinear response that involves the variation and coupling of different parameters. Previous research considering the effects of different aspects of nonlinearities in the response of the FPS showed that there may be a significant divergence from a bilinear idealization. There is a need to develop a better understanding of the modeling assumptions and the required level of accuracy for the FPS in three-dimensional (3-D) bridge models.

2) The number of studies that compared the response of SIBs with different isolator types is limited. Available studies in this area did not consider the vertical components of ground motions, used two-dimensional structural models and idealized the force-deformation response of the isolators as bilinear which overlooked some of the distinguishing aspects of the response of the two isolator systems. There is a need for further assessment of the comparative response of SIBs via detailed isolator models that can capture the distinctions in the mechanism of sliding and elastomeric isolators.

3) Previous research on the parametric affects of design parameters in SIBs have focused primarily on bridges utilizing elastomeric systems and was generally confined to two-dimensional models that excluded the vertical components of ground motions. Further insight on the influence of design parameters in bridges isolated with the FPS is needed.

CHAPTER 3

SEISMIC ISOLATION FOR BRIDGES

3.1 Introduction

The general topic of bridge seismic isolation requires an understanding of structural analysis and dynamics, corresponding code aspects and the characteristics of the isolators. Decoupling of the structure from the horizontal components of the ground motion via an isolator results in a redistribution of seismic forces. The governing design codes present different methods of analysis for SIBs. Various isolators are available for bridges. The objective of this chapter is to elaborate on these aspects of bridge seismic isolation. The effects of seismic isolation in bridges are illustrated on a simplified bridge model via modal analysis. An outline of the analysis methods in the governing design code of bridge seismic isolation is also presented. The characteristics of most commonly used isolators in bridges are described.

3.2 General Features of a Seismically Isolated Bridge (SIB)

Typically, the primary objective of bridge seismic isolation is the protection of the piers and the foundations and in some cases the abutments (Skinner et al. 1993). This is accomplished by installing seismic isolators between the superstructure and these components. The superstructure is seldom of concern due to inherent strength in design for vehicle loads. In superstructure isolation, the substructure is not isolated from the ground motions but decoupled from the relatively larger mass of the superstructure. The effects of seismic isolation is examined through an idealized bridge structure with a lumped superstructure and substructure mass, m_1 and m_2, respectively, substructure lateral linear-elastic stiffness k_1 and isolator linear-elastic stiffness k_2. Each lumped mass is designated a lateral degree-of-freedom, u_1 and u_2 (Figure 3.1).

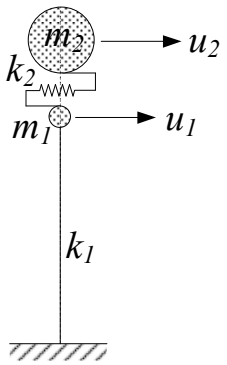

Figure 3.1 Idealized seismic-isolated bridge substructure.

The mass and the stiffness matrices of this system are:

$$\mathbf{m}=\begin{bmatrix} m_1 & 0 \\ 0 & m_2 \end{bmatrix} \tag{3.1}$$

$$\mathbf{k}=\begin{bmatrix} k_1+k_2 & -k_2 \\ -k_2 & k_2 \end{bmatrix} \tag{3.2}$$

The characteristic equation (frequency equation) is (Chopra 2000):

$$\det\left[\mathbf{k}-\omega_n{}^2\mathbf{m}\right]=0 \tag{3.3}$$

where ω_n is the natural frequency of the n^{th} mode. Given the positive definite property of **k** and **m**, the expanded form of Equation 1 has real and positive roots for $\omega_n{}^2$:

$$m_1m_2\,\omega_n{}^4+(-k_1m_2-k_2m_2-k_2m_1)\omega_n{}^2+k_1k_2=0 \tag{3.4}$$

Consider the structure to have m_1=0.70 kN-s^2/cm, m_2=0.18 kN-s^2/cm, and k_1=280.2 kN/cm. From the solution of Equation 3.4, the natural period of the n^{th} mode, T_n= $2\pi/\omega_n$, as a function of k_2/k_1 is as given in Figure 3.2. Large values of k_2/k_1 imply a rigid layer between m_1 and m_2. In this case the structure essentially reduces to a cantilever with a lumped mass at the tip and has a T_1 =0.35 s. It is observed that for values of $k_2/k_1 < 1$, there is a notable increase in the fundamental period of the structure. The effect of introducing a flexible layer to the second period is negligible. The

installation of a flexible layer, where k_2/k_1<1, is an effective approach for increasing the fundamental period of the structure with little influence on the second period.

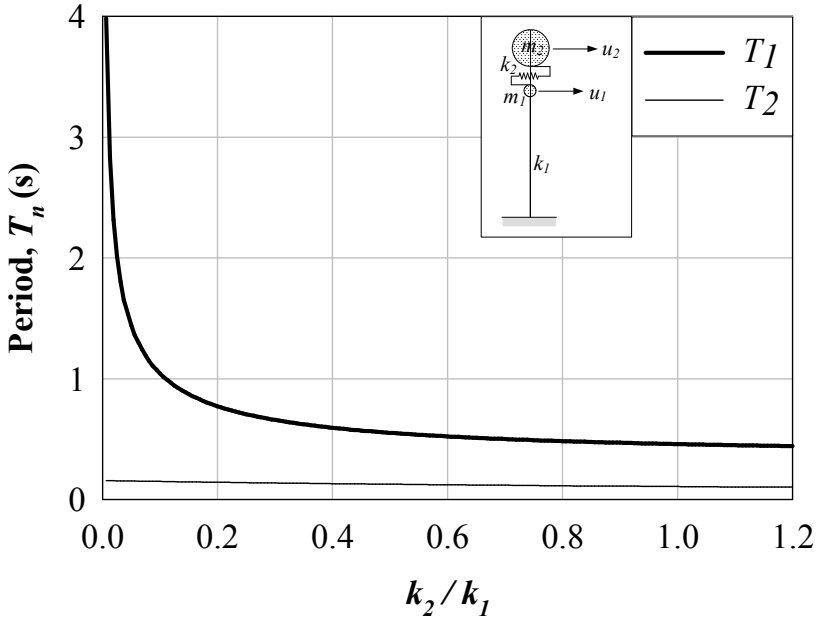

Figure 3.2 First, T_1, and second, T_2, mode structural periods as a function of k_2/ k_1 (m_1=0.70 kN-s^2/cm, , m_2=0.18 kN-s^2/cm, and k_1=280.2 kN/cm).

To highlight the dynamics of superstructure isolation, consider the system to have seismic isolation with the objective of achieving three times increase from the non-isolated period of 0.35 s. From Figure 3.2, this corresponds to approximately k_2=26.3 kN/cm in which the first two periods become T_1=1.05 s and T_2=0.15 s. The n^{th} mode shape, ϕ_n, is determined from:

$$\left[\mathbf{k} - \omega_n{}^2 \mathbf{m}\right]\phi_n = 0 \tag{3.5}$$

The solution of Equation 3.5 by assuming unit displacements at the first degrees-of-freedom in each of the two modes is given in Figure 3.3. It is observed that in the first

mode shape of the structure, the isolator undergoes significant deformation compared to the substructure. In the second mode the structural deformation is larger, however, this mode is subsequently shown to make insignificant contribution to the earthquake-induced forces of the structure, based on its low participation factor.

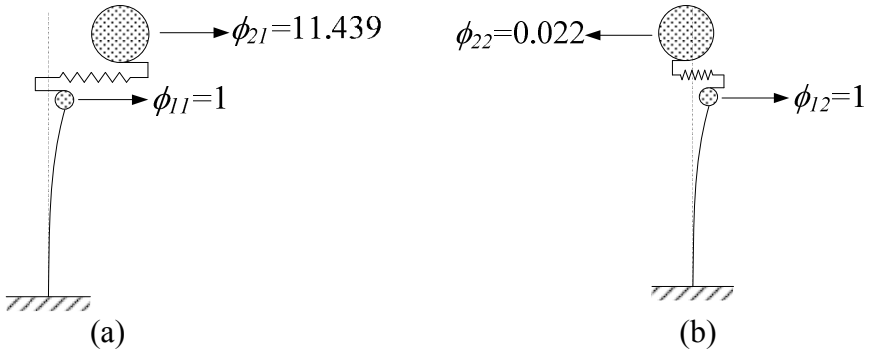

Figure 3.3 Structural shapes for (a) Mode 1 (b) Mode 2.

The spatial distribution of the effective earthquake forces are defined by :

$$\mathbf{s} = \sum_{n=1}^{N} \Gamma_n \mathbf{m} \phi_n \tag{3.6}$$

where $\Gamma_n = L_n / M_n, L_n = \phi_n^T \mathbf{mi}$, and $M_n = \phi_n^T \mathbf{m} \phi_n$, and **i** is the influence vector. The modal expansion of these forces and the modal static responses for the base shear, V_{bn}^{st}, and base moment, M_{bn}^{st}, for the n^{th} mode are given in Figure 3.4. An important implication of this result is that the first mode forces are essentially the same as the total forces. The second mode components of the static forces are negligible compared to those in the first mode. Consequently, the second mode response which involves the structural deformations is expected to make little contribution to the earthquake response of the structure.

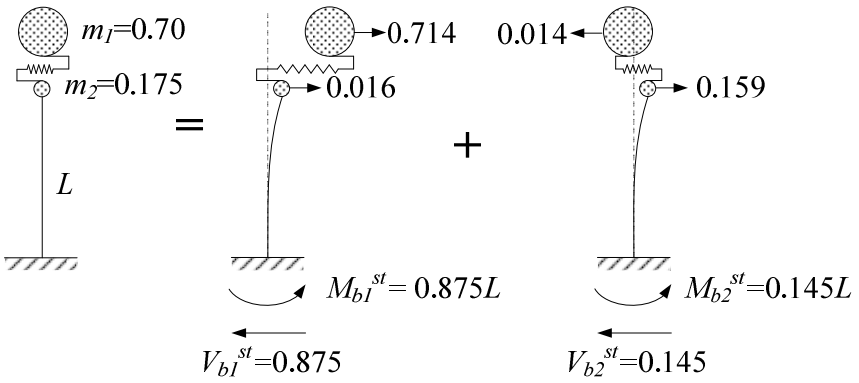

Figure 3.4 Modal expansions of effective earthquake forces and modal static responses for the base.

The earthquake response of the structure at any given time, *t*, is obtained by combining the contributions of all modes:

$$r(t) = \sum_{n=1}^{N} r_n^{st} A_n(t) \tag{3.7}$$

where r_n^{st} is the modal static response, $A_n(t) = \omega_n^2 D_n(t)$ is the pseudo-acceleration time-history and $D_n(t)$ is the displacement of the n^{th} mode. Particular interest is the peak response of the structure over the duration of the earthquake-induced response. This is obtained from:

$$r_{n\mathrm{O}} = r_n^{st} A_n \tag{3.8}$$

where A_n is the peak value of $A_n(t)$ for a particular T_n provided by a pseudo-acceleration spectrum. Consider the pseudo-acceleration design spectrum of AASHTO in the Memphis, TN region with Type II soil profile and acceleration coefficient A=0.2 (Figure 3.5).

The base shear calculation of each mode and their combination via the square-root-of-sum-of-squares (SRSS) is given in Table 3.1. Despite a larger pseudo-acceleration that corresponds to the second mode of the response, this effect is dampened

due to considerably smaller static response. The design pseudo-acceleration for the non-isolated structure corresponds to 0.5g and a peak base shear of 0.438 kN-s^2/cm. The seismic isolation scheme reduced the base shear by 72%.

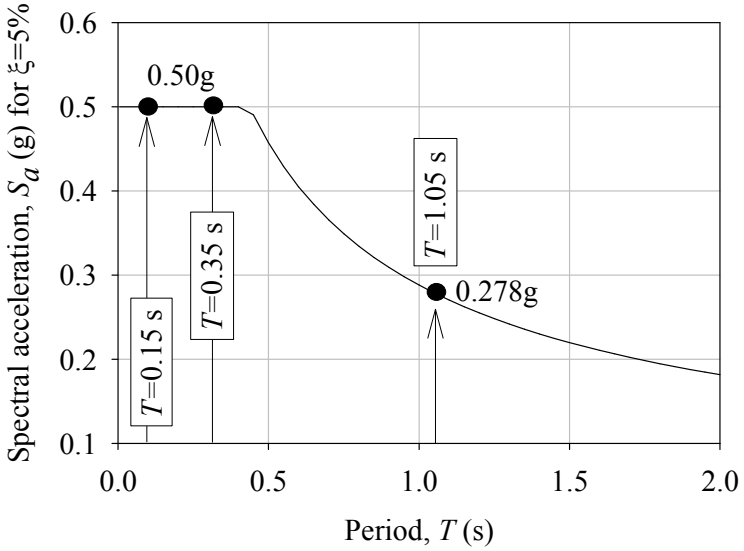

Figure 3.5 Pseudo-acceleration design spectrum for AASHTO Type II soil profile with acceleration coefficient A=0.2.

Table 3.1 Calculation of base shear

Mode	A / g	Static Base shear, V_b^{st} (kN-s^2/cm)	Peak Base shear, V_{bo} (kN-s^2/cm)
1	0.278	0.875	0.244
2	0.500	0.145	0.073
SRSS			0.255

3.3 Bridge Seismic Isolation in Design Codes

The American Association of Highway and Transportation Officials (AASHTO) Guide Specifications for Seismic Isolation Design provides the "*guide specifications for*

the seismic isolation design of highway bridges". This is a supplemental document to the AASHTO Standard Specifications for Highway Bridges Division I-A: Seismic Design. The first Seismic Isolation Guide Specification for bridges by the AASHTO was available in 1991. By this time elastomeric bearings were primarily used in bridge seismic isolation (Stanton 1998). As new designs became available by 1995 the first Seismic Isolation Guide Specification was essentially rewritten in 1997 to address the advances in the industry. Four procedures are available in the Guide Specification for the analysis of SIBs. The following is a brief overview of these procedures.

3.3.1 Procedure 1: Uniform Load Method

The Uniform Load Method is essentially the method of approximating earthquake loads with an equivalent static force. This statically equivalent seismic force is:

$$F = C_s W \tag{3.9}$$

where W is the total vertical load for design of the isolation system and C_s is the elastic seismic response coefficient computed from:

$$C_s = \frac{K_{eff} d}{W} \tag{3.10}$$

where d is the total deck displacement relative to ground and K_{eff} is the sum of the effective linear stiffnesses of all bearings and substructures. In calculating the K_{eff}, the configuration, flexibility and individual stiffnesses of the isolator units and substructure shall be taken into account:

$$K_{eff} = \sum_j \left(\frac{k_{sub} k_{eff}}{k_{sub} + k_{eff}} \right) \tag{3.11}$$

where Σ extends over all substructures, and k_{sub} is the substructure lateral stiffness and k_{eff} is the isolator unit lateral stiffness calculated at maximum displacement capacity (Figure 3.6). The displacement d (mm) is given by:

$$d = \frac{250\,AS_iT_{eff}}{B} \tag{3.12}$$

where A is the acceleration coefficient defined in Table C3-1 of the Guide Specification, S_i is the numerical coefficient per site-soil profile as defined in Table 5-1 of the Guide Specification, T_{eff} is the period of the seismically isolated structure in seconds in the direction under consideration and B is the damping coefficient.

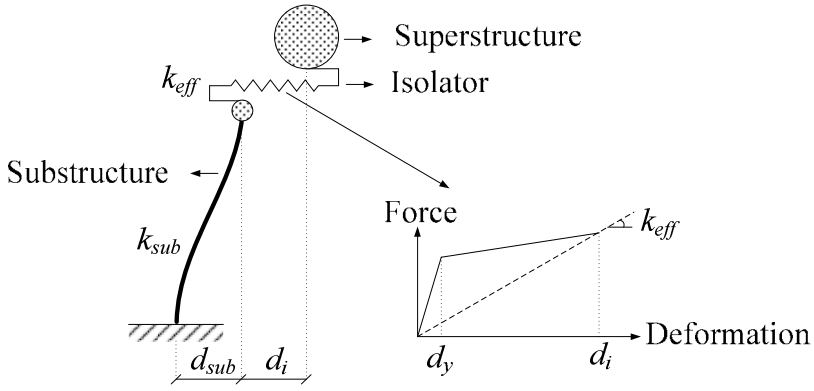

Figure 3.6 Single substructure and isolator idealization.

3.3.2 Procedure 2: Single Mode Spectral Method

The Single Mode Spectral Method is the same approach in article 4.4 of AASHTO Standard Specifications (Division I-A: Seismic Design). However, the method is simplified for SIBs due to the rigid body deformation of the superstructure. The first three steps of the procedure is devoted to finding the deflection, slope and moments in the

bridge superstructure via the double integration method. These results are used to establish the intensity of the equivalent static seismic loading applied to represent the primary mode of vibration, $p_e(x)$. For SIBs the Guide Specification Commentary C7.2 gives:

$$p_e(x) = \mathrm{w}(x)\, C_s \tag{3.13}$$

where C_s is calculated from Equation 10 and $w(x)$ is the dead-load-per-unit length of the bridge superstructure. The loading, $p_e(x)$, is used for calculating resulting member forces and displacements.

3.3.3 Procedure 3: Multimode Spectral Method

Different from the previous two procedures, the Multimode Spectral Method requires a detailed model of the bridge in a computer program. The Guide Specifications refers to article 4.5 of AASHTO Standard Specifications (Division I-A: Seismic Design) for the specifics on modeling. Isolators are modeled by their effective stiffness based on design displacements. The procedure is essentially performing an equivalent linear response spectrum analysis.

3.3.4 Procedure 4: Time-History Method

The Time History Method of analysis is the most sophisticated among the four permitted in the Guide Specification (Stanton 1998). This Procedure involves the time-history analysis of the bridge models with isolation bearings that have nonlinear deformation characteristics. The AASHTO Guide Specifications (1999) Section 7 on Analysis Procedures states that: *"To simplify the nonlinear behavior of the isolator unit, a bilinear simplification may be used"*. This bilinear hysteretic model is characterized by the elastic stiffness, k_u, post-elastic stiffness, k_d, characteristic strength, Q_d, yield force, F_y, and maximum bearing displacement, Δ_{max} (Figure 3.7). The bridge model is to be

subjected to the orthogonal components of no less than three ground motion records. The ground motion records may be frequency-scaled to match the characteristics of the corresponding site. The 5%-damped response spectrum is established by taking the square root of the sum of the squares of the orthogonal components of the ground motions. The maximum response parameter among the three ground motion records determines the design. If seven or more ground motions are used, than the average value of response parameter may be used for design. This method is required if the structure acquires effective periods greater than 3 seconds.

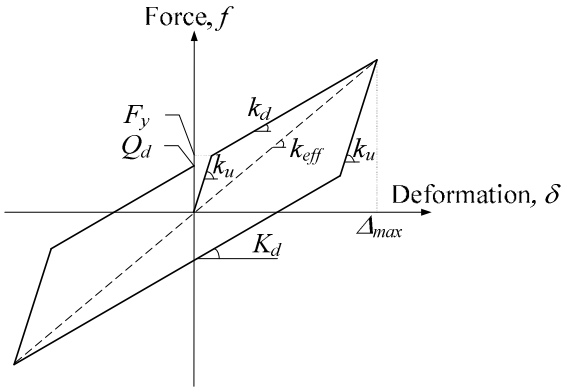

Figure 3.7 Characteristics of bilinear isolation bearings per AASHTO Guide Specifications.

3.4 Descriptions of Common Isolators

Isolators can be classified as sliding and elastomeric (Taylor and Igusa 2004; AASHTO 1999). The Guide Specifications specifically mention two isolator types from each category: Lead-Rubber and High Damping Rubber for elastomeric, and Friction Pendulum System and Eradiquake for sliding. The development of elastomeric isolators, (shown in Figure 3.8) is considered an extension of elastomeric bridge bearings and

bearings for vibration control of buildings (Naeim and Kelly 1996). These systems have become a practical tool for seismic isolation in the late 70s. Elastomeric isolators are fabricated through a process called vulcanization, which is the bonding of steel plates with rubber (HITEC).

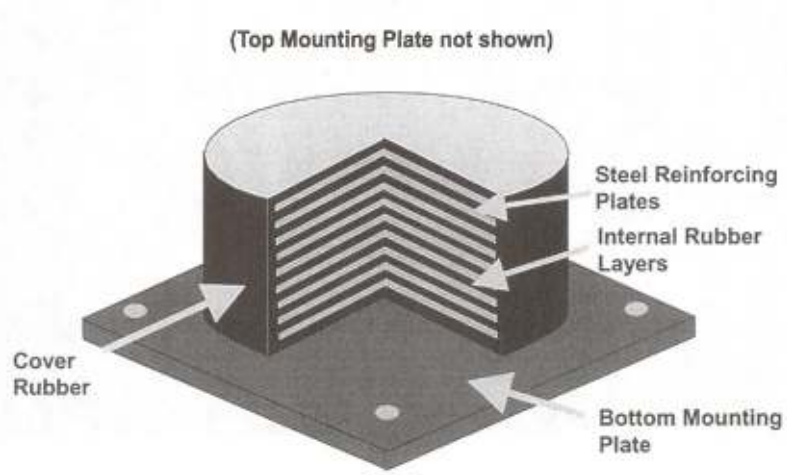

Figure 3.8 Typical elastomeric isolator (Taylor and Igusa 2004).

Sliding isolators have been modified from Teflon sliding bearings that are commonly used in bridge applications to accommodate movements from factors such as thermal expansions, creep, shrinkage or prestressing (HITEC 1998). These isolators typically possess two surfaces with different finish to slide over one another (AASHTO 1999). Naeim and Kelly (1996) noted that a purely sliding system with talc proposed by Johannes Avetican Clanterients in 1909 was the earliest seismic isolation system (Figure 3.9). However, widespread use of the sliding isolators corresponds to early 1990s. Despite the emphasis of this study on the sliding isolator FPS, a general overview of the four systems mentioned in the Guide Specifications are presented for completeness.

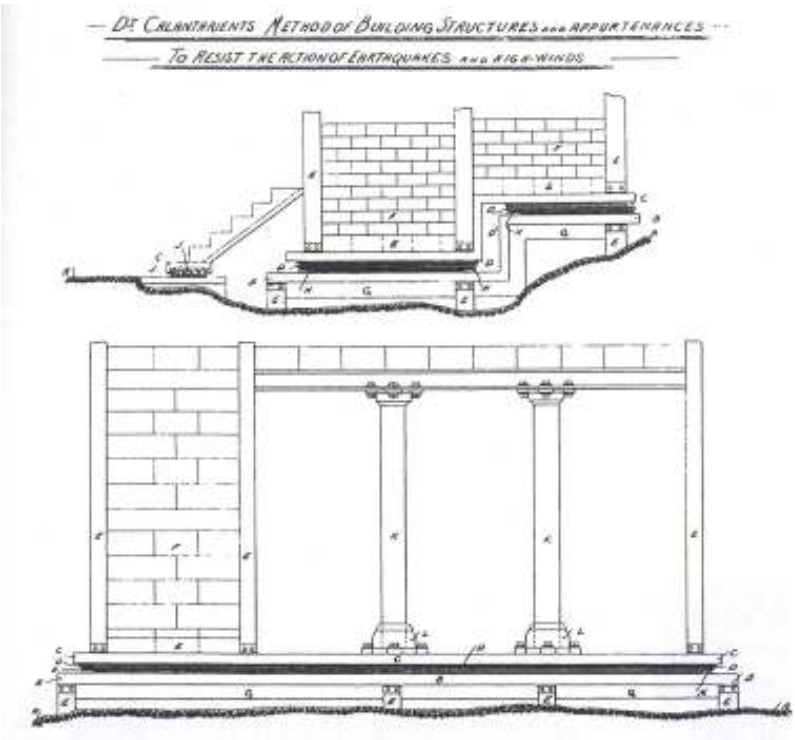

Figure 3.9 Clantarient`s base isolation system using a layer of talc as the isolating medium (Naeim and Kelly 1996).

3.4.1. The Eradiquake System (EDS)

The Eradiquake System (EDS) isolator is made up of essentially two components: (1) a sliding multirotational bearing assembly (2) a maintenance-free restoring device called the Mass Energy Regulator (MER) (Figure 3.10). The system restores through the MER and simultaneously dissipates energy via the steel and composite sliding bearing at the center. It is possible to design the bearing to have different energy dissipation and stiffness characteristics in the in-plane orthogonal directions. The value of Q_d is a function of the dynamic friction coefficient of the central sliding bearing. The value of K_d is governed by the properties of the MER (AASHTO 1999).

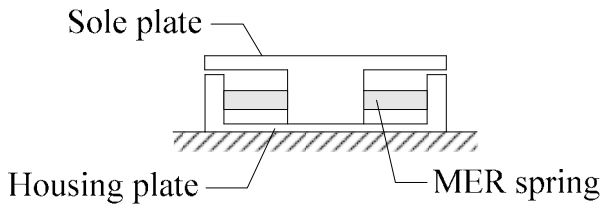

Figure 3.10 The Eradiquake seismic isolation bearing.

3.4.2. The High Damping Rubber System (HDRS)

The High Damping Rubber System (HDRS) is essentially the aforementioned elastomeric bearings with the only difference of having a modified rubber compound that acquires increased damping characteristics (Figure 3.11) (Naeim and Kelly 1996). High damping rubber layers deform under shear to reduce earthquake loads and dissipate energy (HITEC 1998). The isolator stiffens and acquires a higher level of energy dissipation at large deformations due to the strain crystallization process in the rubber (Naeim and Kelly 1996). The values of Q_d and K_d are a function of the additives to the rubber (AASHTO 1999).

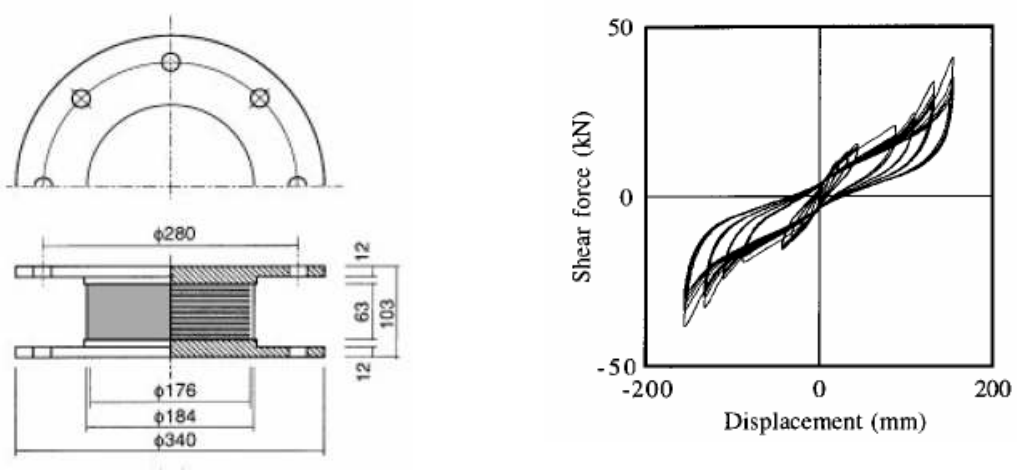

(a) (b)

Figure 3.11 (a) High damping rubber bearing used in the earthquake simulator tests with dimensions in mm (b) corresponding force-deformation hysteresis (Kikuchi and Aiken 1997).

3.4.3. The Lead Rubber Bearing (LRB)

The Lead Rubber Bearing (LRB) consists of steel plates, rubber and a lead core (Figure 3.12). A lead core is inserted down the center of the bearing for energy dissipation and stiffness (Priestley et al. 1996). Lead is a feasible option because it yields in shear at relatively low stresses, 10 MPa, and has good fatigue properties (Skinner et al. 1993). The steel layers placed between the rubber serves to limit the edge-bulging of the rubber (Tyler 1991). Additionally, the steel plates force the lead plug bearing to deform in shear (Naeim and Kelly 1996). As a multilayered elastomeric type bearing, the LRB is susceptible to a buckling type of instability. The force-deformation response is typically modeled as bilinear (Naeim and Kelly 1996). The value of Q_d is a function of the lead core and the value of K_d is a function of the rubber (AASHTO 1999). An important characteristic of the LRB is that the in cold temperatures, natural rubber causes a significant increase in the Q_d (AASHTO 1999).

The LRB is a type of isolator widely used in bridge applications (Buckle and Mayes 1990). It has been also reported based on information provided by the manufacturers that the cost, size and energy dissipation of the FPS and LRB may be comparable in bridge applications (Dicleli 2002). Consequently, the LRB is used in Chapter 6 to compare the applications of sliding versus elastomeric seismic isolation of bridges. The mechanical properties of the LRB is elaborated further in Chapter 6.

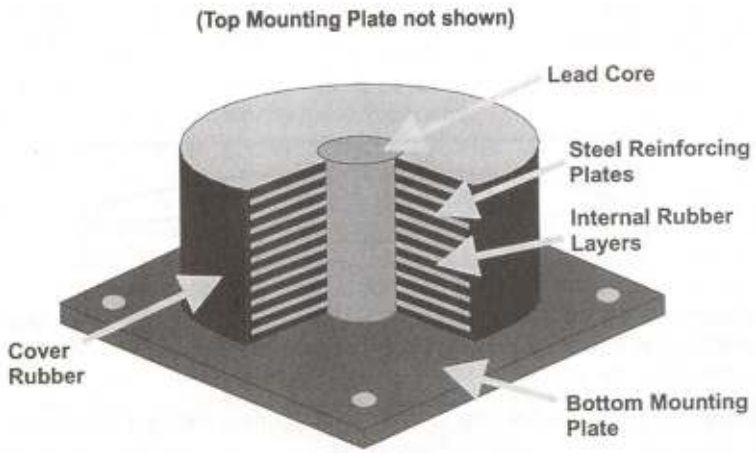

Figure 3.12 Typical lead rubber bearing (LRB) (Taylor and Igusa 2004).

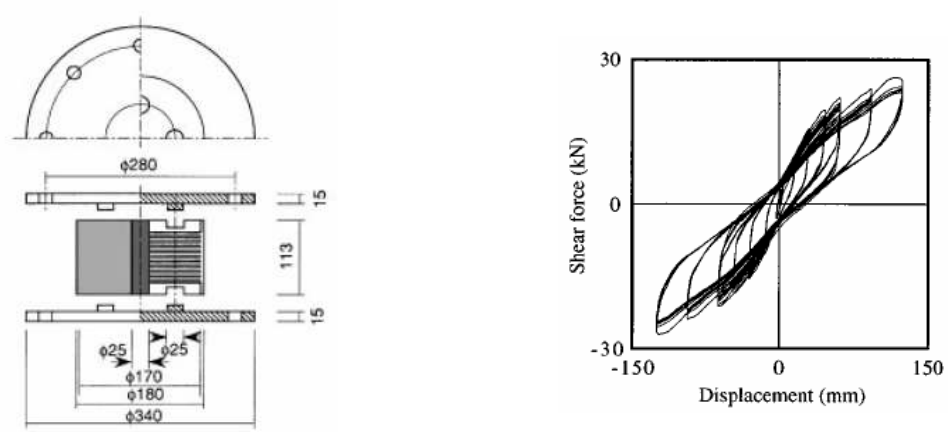

(a) (b)

Figure 3.13 (a) Lead rubber bearing (LRB) used in the earthquake simulator tests with dimensions in mm (b) corresponding force-deformation hysteresis (Kikuchi and Aiken 1997).

3.5 Conclusion

Seismic isolation of bridges is an effective approach for reducing the forces imparted by earthquakes. The favorable effects of seismic isolation is achieved essentially by decoupling the response of the structure from the ground motion and shifting the period for lower pseudo acceleration in the design spectrum. It is concluded from the modal analysis of a simplified bridge model that the stiffness characteristics of the isolators significantly control the dynamic response of the system. There are four analysis procedures available in the governing code of SIBs, the Guide Specifications. The most sophisticated one of these procedures, the time-history method, will be the basis of the analyses throughout this study. An overview of common isolators mentioned in the Guide Specifications has been presented.

CHAPTER 4

FRICTION PENDULUM SYSTEM (FPS) MODELING

4.1 Introduction

This chapter is devoted to the development of a new finite element (FE) model that can represent the inherent nonlinear and coupled response of the Friction Pendulum System (FPS). The general characteristics of the simplified bilinear model of the isolator are explained. The analogy between the simplified bilinear response of the FPS and the bilinear modeling presented in the AASHTO Guide Specifications (1999) is described. The equations and modeling techniques used to represent the nonlinear and coupled response of the isolator is reviewed, and the nonlinear kinematics of the isolator response is developed. The implementation of the response of the isolator into OpenSees via developing new C++ classes is explained. The FE model is verified with experimental data. Preliminary results on the influence of different modeling assumptions for the FPS are highlighted.

4.2 Simplified Isolator Response Modeling

The mobilized response of the FPS is representative of a mass sliding on a perfectly spherical surface with a coefficient of friction μ, and a radius of curvature R. The two components of the intrinsic forces of the FPS consists of the pendulum motion of the mass, f_R, and the friction between the mass and the sliding surface, f_μ. Assuming small deformations, the unidirectional force-deformation response of the FPS is (Zayas et al. 1987):

$$f = \overbrace{N\,\mu \mathrm{sgn}(\dot{\delta})}^{f_\mu} + \overbrace{\frac{N}{R}\delta}^{f_R} \tag{4.1}$$

where N is the normal force acting on the sliding surface, R is the radius of the concave surface, δ is the sliding deformation, $\dot{\delta}$ is the sliding velocity, and $\mathrm{sgn}(\dot{\delta})$ is the signum function. The signum function is equal to +1 or -1 depending on whether $\dot{\delta}$ is negative or positive, respectively (Figure 4.1). The friction response, f_μ, and the pendulum motion response, f_R, in Equation 4.1 are representative of plastic and elastic models, respectively, illustrated in Figure 4.2.

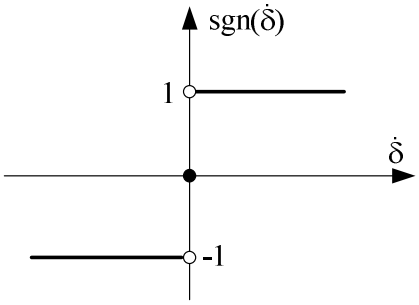

Figure 4.1 The signum function.

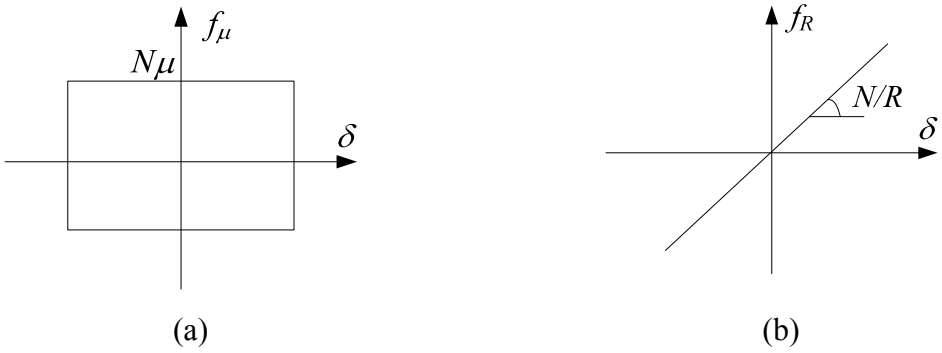

Figure 4.2 The intrinsic response components (a) friction, f_μ, and (b) pendulum, f_R.

The combination of f_R and f_μ corresponds to a unidirectional rigid-plastic hysteretic model given in Figure 4.3. The AASHTO Guide Specifications (1999) Section 7 on Analysis Procedures states that: *"To simplify the nonlinear behavior of the isolator unit, a bilinear simplification may be used"* (Figure 4.4). This bilinear hysteretic model is characterized by the elastic stiffness, K_u, post-elastic stiffness, K_d, characteristic strength, Q_d, yield force, F_y, and maximum isolator displacement, Δ_{max}. If the yield displacements of steel-Teflon sliding surfaces reported in the order of 0.05-0.02 cm by Constantinou et al. (1990) for conditions relevant to the FPS is considered, Figure 4.3 takes up the characteristics of the bilinear model in Figure 4.4. This bilinear model for the FPS given in Figure 4.3 is based on the assumptions that: (1) N is constant; (2) μ is constant; (3) the horizontal response is uncoupled in the orthogonal directions; and (4) isolator deformations are small and planar. The following sections elaborate on these aspects and how they may be incorporated into the response.

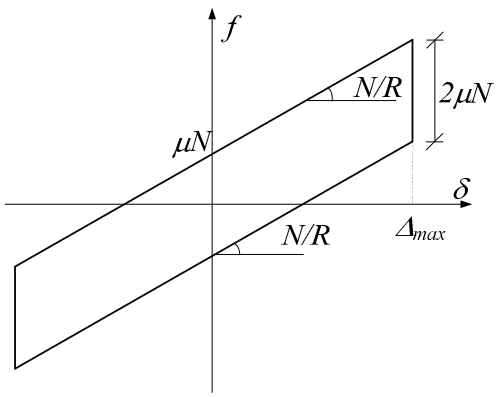

Figure 4.3 Force-deformation characteristics of the unidirectional rigid-plastic response of the FPS.

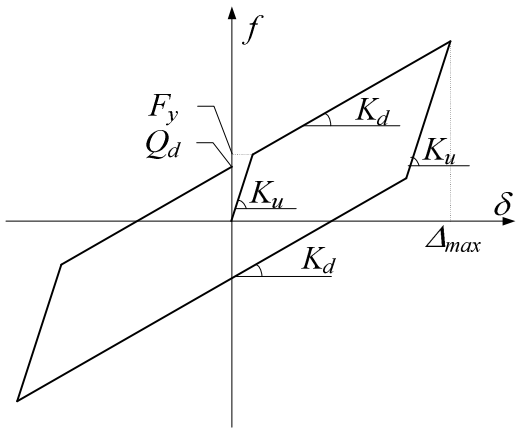

Figure 4.4 Force-deformation characteristics of bilinear isolators.

4.3 Normal Force

The normal force, *N*, acting on the FPS is inherent in both resisting force components, f_μ and f_R, of the response. An increase in the magnitude of *N* is indicative of a higher yield force which may delay the mobilization of the FPS under dynamic loads and a higher post-yield stiffness which may reduce the flexibility of the isolator. Additionally, *N* changes the magnitude of μ, however this relationship is discussed subsequently. The conventional FPS does not have resistance in tension and it is approximately rigid in compression (Zayas et al. 1987). This behavior closely matches the response of a zero-length gap element defined with a force:

$$f_g = \begin{cases} k_g \delta_g & \text{if} \quad \delta_g \le 0.0 \\ 0.0 & \text{if} \quad \delta_g > 0.0 \end{cases} \tag{4.2}$$

where k_g is a high compression stiffness and δ_g is the deformation (Figure 4.5). Modeling the vertical response of the FPS with a gap element allows simultaneously the monitoring of the variations in *N* and capturing the effects of uplift and impact in the FPS (Almazan and Llera 2003).

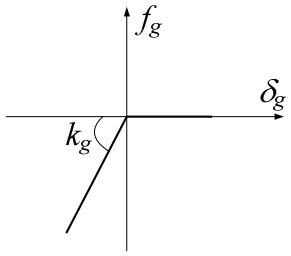

Figure 4.5 Gap element force-deformation model.

4.4 Coefficient of Friction

The coefficient of friction, μ, in addition to the material properties of the surface, was found to be primarily a function of $\dot{\delta}$ and N (Mokha et al. 1990). Accurate mathematical models have been developed by Constantinou et al. (1990) to capture the value of μ for a range of $\dot{\delta}$ and N that is of interest to the response of the FPS. The influence of $\dot{\delta}$ on the μ was approximated via the aid of experimental results as:

$$\mu = f_{max} - D_f e^{(-a|\dot{\delta}|)} \tag{4.3}$$

where, f_{max} and f_{min} are the values of coefficient of friction at large and small sliding velocities, respectively, D_f is the difference between f_{max} and f_{min}, and a is a constant, having units of time per unit length, that controls the variation of the coefficient of friction with velocity. Only the dependency of f_{max} to pressure, P, is considered in this study as the influence of pressure on f_{min} and a were shown to be negligible by Tsopelas et al.(1994). The term f_{max} as a function of P was given as:

$$f_{max} = f_{max,0} - D_{fmax} tanh(\varepsilon P) \tag{4.4}$$

where $f_{max,0}$ and $f_{max,p}$ are the values of f_{max} at very low and high pressures respectively, D_{fmax} is the difference between $f_{max,0}$ and $f_{max,p}$, and ε is a constant that controls the variation of f_{max} between very low and very high pressures (Figure 4.6). Equations 4.3

and 4.4 may be updated for the values of $\dot{\delta}$ and N in an iterative solution scheme to account for the changes in μ.

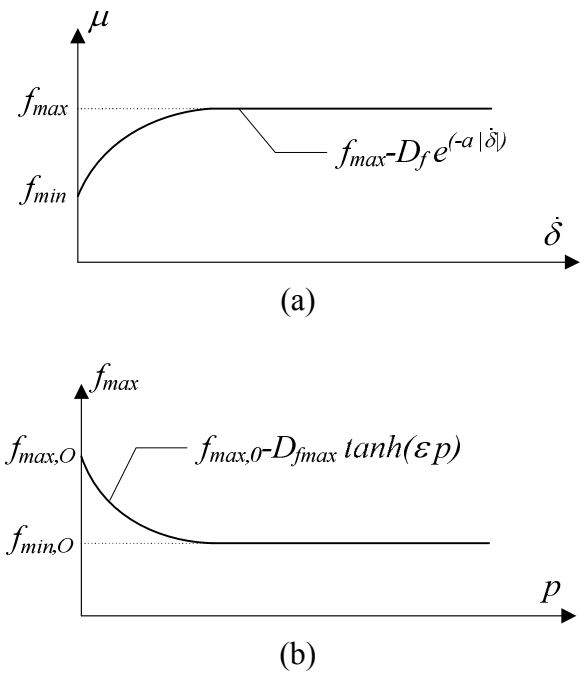

Figure 4.6 Variation of the coefficient of friction with (a) velocity of sliding; and (b) isolator contact pressure (Roussis and Constantinou 2006).

4.5 Bidirectional Coupling

Bidirectional motion may commence in the FPS isolator subject to multidirectional excitations. The two important characteristics of the bidirectional sliding motion are that: (1) the in-plane force-deformation response of the sliding is isotropic; and (2) the behavior shifts from stick and slip conditions (Constantinou et al. 1990). A simplified approach for modeling the planar frictional response is to consider two independent unidirectional elements according to the Coulomb's model in the orthogonal

x and y directions of the horizontal plane based on Equation 4.1. In this case the planar frictional force is:

$$\mathbf{f}_{\mu} = \begin{bmatrix} f_{\mu x} \\ f_{\mu y} \end{bmatrix} = N\mu \begin{bmatrix} \text{sgn}(\dot{\delta}_x) \\ \text{sgn}(\dot{\delta}_y) \end{bmatrix} \tag{4.5}$$

where, $f_{\mu x}$ and $f_{\mu x}$ are the components of the friction force, and $\dot{\delta}_x$ and $\dot{\delta}_y$, are the components of the velocity in the x and y directions, respectively. However, the calculation of $\mathbf{f}_{\mu}$ with two independent Coulomb's models for plane motion, overestimates the resistance, produces inaccuracies in capturing stick-slip conditions and raises complications in numerical computation (Constantinou et al. 1990).

The planar sliding force-deformation response of the FPS is isotropic. This implies that the interaction surface of $f_{\mu x}$ and $f_{\mu x}$ is circular and the resultant sliding friction force magnitude, $\|\mathbf{f}_{\mu}\| = \sqrt{f_{\mu x}{}^2 + f_{\mu y}}$, is equal to $N\mu$ regardless of the sliding direction. The planar frictional force that satisfies these conditions during sliding is:

$$\mathbf{f}_{\mu} = \begin{bmatrix} f_{\mu x} \\ f_{\mu y} \end{bmatrix} = N\mu \begin{bmatrix} \cos(\theta) \\ \sin(\theta) \end{bmatrix} \tag{4.6}$$

where, $\theta = \tan^{-1}(\dot{\delta}_y / \dot{\delta}_x)$ defines the direction of the sliding motion. Unlike the case presented by Equation 4.5, the components of $\mathbf{f}_{\mu}$ in Equation 4.6 are insensitive to the variations in the magnitudes of respective sliding velocities. Consequently, if the response of $\mathbf{f}_{\mu}$ is modeled by Equation 4.5, the magnitude of $\|\mathbf{f}_{\mu}\|$ during sliding ranges between $N\mu$, if sliding along the x or y axes, and $\sqrt{2}N\mu$, if sliding in a path along the 45 degree direction. The shape of the interaction surface between $f_{\mu x}$ and $f_{\mu x}$ is circular if Equation 4.5 is used and square if Equation 4.6 is used (Figure 4.7).

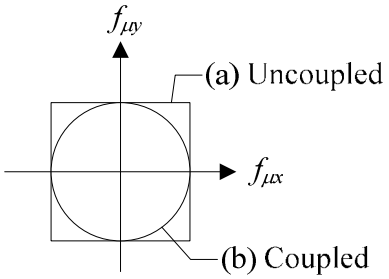

Figure 4.7 Frictional interaction surface (a) uncoupled (b) coupled response.

The response of the sliding system may shift between two phases: (1) the sliding phase, where motion commences in both directions; and (2) the sticking phase, where one or both of the components of the velocity are zero or very low (Constantinou et al. 1990). In the Coulomb's model, the transition between the two phases is independent from the magnitude of the sliding velocity and discontinuous (Figure 4.1). Constantinou et al. (1990) reported that the response of Teflon-steel sliding surfaces predicted via the Coulomb's model contained high-frequency components that did not prevail in the experiments. This was attributed to the significantly more sticking phases that developed in the Coulomb's model as a result of independence of resistance to the magnitude of the sliding velocity. There are complications in using Coulomb's model in numerical solutions because of the low rate of convergence caused by this discontinuity (Feldstein and Goodman 1973) and the difficulty of extending Equation 4.5 to plane motion (Younis et al. 1983).

Constantinou et al. (1990) extended the work of Park et al. (1986) and presented bi-dimensional hysteretic parameters, $\boldsymbol{\eta} = [\eta_x \quad \eta_y]^T$, to evaluate $\mathbf{f}_\mu$ in planar steel-Teflon sliding interfaces. The frictional force vector in this case is defined as:

$$\mathbf{f}_\mu = N\mu\boldsymbol{\eta} \tag{4.7}$$

where $\boldsymbol{\eta}$ is dimensionless hysteretic parameters that evolve according to the following coupled set of differential equations:

$$\boldsymbol{\eta} = \begin{bmatrix} \dot{\eta}_x \\ \dot{\eta}_y \end{bmatrix} = \frac{1}{\Delta s} \begin{bmatrix} A - a_x \eta_x^{\,2} & -a_y \eta_x \eta_y \\ -a_x \eta_x \eta_y & A - a_x \eta_x^{\,2} \end{bmatrix} \begin{bmatrix} \dot{\delta}_x \\ \dot{\delta}_y \end{bmatrix} \tag{4.8}$$

where $\dot{\delta}_x$ and $\dot{\delta}_y$, are the components of the sliding velocity in the x and y directions, respectively, $a_x = \beta + \gamma \operatorname{sgn}(\dot{\delta}_x \eta_x)$, $a_y = \beta + \gamma \operatorname{sgn}(\dot{\delta}_y \eta_y)$, Δ_Y is the yield displacements, A, β, γ are dimensionless constants that control the shape of the hysteretic loops. Constantinou et al. (1990) showed that for $A/(\beta + \gamma) = 1$, the solution of Equation 4.7: (1) describes a circular interaction curve; (2) for sliding conditions the hysteretic parameters are $\eta_x = \cos\theta$ and $\eta_y = \sin\theta$, where $\theta = \arctan(\dot{\delta}_y / \dot{\delta}_x)$; and (3) for sticking conditions $\|\boldsymbol{\eta}\| < 1.0$. The solution of the of the coupled differential Equation (4.8) can be solved via numerical algorithms presented for the common computer languages like C++ (Lee and Schiesser 2004; Press et al. 2003). Additionally, common numerical calculation software such as Mathcad (Pritchard 1998) and Matlab (Shampine et al. 2003) have a variety of built-in functions to solve coupled differential equation systems. In the model being developed for this study, the semi-implicit method presented by Rosenbrock (1963) have been utilized as the solution algorithm due to its: (1) relative simplicity; (2) ability to handle stiff problems; (3) common stability; and (4) acceptable accuracy ($<10^{-4} - 10^{-5}$) (Press et al. 2003).

4.6 Large Deformation Moments

In bridge applications, the FPS is installed above piers and abutments as either the concave dish facing up or down (EPS 2002). The orientation of the FPS controls whether the P-Δ moments occur at the structural members below or above the isolator (EPS

2002). This unique feature of the FPS does not have implications on the in-plane force-deformation response and allows for diverting P-Δ moments from weak elements of the structure (Almazan and Llera 2003). Figure 4.8 is a schematic of the displaced shape of an FPS between a simplified bridge superstructure and the column. The normal force, N, is transmitted through the slider to the concave dish. Assuming that the rotations at the superstructure and the top of the column are negligible, the displaced configuration of the FPS results in an internal moment $M=N\delta$. This internal moment, M, is balanced at the tip of the column if the concave dish is at the bottom and by the superstructure if the concave dish is at the top. Almazan and Llera (2003) presented a nonlinear transformation matrix for their FPS model to account for this aspect, which is elaborated in the subsequent section.

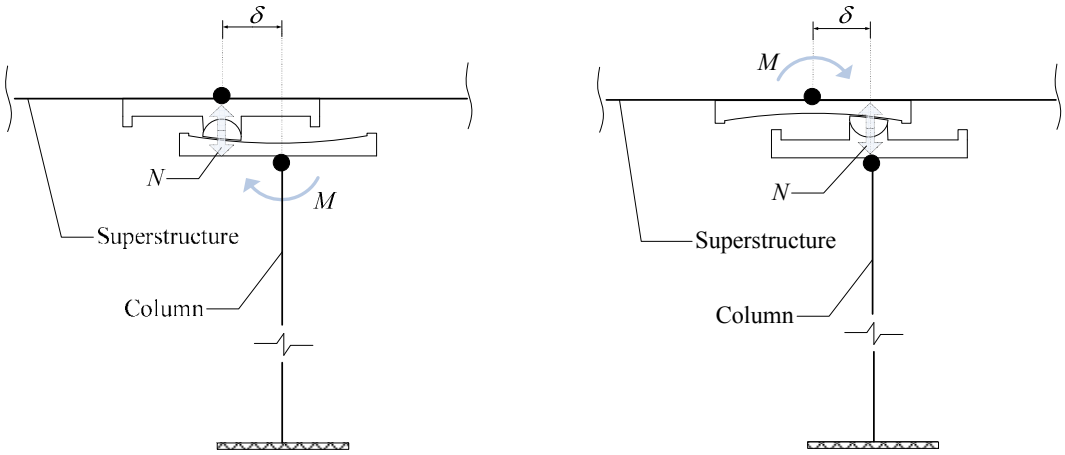

Figure 4.8 Deformed shape of the seismic isolator between the superstructure and the substructure with concave dish at the (a) bottom (b) top.

4.7 Mathematical Model

The exact three dimensional (3-D) kinematics equations considering large deformation effects of the FPS were developed by Almazan and Llera (2003). The zero-

length element developed in OpenSees to model the response of the FPS is constructed based on these principles by assuming no nodal rotations. The author does not claim any innovation for implementing this simplification and refer the reader to Almazan and Llera (2003) for a more detailed presentation of these principles. Here, only a brief summary of the mathematical formulation is presented with similar nomenclature as the original equations. The zero-length element is 3-D with 6 degrees of freedom (DOF) per node (Figure 4.9). This model accounts for the variations of the N via an inherent gap element described by Equation 4.2 and the variations of the μ via Equations 4.3 and 4.4 at each integration time step. The coupling of the sliding forces are included via the hysteretic parameters, $\boldsymbol{\eta} = [\,\eta_x \quad \eta_y\,]^{\mathrm{T}}$, as described in the previous sections. The P-Δ moments are transferred to the nodes of the model via a nonlinear transformation matrix.

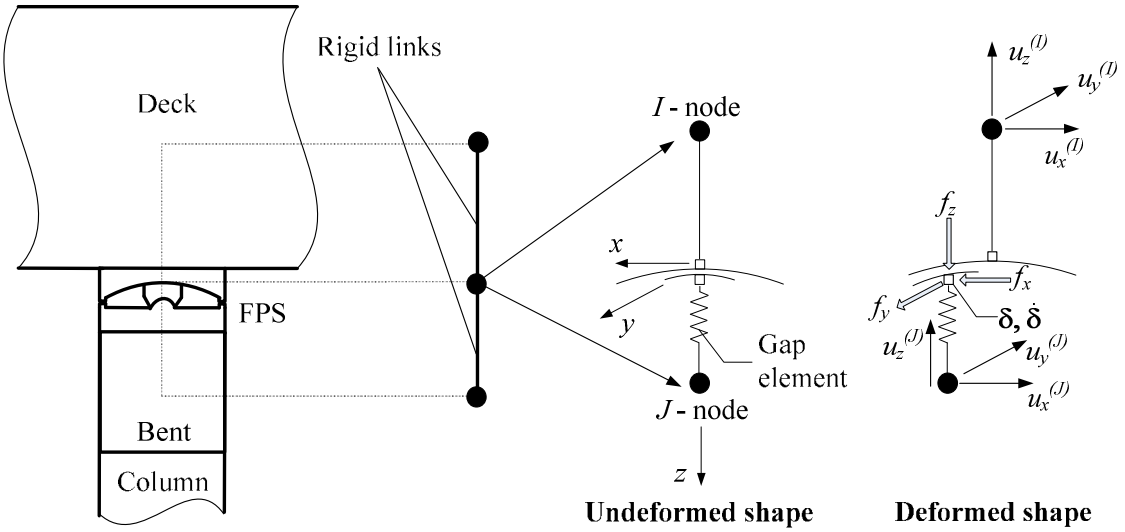

Figure 4.9 Schematic view of the model.

Assuming that the nodal rotations are negligible, the local slider and global coordinates coincide. The nodal deformations of the element are defined as $\mathbf{u}=[\mathbf{u}^{(J)}\ \mathbf{u}^{(I)}]^{\mathrm{T}}$, where $\mathbf{u}^{(J)}=[u_x^{(J)}\ u_y^{(J)}\ u_z^{(J)}\ r_x^{(J)}\ r_y^{(J)}\ r_z^{(J)}]^{\mathrm{T}}$ and $\mathbf{u}^{(I)}=[u_x^{(I)}\ u_y^{(I)}\ u_z^{(I)}\ r_x^{(I)}\ r_y^{(I)}\ r_z^{(I)}]^{\mathrm{T}}$ define the motions of nodes *J* and *I*, respectively. The instantaneous position and velocity of the slider is defined by the vectors $\boldsymbol{\delta}=[\,\delta_x\ \ \delta_y\ \ \delta_z\,]$ and $\dot{\boldsymbol{\delta}}=[\,\dot{\delta}_x\ \ \dot{\delta}_y\ \ \dot{\delta}_z\,]$, respectively (Figure 4.10). The slider's motion is bounded by the spherical surface of the concave dish defined as:

$$G=\delta_x{}^2+\delta_y{}^2+(\delta_z-R)^2=0 \tag{4.9}$$

The unitary vectors in the outward normal direction and the tangential to the trajectory of the slider are:

$$\mathbf{n}=\frac{\nabla G}{\|\nabla G\|}=\frac{1}{R}\left[\delta_x\ \ \delta_y\ \ (\delta_z-R)\right]^{\mathrm{T}} \tag{4.10}$$

and

$$\mathbf{s}=\frac{\dot{\boldsymbol{\delta}}}{\|\dot{\boldsymbol{\delta}}\|}=\left[\frac{\eta_x}{\|\boldsymbol{\eta}\|}\cos\alpha\ \ \ \frac{\eta_y}{\|\boldsymbol{\eta}\|}\cos\alpha\ \ \ sin\,\alpha\right]^{\mathrm{T}} \tag{4.11}$$

respectively (Figure 4.10), where,

$$\alpha=\arctan\left(\frac{\delta_x\dfrac{\eta_x}{\|\boldsymbol{\eta}\|}+\delta_y\dfrac{\eta_y}{\|\boldsymbol{\eta}\|}}{R-\delta_z}\right) \tag{4.12}$$

denotes the angle between the frictional force component and the *x*-*y* plane. The local slider restoring forces for all phases is:

$$\mathbf{f}=\left[f_x\ \ f_y\ \ f_z\right]^{\mathrm{T}}=N\mathbf{r} \tag{4.13}$$

where, **r**, is the restoring force orientation vector that is constituted from the normal and tangential components of the slider as:

$$\mathbf{r} = \overbrace{\mathbf{n}}^{\text{normal component}} + \overbrace{\mu\|\boldsymbol{\eta}\|\mathbf{s}}^{\text{tangential component}} \tag{4.14}$$

The concavity and friction-based components of the isolator are $\mathbf{f_R} = \mathbf{n}N$ and $\mathbf{f_\mu} = N\mu\|\boldsymbol{\eta}\|\mathbf{s}$, respectively. The normal force in the isolator is:

$$N = \frac{f_g}{r_z} \tag{4.15}$$

where r_z is the axial component of the vector **r**.

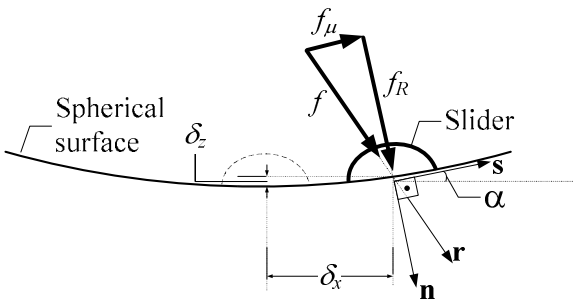

Figure 4.10 Deflections and forces acting on the slider.

The nodal force vector $\mathbf{F}=[\mathbf{F}^{(J)}\ \mathbf{F}^{(I)}]^{\mathrm{T}}$, where $\mathbf{F}^{(J)}=[F_x^{(J)}\ F_y^{(J)}\ F_z^{(J)}\ M_x^{(J)}\ M_y^{(J)}\ M_z^{(J)}]^{\mathrm{T}}$ and $\mathbf{F}^{(I)}=[F_x^{(I)}\ F_y^{(I)}\ F_z^{(I)}\ M_x^{(I)}\ M_y^{(I)}\ M_z^{(I)}]^{\mathrm{T}}$ define the forces at nodes *J* and *I*, respectively, is:

$$\mathbf{F} = \hat{L}^{\mathrm{T}}\mathbf{f} \tag{4.16}$$

where $\hat{L}^{\mathrm{T}}$ is the transform of the nonlinear transformation matrix defined as:

$$\hat{L} = \begin{bmatrix} \pm 1 & 0 & 0 & 0 & 0 & 0 & \pm 1 & 0 & 0 & 0 & \mp\delta_z & \pm\delta_y \\ 0 & 1 & 0 & 0 & 0 & 0 & 0 & -1 & 0 & \delta_z & 0 & -\delta_x \\ 0 & 0 & \pm 1 & 0 & 0 & 0 & 0 & 0 & -1 & \mp\delta_y & \pm\delta_x & 0 \end{bmatrix} \tag{4.17}$$

The top and bottom signs in Equation 4.17 are used to differentiate between the downward and upward positions of the FPS, respectively. The transformation matrix, $\hat{L}$,

depends exclusively on geometry and is nonlinear to account for the variation of the *P-Δ* moments. The exclusion of the vertical rise in the concave dish corresponds to $\delta_z = 0$, $\alpha = 0$, and $N = f_g$. In this case Equation 4.13 becomes:

$$\mathbf{f} = \begin{bmatrix} f_x & f_y & f_z \end{bmatrix}^{\mathrm{T}} = N \begin{bmatrix} \frac{\delta_x}{R} + \eta_x \mu & \frac{\delta_y}{R} + \eta_y \mu & -1 \end{bmatrix}^{\mathrm{T}} \tag{4.18}$$

4.8 Evaluation Platform

The Open System for Earthquake Engineering Simulation (OpenSees) is an open source software framework for simulating the earthquake response of structural and geotechnical systems (Mazzoni et al. 2006). OpenSees has an open source object-oriented architecture in the C++ programming language that maximizes its modularity, thus making it a viable choice for research purposes. OpenSees is chosen as the simulation platform for this study mainly because of its ability to access its source code to incorporate new material and element models without the need to perform changes in the existing solution algorithms. Material and element models describing the hysteretic response of new structural members can be developed as C++ classes and inserted into the existing library of OpenSees for analyses. This powerful attribute of OpenSees allows researchers to analyze a wide range of aspects of innovative materials and elements in larger models. Although OpenSees provides a variety of hysteretic uniaxial force-deformation response models, none of them was found to be capable of adequately representing the mathematical model described previously. Consequently, a 3-D zero-length *element*[1] class and a complimentary *material* class that can optionally include/exclude the modeling aspects of the FPS is implemented into OpenSees. The implementation of this procedure requires a combined knowledge of C++ programming,

[1] Italicized word is used for C++ class

object-oriented-design and the definitions and architecture of OpenSees framework. There is no source, to the author's knowledge, that provides a step-by-step explanation of adding new *elements* or *materials* into the existing library of OpenSees. The annually held OpenSees Developer Workshop at Berkeley, California gives limited yet valuable insight about these procedures (McKenna 2005a; McKenna 2005b).

A typical structural member in OpenSees is constructed via the *material* and *element* classes. The *material* class receives nodal displacements and velocities as input from the element class and returns trial force and tangent stiffness values according to a predefined force-deformation law. The *element* class is responsible for the generation of time dependent stiffness and transformation matrices and equilibrium iterations. The *element* class has access to all the forces from the materials in different directions. The new *material* class developed for the FPS model, *FPSmaterial*, is responsible for evaluating the corresponding components of $\mathbf{f}$ via Equation 4.13. In addition to the strain and velocity, Equation 4.13 requires that, N, the corresponding component of $\boldsymbol{\eta}$, and μ, at each integration time step be delivered from the *element* class. This is accomplished by adding these parameters to the corresponding abstract method via overriding (see Appendix A). The new *element* class developed for the FPS model, *FPSelement*, is designed to interact with *FPSmaterial*. In addition to the typical parent *element* class in OpenSees, the *FPSelement* is designed to evaluate large deformation effects in N via Equation 4.2, solve the parameters of $\boldsymbol{\eta}$ via the semi-implicit Rosenbrock (1963) method in Equation 4.8, update the values of μ via Equations 4.3 and 4.4 and α via Equation 4.12, and to construct the $\hat{L}$ via Equation 4.17 at each time integration step (Figure 4.11). The C++ script for differential equation solution with the Rosenbrock Methods presented by Press et al. (2003) has been incorporated into the *FPSelement* class to solve the parameters of $\boldsymbol{\eta}$.

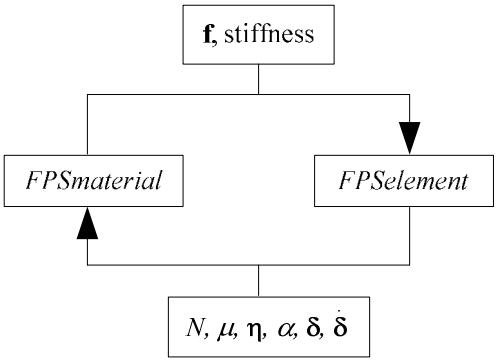

Figure 4.11 *FPSelement* and *FPSmaterial* interaction.

4.9 Verification

The FE model developed for the FPS in OpenSees is verified with respect to data obtained from experimental studies performed on a rigid isolated frame by Mosqueda et al. (2004) and the influence of modeling assumptions are monitored. A 3-D model of the experimental setup is developed in OpenSees. Two loading schemes comprised of unidirectional and bidirectional paths are applied to the model to illustrate the characteristics of the FPS force-deformation response.

4.9.1. Structural Properties and Loads

The structural model considered herein is the test setup studied at the Earthquake Engineering Research Center (EERC) headquartered at the University of California, Berkeley by Mosqueda et al. (2004). The test setup consisted of four FPS isolators installed under a rigid concrete block (Figure 4.12). The objective of the test was to examine the bi-directional response of the FPS isolators. The frame was loaded with a 1.78 m (*x* direction) by 2.85 m (*y* direction) rectangular rigid mass totaling approximately 290 kN, to produce a target vertical load on each isolator of 72.5 kN. The isolators had a concave surface with a 76.2 cm radius and the μ at low and high velocities, f_{min} and f_{max},

were given as 0.05 and 0.11, respectively. The maximum displacement capacity of the isolators was $\pm$ 17.8 cm. However, the maximum displacement capacity of the simulator was $\pm$ 12.7 cm. The yield displacement of the isolators, Δ_y, was approximately 0.025 cm. The constant describing the rate of transition from low to high velocities, *a*, was found to be 1.5 by Mosqueda et al. (2004). However, the constant, ε, that controls the variation of f_{max} between very low and very high pressures is not provided. Constantinuo et al. (1993) gave this relationship as $f_{max} = 0.12 - 0.07\tanh(\varepsilon p)$. This relationship is scaled by 1.2 to match the value of f_{max}=0.11 in the Mosqueda et al.(2004) study at a normal load level of 72.5 kN (Figure 4.13).

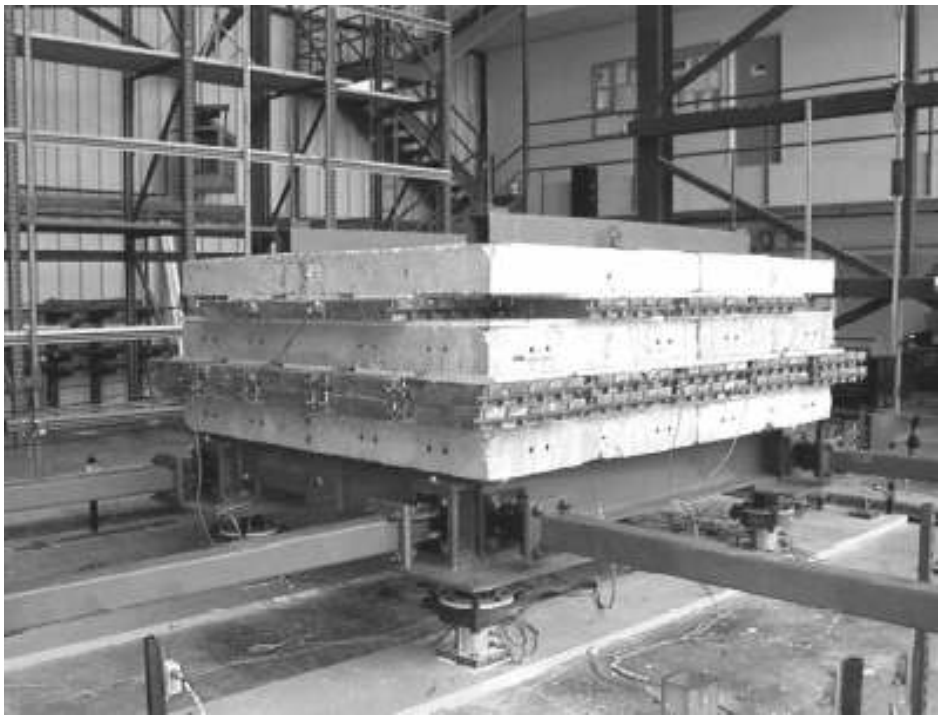

Figure 4.12 Test setup studied by Mosqueda et al. (2004).

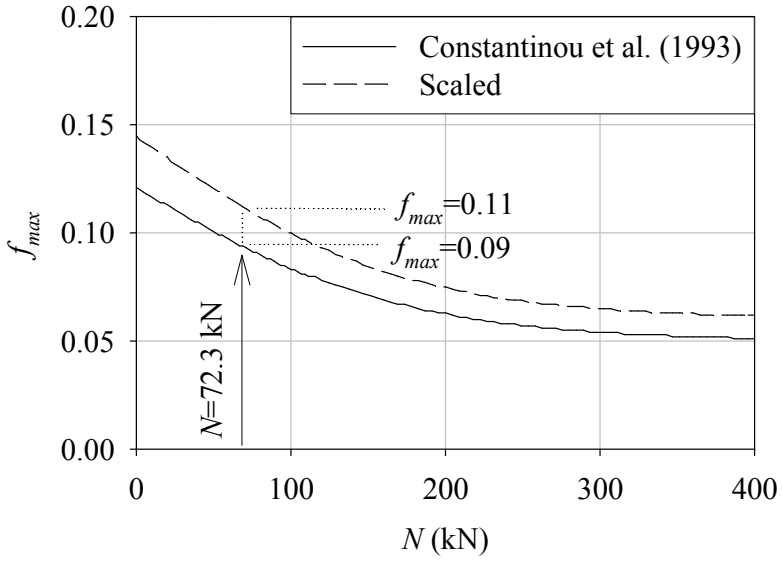

Figure 4.13 Scaling of f_{max} with respect to the relationship presented in Constantinou et al. (1993).

The frame is analyzed under displacement controlled unidirectional (L1) and bidirectional (L2) loadings. The unidirectional loading (L1) is categorized as L1a, L1b and L1c sinusoidal motions with peak displacement values of 12.7, 17.8 and 45.0 cm, respectively (Figure 4.14). The loading L1a has a maximum displacement that is limited by the simulator capacity of the test setup and is used to verify only force-deformation response per tests data. The second loading, L1b, has the maximum displacement capacity of the isolators and it is used to observe bounds of the μ on the force deformation response. The third load path, L1c, exceeds the maximum capacity of the isolators and it is purely theoretical. This path is used to monitor the range which large deformation effects become significant in the response of the isolators.

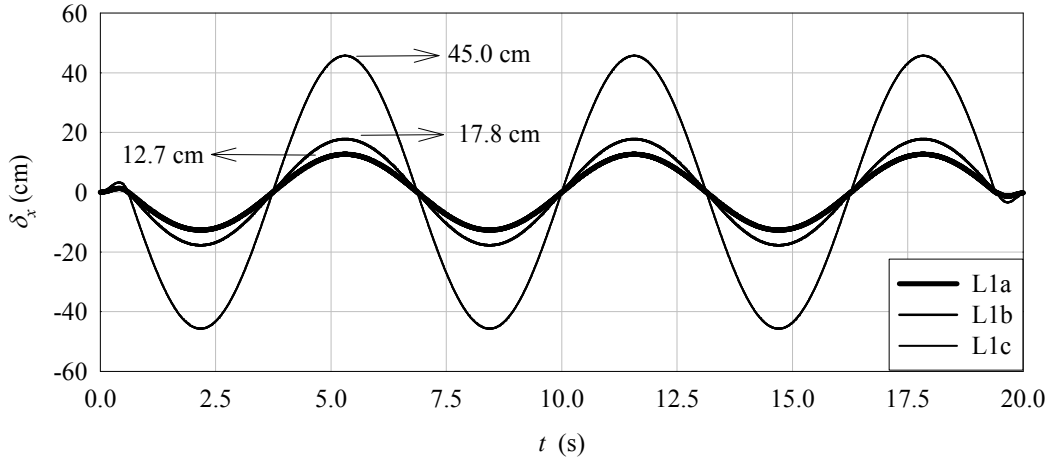

Figure 4.14 Unidirectional load histories with amplitude, ± 12.7 cm (L1a), ± 17.8 cm (L1b), and ± 45.0 cm (L1c).

The bidirectional loading, L2, is used to verify the planar response of the isolators and monitor the influence of the effects of bidirectional sliding interaction in the response. The history of the displacements in each orthogonal direction is defined by $B\sin(wt)$, where $B=5$ is the amplitude of the motion, t is the time, and w is the frequency equal to 1 in the x direction and 2 in the y direction (Figure 4.15).

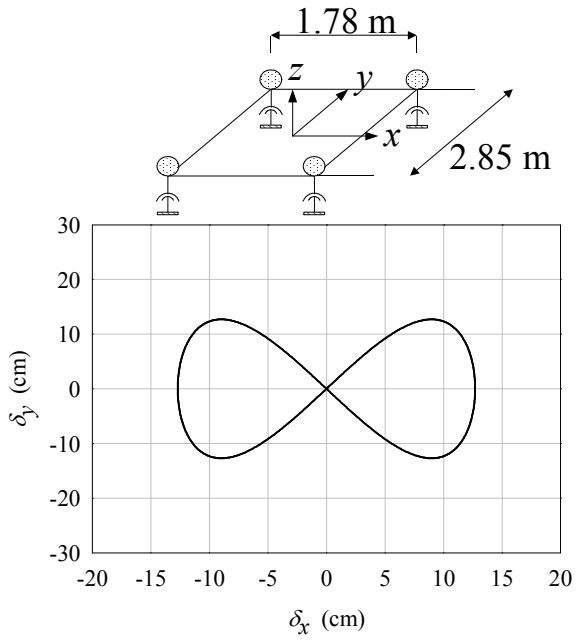

Figure 4.15 Combined bidirectional loading path for L2.

4.9.2 Modeling and Analysis

A three dimensional (3-D) model of the setup is developed in OpenSees via rigid beam elements and the zero-length element developed for the FPS (Figure 4.16). The base of the model is fixed at the four corners in all directions. The mass of the rigid block is lumped at the four corners and these corners are connected via rigid beam elements. After applying only the gravity portion of the corresponding load case, the gravity loads are held constant and the lateral load is applied to the model. This allows for the development of the frictional forces in zero-length elements. All analyses are geometrically nonlinear and a Newton-Raphson solution algorithm is used for the solutions.

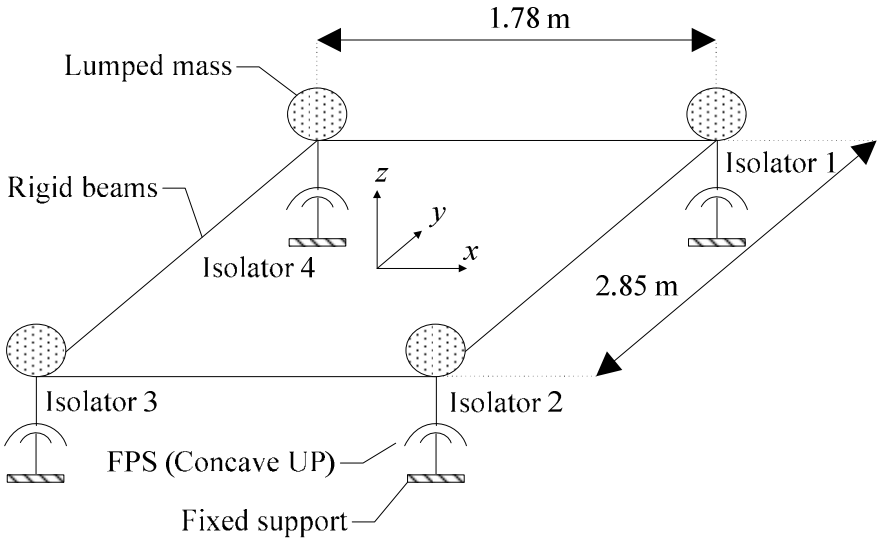

Figure 4.16 Finite element model of the test setup studied by Mosqueda et al. (2004).

4.9.3 Results

Mosqueda et al. (2004) reported that as a result of the rigidity of the supported block, minor changes in the vertical alignment of the setup caused significant redistribution of the normal forces acting on the isolators, and in some cases complete unloading. The authors have also underlined the difficulty of adequately modeling the friction response of the FPS. The normalized force-deformation history of Isolator 3 and the overall superstructure computed from the model and the experimental results for L1 is given in Figure 4.17. Given the complexity of the response, results predicted by the model are in agreement with that reported from the experiment.

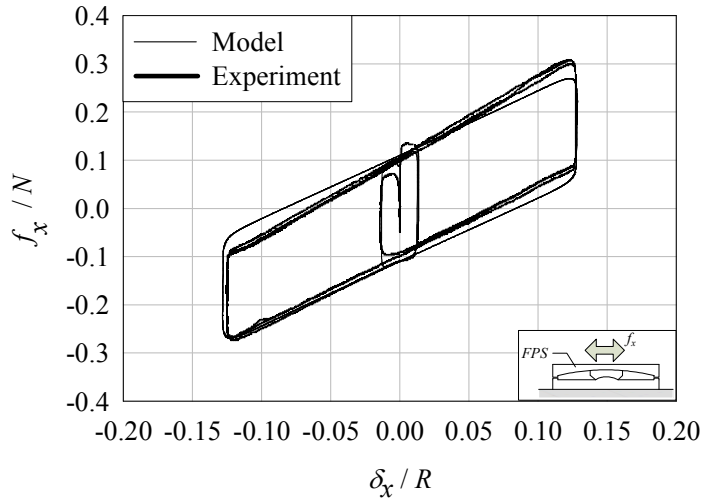

(a)

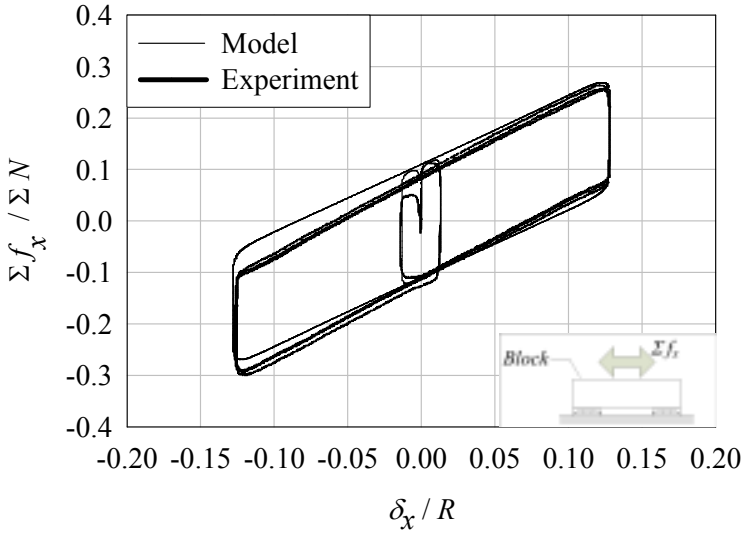

(b)

Figure 4.17 Comparison of the normalized force-deformation histories between the model and the experimental results for (a) individual Isolator 3, and (b) total isolator forces.

Figure 4.18 shows the variation of μ for loading path L1b. Despite the assumption of constant N on the FPS, the value μ ranged between 0.05 to 0.11 due to

changes in the sliding velocity. This is equivalent to a 110% variation in the frictional force component, f_μ, of the FPS during response. The upper and lower bounds of the isolator response as a function of f_{min}=0.05 and f_{max}=0.11 is given in Figure 4.19. The maximum isolator force (MIF) calculated by the model by accounting for velocity and pressure effects in the friction coefficient was 24.02 kN. This value was overestimated by 9.6% and underestimated by 10.5% when the μ was assumed to be f_{min} *and* f_{max}, respectively. The shape of the force-deformation histories given in Figure 4.19 also reveal that the energy dissipated per cycle under different assumptions for the value of the μ is proportionally variant as in the case of MIF.

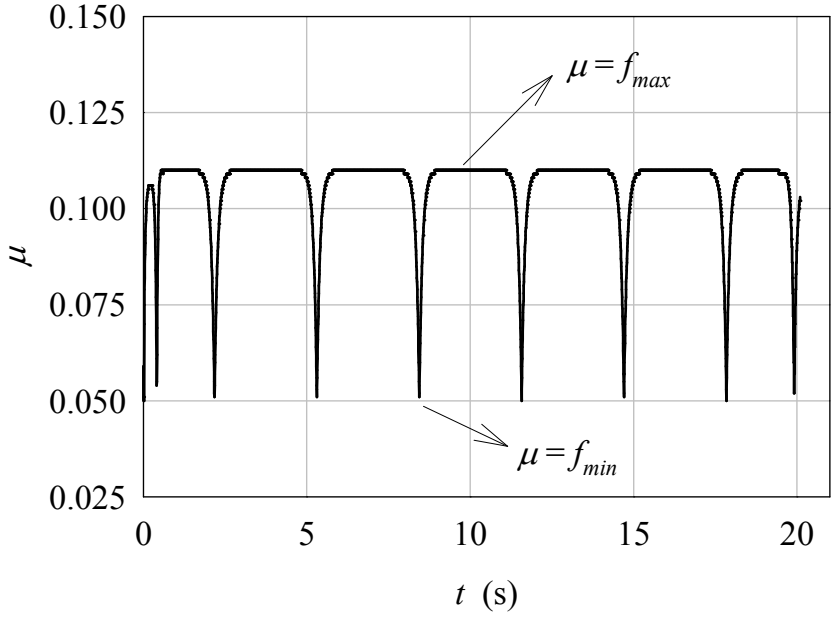

Figure 4.18 Friction coefficient, μ, time history under loading L1b.

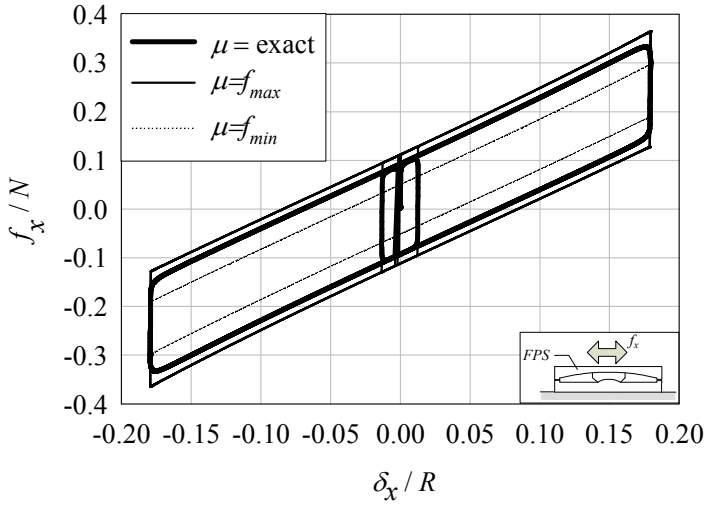

Figure 4.19 Comparison of the force-deformation histories of the FPS with theoretically exact value of the friction coefficient, μ, $\mu = f_{max}$, and $\mu = f_{min}$ for loading L1b.

Isolator response under L1c with the small deformations model (SDM) and the large deformations model (LDM) are given in Figure 4.20. It is observed that the difference between the SDM and the LDM is negligible under even the maximum isolator displacement capacities which correspond to δ_x/R=0.18. Inclusion of the large deformation effect reduced the MIF at theoretical displacements that exceed the isolator deformation capacity. This softening is attributed mainly to the inclusion of the geometric angle α in the calculation of the *N at* large displacements. The difference in the MIF between the LDM and the SDM for this particular case was less than 4% at the maximum displacements of L1c loading.

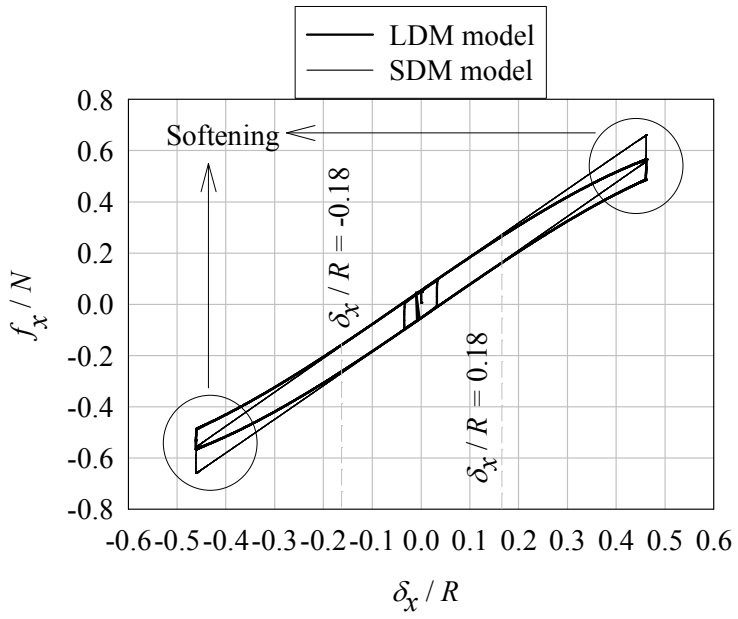

Figure 4.20 Comparison of the response of the small deformations model (SDM) and the large deformations model (LDM).

The force-deformation histories and the combined resisting force paths in the two orthogonal directions of the combined isolators under L2 are given in Figures 4.21. This figure shows that the force paths in the orthogonal directions predicted by the coupled model are in agreement with test results. A comparison of this response with an uncoupled model is presented in Figure 4.22. It is observed that, the uncoupled model deviates significantly from the path of the coupled model as the resisting forces change directions. The variation of the components of the instantaneous velocity in the orthogonal directions had significant influence on the force history in the *x*- direction. This is attributed mainly to the variation of the coupled parameters of the $\boldsymbol{\eta}$ varying continuously as a function of time. The MIF of 24.5 kN with the coupled modeled was overestimated as 29.4 kN (20% difference) with the uncoupled model.

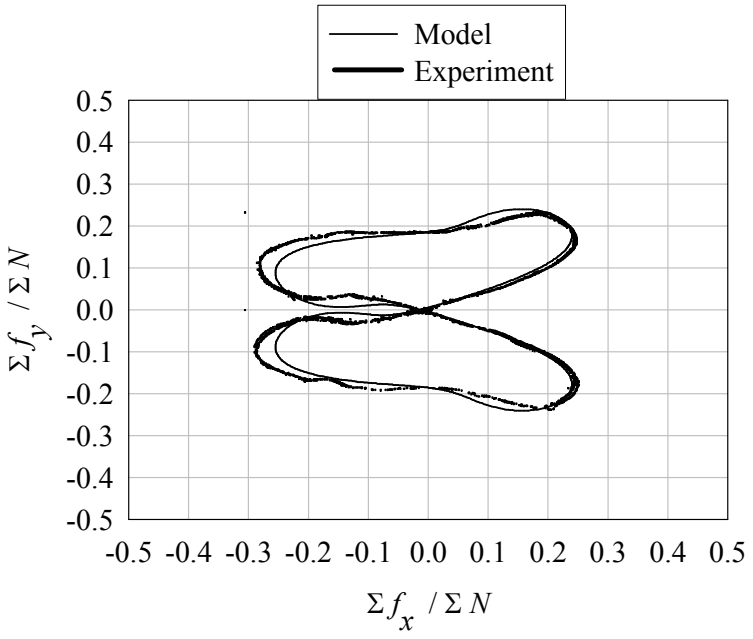

Figure 4.21 Comparison of the bidirectional resisting forces for the experimental data, and coupled model.

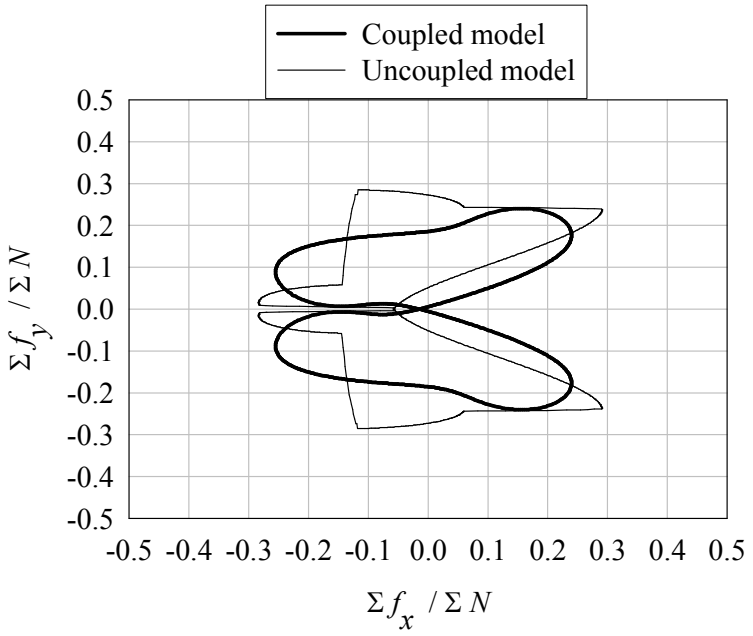

Figure 4.22 Comparison of the bidirectional resisting forces for the coupled model and the uncoupled models.

4.10 Conclusion

In this chapter, the simplified bilinear modeling of the Friction Pendulum System (FPS) has been explained. The simplifying assumptions in this approach and how aspects pertaining to these simplifications can be represented in the finite element (FE) model of the FPS has been highlighted. A new 3D zero-length FE of the FPS has been developed in OpenSees and verified using experimental data. The influence of neglecting certain modeling aspects of the FPS response has been presented. The following conclusions can be drawn from this chapter:

(1) There exists sufficient theoretical and experimental findings on different modeling aspects of the FPS; however a comprehensive FE model that combines these effects is absent. An FE model to fill this gap has been developed and compiled from existing research and implemented as a new element into OpenSees.

(2) The FE model developed in OpenSees for the response of the FPS provides good agreement with experimental findings of Mosqueda et al. (2004) under both unidirectional and bidirectional loadings.

(3) It was observed that the different assumptions in modeling the FPS caused significant variations in the paths of the force-deformation histories of the isolators. These affects need to be quantified for bridge applications. Different assumptions pertaining to the modeling of structures seismically isolated with the FPS may lead to over or under design of isolators.

CHAPTER 5
BRIDGE RESPONSE AS A FUNCTION OF ISOLATOR MODELING ASSUMPTIONS

5.1 Introduction

This chapter investigates the response of typical highway bridges isolated with the Friction Pendulum System (FPS) as a function of isolator modeling assumptions. The selection and detailed modeling of the bridges considered for seismic isolation with the FPS are presented. Seven models of a three-dimensional (3-D) Multi-Span Continuous (MSC) Steel Girder bridge with different assumptions of the FPS are generated. Nonlinear time history analyses (NLTH) are performed for the bridge to examine the effect of modeling parameters of the FPS on the response. The influence of the variations in isolator normal force, N, and coefficient of friction, μ, in-plane bidirectional sliding interaction, large deformation, P-Δ effects, and the orientation of the FPS isolators are highlighted. Maximum normalized force (MNF) and deformation (MND) of the isolators and column drifts are used as the parameters to characterize the response of the models.

5.2 Selection of the Class of Highway Bridges for Seismic Isolation and Analyses

A detailed survey of 163,433 bridges in the Central and Southeastern US (CSUS) was performed by Nielson (2005). The results of this study showed that Multi-Span Continuous (MSC) Steel Girder and Multi-Span Simply Supported (MSSS) Steel Girder bridges and MSC and MSSS Concrete Girder bridges are among the most common classes of bridges found in the CSUS inventory (Figure 5.1). Nielson (2005) further performed the fragility assessment of the classes of bridges and concluded that the MSC and MSSS Steel Girder bridges were among the most vulnerable to damage, followed by

the MSC and MSSS Concrete Girder bridges. Previous research identified significant vulnerabilities of the steel fixed and rocker bearings employed in these bridges to seismic loads (Mander et al. 1996). Seismic isolation of these bridges via replacing the existing steel bearings with the Friction Pendulum System (FPS) may be an effective tool for improving the earthquake performance. Assuming that the superstructure of SIBs remains within the elastic range, the modeling of the steel and concrete bridges are similar. Particular emphasis is given to these highway bridges in subsequent sections of this dissertation.

Figure 5.1 Picture of example MSC Steel Girder Highway Bridge (Nielson 2005).

5.3 Seismically Isolated Bridge (SIB) Modeling

The bridge type selected for the NLTH analysis in this chapter is an MSC Steel Girder Bridge seismically isolated with FPS isolators (Nielson 2005). The 3-D SIB model was developed in OpenSees. This model includes material and geometric nonlinearities. The geometry and modeling approach for the bridge is illustrated in Figures 5.2 and 5.3. The bridge has three spans and a continuous slab-on-girder deck with a total of eight steel girders. The seismic isolation of the bridge is achieved via placing FPS isolators under each of the eight girders above the piers and abutments. The

width of the expansion joints at the abutments is 7.7 cm. The FPS isolators are selected to achieve approximately a 2.0-2.5 second fundamental period which corresponds to R = 99 cm with an in-plane displacement capacity of 23 cm. The isolators are assumed to be positioned as the concave dish at the top. The slider diameter has 7.7 cm to ensure pressures below 275 MPa under gravity and earthquake loads in accordance with the recommendations of the manufacturer. The characteristic properties of the μ are selected as: a = 59.1 s/m, Δ_s = 0.025 cm, ε = 0.012 MPa^{-1}, f_{max} = 0.12 and f_{min} = 0.05 (Mosqueda et al. 2004; Constantinou et al. 1993).

The superstructure is expected to remain within the linear elastic range, thus, the deck elements are modeled using elastic beam column elements, using the composite section properties. The section properties for the columns and the bent beams are created using fiber elements with appropriate constitutive models for both the concrete and the steel reinforcement. The reinforcing steel is modeled as a bilinear material with a yield strength, f_{ys} = 414 MPa, and an elastic modulus, E_s = 200 GPa. A strain hardening ratio of 0.018 is used for this material (Figure 5.4). The unconfined and confined concrete behavior is modeled via the Kent-Scott-Park model which utilizes a degraded linear uploading/reloading stiffness and a residual stress. The concrete compressive strength, f_c, and associated strain, ε_c, are 27.6 MPa and 2.10^{-3} for the unconfined case and 28.5 MPa and (2.062)10^{-3} for the confined case, respectively (Figure 5.4). The bridge has footings which are 2.44 m square and use eight piles. The horizontal, k_t, and rotational, k_r, stiffnesses of the foundation are 130.5 kN/mm and (6.06)10^5 kNm/rad, respectively. Structural damping is assumed to be 5%.

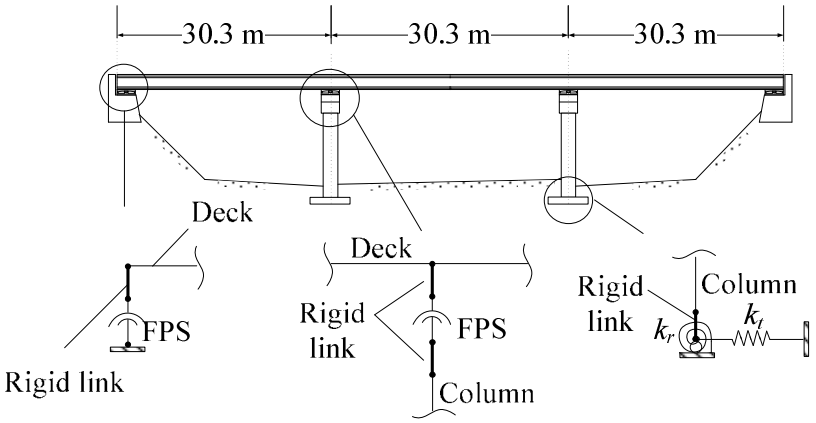

Figure 5.2 Multi-span continuous (MSC) steel girder bridge general elevation and modeling details.

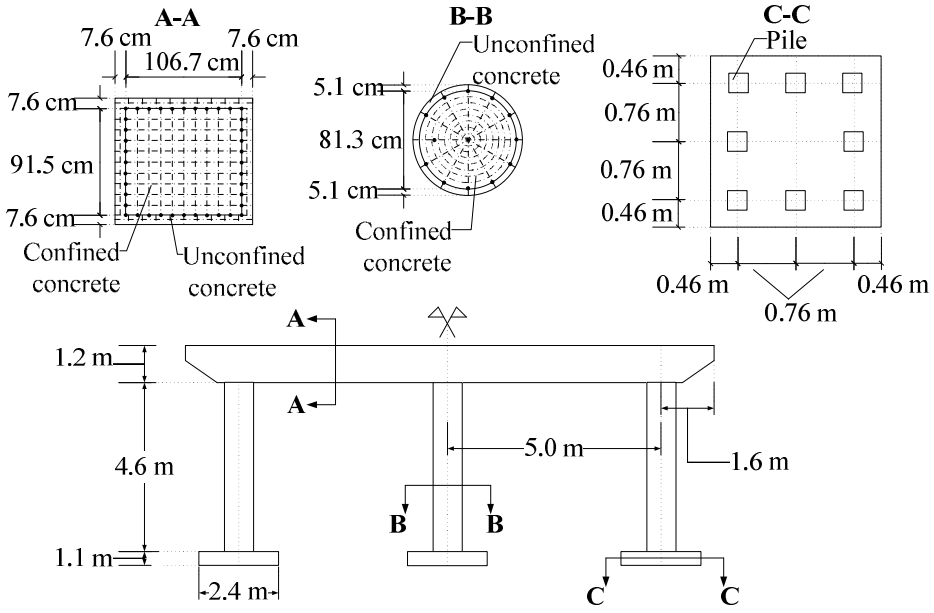

Figure 5.3 Pier configuration and bent and column discretization.

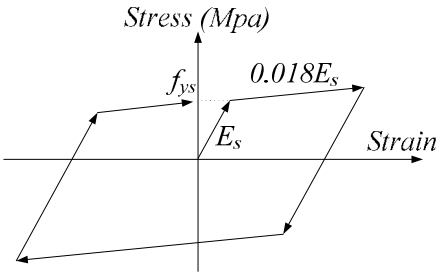

(a)

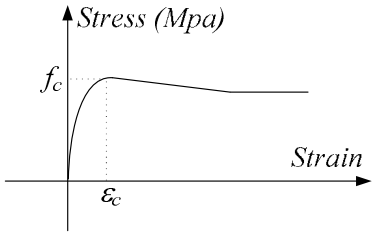

(b)

Figure 5.4 Constitutive relationships for the modeling of (a) steel material; and (b) concrete material.

5.4 FPS Models

Seven SIB models are generated with the above properties where the only difference is in the FPS modeling assumptions. The first model is theoretically exact, i.e., accounts for the variations of the N and μ, has bi-directional coupling of the sliding forces and incorporates P-Δ effects. The second model is a simplified bilinear model that is insensitive to the variations in N and μ, with uncoupled bi-directional sliding forces and small deformation assumptions. In Model 2, the constant value of N is taken as the corresponding value after gravity load analysis and μ as 0.07. The third model is developed to monitor the influence of not accounting for the variations of N on the response of the FPS. It is the same model as Model 1 with the only difference of assuming a constant N of the corresponding value after gravity load analysis. The fourth model is developed to identify the influence of the bidirectional coupling in estimating

the response of the FPS. It is the same model as Model 1 with the only difference of assuming the orthogonal sliding forces of the FPS isolators to be uncoupled. This is achieved by assuming $\boldsymbol{\eta} = [\,\mathrm{sgn}(\dot{\delta}_x) \quad \mathrm{sgn}(\dot{\delta}_y)\,]^{\mathrm{T}}$. The fifth model is developed to monitor the influence of not accounting for the inclination due to the concavity in the FPS. This is achieved by computing **f** with Equation 4.18 . The sixth model is generated to identify the influence of the FPS orientation. Model 6 is same as Model 1 with the only difference being that the FPS isolators are positioned with the concave dish at the bottom which is accommodated as the corresponding sign shift in the $\hat{L}$ in Equation 4.17. The seventh model, is developed to monitor the influence of the assumptions on the value of μ. Model 7 is established with the same principles as Model 1 with the only difference of having a μ that is constant, i.e. insensitive to variations in pressure and sliding velocity. Model 7 is discussed separately from the other models and analyzed for a constant value of μ ranging from 0.05 to 0.12 with increments of 0.01. The properties of the models are summarized in Table 5.1.

Table 5.1 Summary of model properties

	Model[1]						
Modeling aspect	1	2	3	4	5	6[2]	7[3]
Normal force	x			x	x	x	x
Bidirectional coupling	x		x		x	x	x
Large deformations	x		x	x		x	x
Fiction coefficient	x		x	x	x	x	

[1] 'x' denotes exact modeling
[2] Concave dish of the FPS at the bottom
[3] Seven models with value of μ ranging from 0.05 to 0.12 with increments of 0.01

5.5 Dynamic Analyses

The modal properties of the SIB in Model 1 are established by assigning linear effective stiffness to the FPS isolators. The first three modes of vibration are those involving the isolation system which shows that the characteristics and the design of the FPS isolators govern the dynamic response of the bridge (Figure 5.5). The first three modal periods of the SIB are 2.22 s, 2.15 s, and 1.93 s, respectively. The first mode is longitudinal, the second mode is transverse and the third mode is torsional.

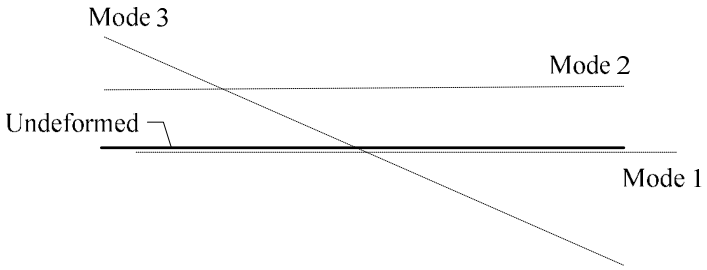

Figure 5.5 Mode shapes of the deck.

Seismically isolated bridge (SIB) models were subjected to NLTH analyses. OpenSees allows the user to select the integration technique and solution algorithm for the analysis. Newmark's average acceleration time-stepping scheme, which is an unconditionally stable numerical integration algorithm, was used in integrating the nonlinear dynamic equilibrium equations. The equations of motion were solved numerically using the Newton-Raphson method. The time interval for solving the equations of motion was taken as 0.005 s.

An important recommendation by the bridge engineering community is the use of design earthquakes that have a 2% probability of exceedance in 50 years (an earthquake with a mean recurrence interval of 2475 years) (FEMA 1997). A suite of ten earthquake

records from rock sites is used in the NLTH analysis of the bridges (Table 5.2). The geometric mean of the longitudinal and transverse component of each record is scaled to match the spectral value of 0.118g at a period of 2.22 s corresponding to a 2% probability of exceedance in 50 years hazard level earthquake in Memphis, TN. The response spectra of the scaled ground motion records for 5% damping, ξ, and their median are given in Figure 5.6.

Table 5.2 Ground motion suite

		Component PGA (g)			
No.	Earthquake record	Longitudinal	Transverse	Vertical	Scale
1	Morgan Hill 1984/04/24	0.098	0.069	0.092	7.932
2	Northridge 1994/01/17	1.285	1.585	1.229	0.767
3	Whittier Narrows 1987/10/01	0.304	0.199	0.227	3.279
4	Loma Prieta 1989/10/18	0.473	0.411	0.209	1.263
5	Gazli, USSR 1976/05/17	0.718	0.608	1.264	0.421
6	N. Palm Springs 1986/07/08	0.492	0.612	0.471	1.434
7	Helena, Montana 1935/10/31	0.173	0.15	0.102	3.654
8	Loma Prieta 1989/10/18	0.453	0.501	0.507	1.248
9	Nahanni, Canada 1985/12/23	0.978	1.096	2.086	0.787
10	Landers 1992/06/28	0.721	0.785	0.818	0.552

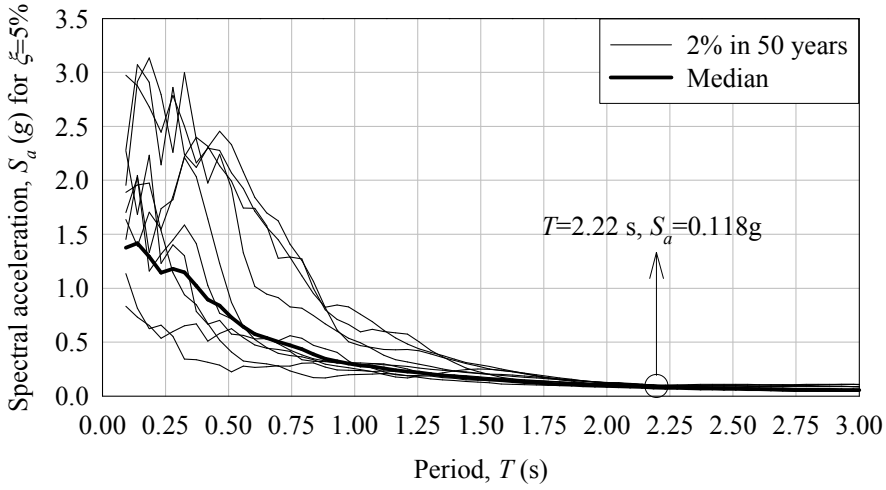

Figure 5.6 Response spectrums for the suite of ground motions.

The three components of the acceleration histories of each scaled ground motion are applied to the SIB models (Figure 5.7). The in-plane orthogonal components of the earthquakes are oriented to result in the maximum demands on the columns for all cases. The SIB models were first analyzed for gravity loads and sequentially subjected to NLTH analyses using simultaneously the longitudinal, transverse and vertical acceleration records of the given earthquake. It is found from the gravity load analysis that each isolator above the pier and the abutments carry a gravity load , N_o, of approximately 125 kN and 258 kN respectively (neglecting the normal load variation between the isolators at the exterior and the interior ends at the same pier and abutment).

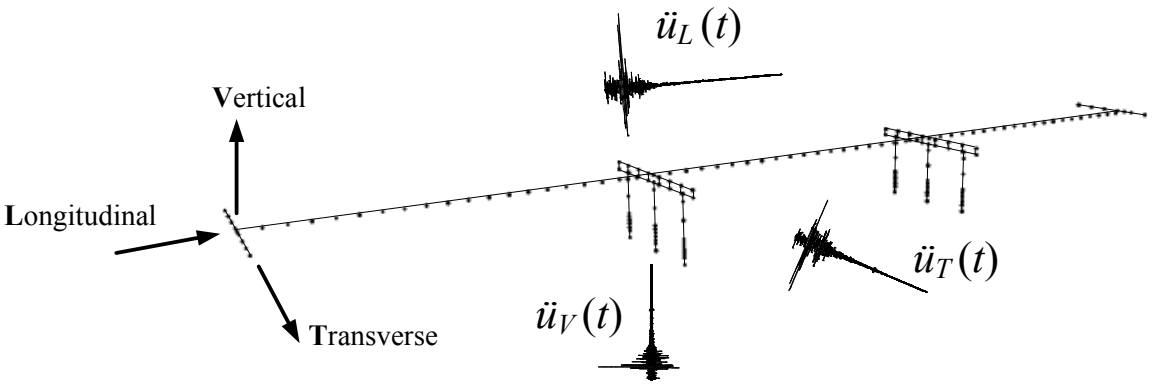

Figure 5.7 Orientation of the 3-D bridge model.

The structural response of the isolators and columns along the same transverse axis were essentially the same. Therefore, the results are presented for one of the isolators on top of the piers and the abutments and one of the columns. The main response quantities monitored for the FPS isolators are the maximum normalized force, MNF = max($\sqrt{f_L^2 + f_T^2} / N_o$), where f_L is the longitudinal and f_T is the transverse isolator force, respectively, and the maximum normalized displacement, MND =

$\max(\sqrt{\delta_L^2 + \delta_T^2}/R)$, where δ_L is the longitudinal and δ_T is the transverse isolator displacement, respectively, for the FPS above the pier. Maximum column drifts, d_{max}, are selected as the response quantity to monitor the structural demands on the SIB.

5.6 Results

It was observed from the NLTH analyses of Model 1 that the maximum allowable displacements at the expansion joints were exceeded in an all records except Morgan Hill, Gazli and Nahanni. This indicates that pounding would occur between the abutment and the deck in the longitudinal direction. The impact forces in the deck are difficult to correlate to damage levels and may impede the utilization of the full capacity of the isolators. Additionally, uplift took place between the sliding surfaces of the FPS isolators in the vertical direction for all of the records except for the Loma Prieta, Helena and Landers. The time-history of the N/N_o of the Model 1 FPS isolator for the Nahanni earthquake is given in Figure 5.8. The maximum allowable N is limited by the allowable pressure of 310 MPa on the slider, which corresponds to N/N_o=5.4. This ratio was not exceeded during any of the NLTH analyses, however, during the Nahanni earthquake a peak value of N/N_o=3.51 was reached. This substantial increase is indicative of a proportional increase in the post-yield stiffness and yield force of the isolator. It is observed from Figure 5.8 that the contact between the two sliding surfaces was lost at least once which resulted in N/N_o=0. This uplift caused instantaneous yet complete loss of stiffness of the isolators during the earthquakes. However, due to the indeterminacy of the model there was no instability.

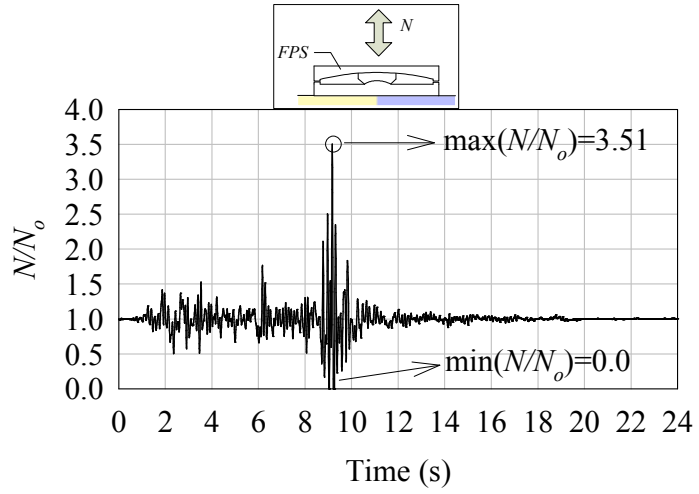

Figure 5.8 Time history of the N/N_o for the FPS during the Nahanni earthquake NLTH analysis.

Figure 5.9 shows the normalized force-deformation (NF-ND) histories of the FPS isolators on top of the piers among Models 1 to 4 in the longitudinal direction of the bridge during the N. Palm Springs record. Model 1 can capture the abrupt changes in isolator force and instances of uplift in the vertical direction. These two aspects of the isolator response could not be observed in Model 2. Additionally, Model 2 underestimated both the MNF and the MND in comparison to Model 1. These differences between Model 1 and Model 2 NF-ND histories can be explained by the response observed in Models 3 and 4. Model 3 was unable to capture peak isolator forces indicating that the normal components of the ground motion were influential in this response quantity. Although Model 4 was able to account for the significant variations in isolator forces, the peak isolator force was overestimated and the peak isolator deformation was underestimated. This implies a stiffer isolator response when the bidirectional effects are neglected.

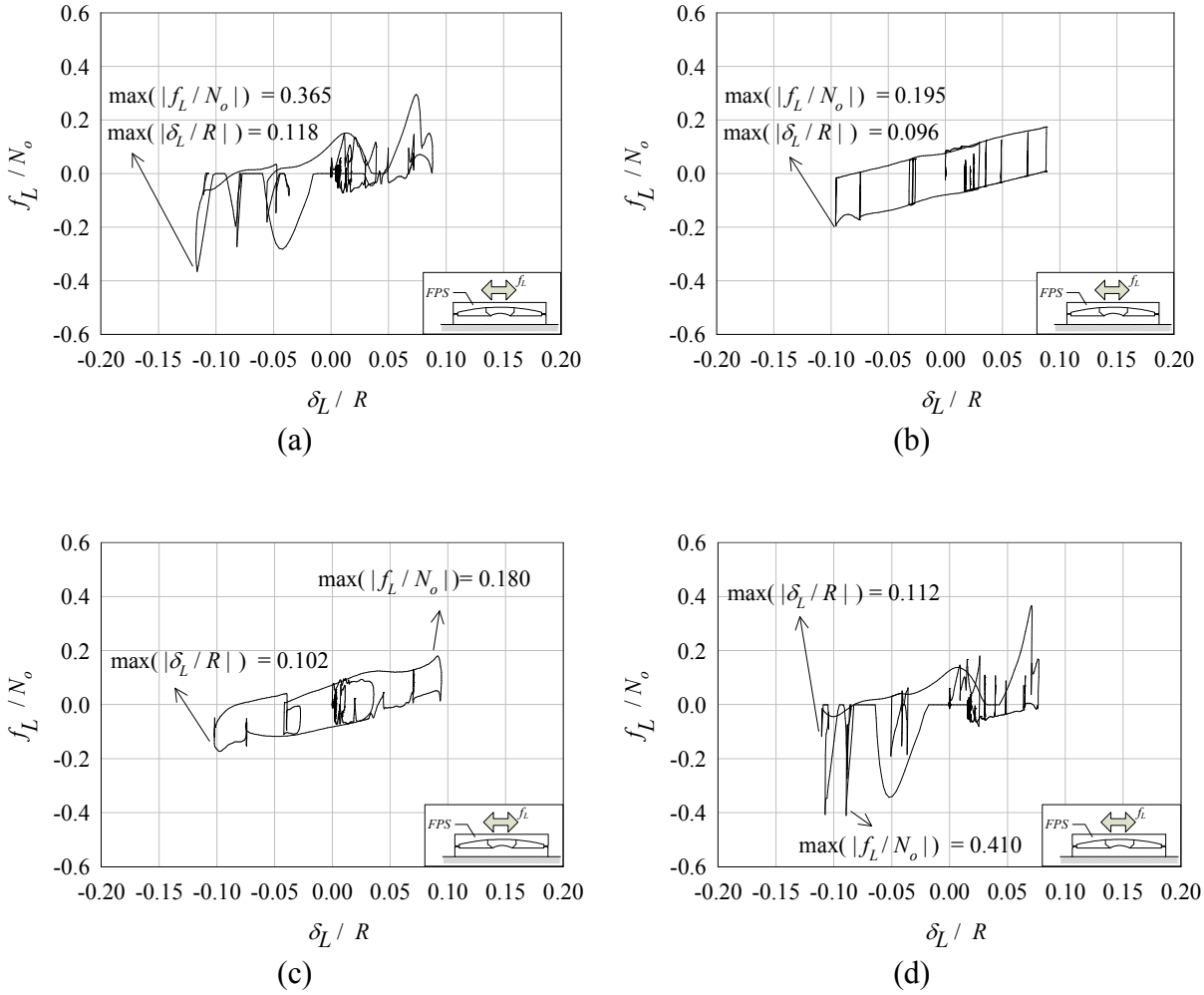

Figure 5.9 Force-deformation history of the FPS in the longitudinal directions on top of the pier for the N. Palm Springs earthquake record with (a) Model 1 (b) Model 2 (c) Model 3 and Model 4.

The influence of the isolator modeling parameters on MNF, MND and d_{max} for the suite of ground motions is illustrated via box plots given in Figure 5.10. Box plots are a useful way of presenting the graphical description of variability of data (Montgomery 2005). This information provides an overview of the expected demands on the isolators

and the structural system as well as the scatter in the results. The statistical interpretation of the results are presented with numerical values of the median and plots of the 10^{th}, 25^{th}, 10^{th}, 75^{th}, and 90^{th} percentile cumulative probabilities.

It is observed that Model 2 underestimated the median of the MNF by 20% and the peak MNF as 44% of Model 1. Similar results were observed for Model 3 which indicated that the normal components of the force are influential in design level isolator forces. It was observed that not including the influence of the variations in the normal forces acting on the isolators causes a loss in the variability of the MNF results. Peak MND values for Models 2 to 7 had negligible difference with Model 1. However, there was a notable variation in the median values of the MND as a function of the magnitude of the constant value of μ. This effect is elaborated in the subsequent section. Model 2 overestimated the median of the d_{max} by 12% and underestimated the peak d_{max} as 69% of Model 1. The absence of the variability in the d_{max} with Model 2 stems from the inability to account for normal force variations on the isolators. On the other hand, Model 2 attained a general increase in the median of the d_{max}, which is attributed to the overestimation of the stiffness caused by uncoupled response in the orthogonal directions of the isolator lateral motion. Another factor that contributed to the increase in the median of the d_{max} in Model 2 was not accounting for the variation of the μ. Models 5 and 6 predicted the MNF, MND and d_{max} approximately the same as Model 1 for the whole suite of ground motion records. The exclusion of the exact kinematics pertaining to the concavity of the FPS in Model 6 was insignificant since the MND was limited to 0.19 for the suite of ground motions. It is concluded that large deformation effects associated with the orientation and exact kinematics were not significant in the response where average MND was smaller than 0.20.

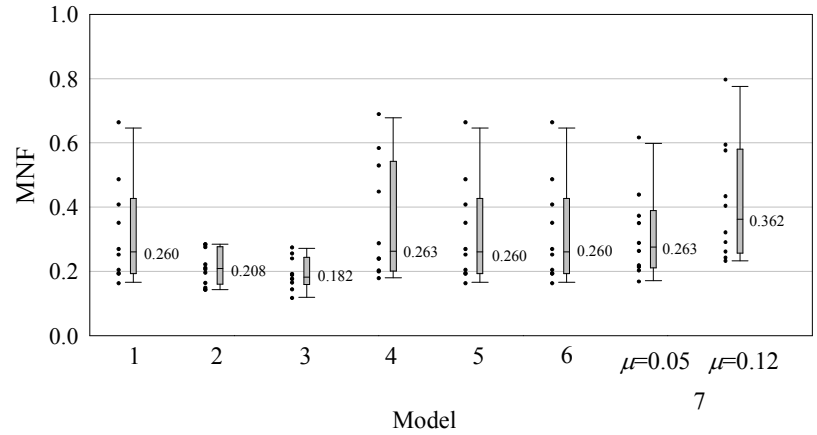

(a)

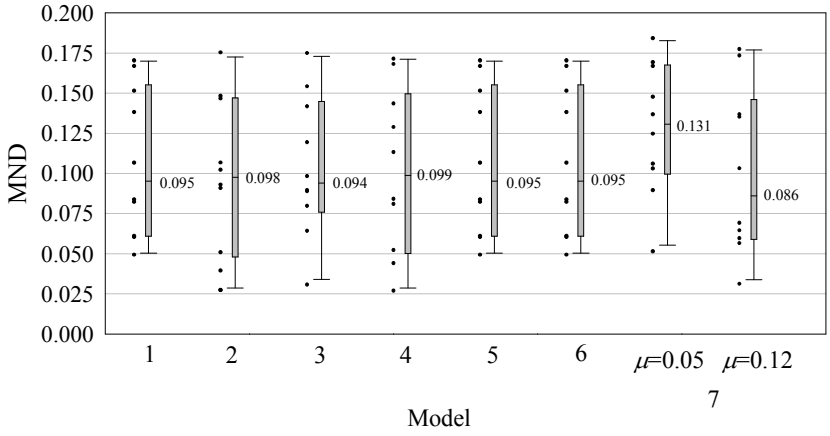

(b)

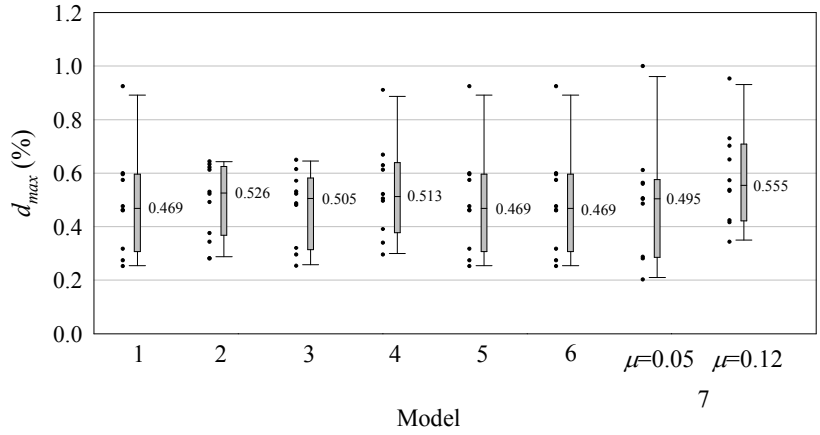

(c)

Figure 5.10 The influence of modeling assumptions on (a) MNF; (b) MND; and (c) d_{max}.

The influence of different magnitudes of μ in Model 7 on MNF, MND and d_{max} for the suite of ground motions is illustrated via box plots given in Figure 5.11. It is observed that both the median and the peak MNF for the suite of ground motions increase consistently with increasing values of μ. Although the median MND generally decreases with the decreasing values of μ, the peak MND remains essentially the same. However, there is a notable increase in the variability of MND with increasing values of μ. The peak and median of the d_{max} are for all values of μ overestimated by Model 7 in comparison to Model 1. The peak and median of the d_{max} attain optimal values at $\mu =$ 0.08 and $\mu = 0.09$, respectively.

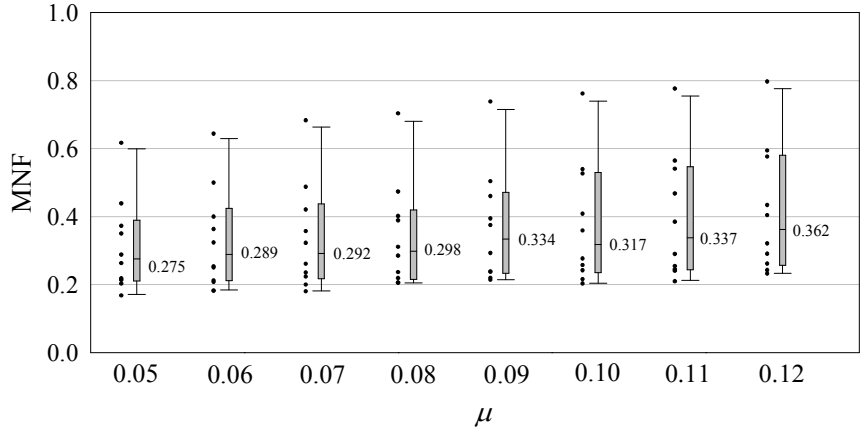

(a)

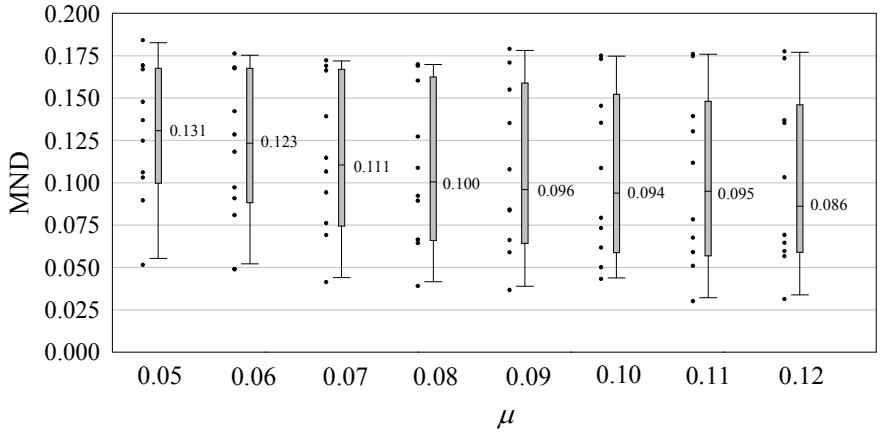

(b)

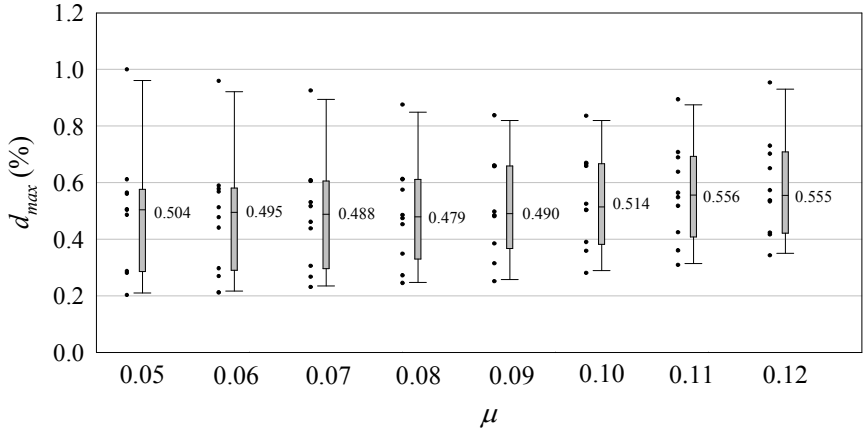

(c)

Figure 5.11 The influence of constant value of μ assumptions on (a) MNF; (b) MND; and (c) d_{max}.

Smaller N_o developed in the FPS isolators at the abutments than at the piers due to the difference in the corresponding tributary mass of the superstructure. Figure 5.12 shows the comparison of the total MNF transferred to the pier, ΣMNF_{pier}, and the total MNF transferred to the abutment, $\Sigma MNF_{abutment}$; and MND on top of the pier, MND_{pier}, and abutments, $MND_{abutment}$ for the suite of ground motions. It is observed that the isolators transferred almost twice as large as the force to the piers in comparison to the abutments on the median. On the other hand MND_{pier} were approximately 16% less than $MND_{abutment}$ on the median. This indicates that the deck engaged into torsional vibration. Abutments may be further engaged into resisting earthquake induced loads in SIB by designing the FPS isolators at the abutments with higher stiffness properties.

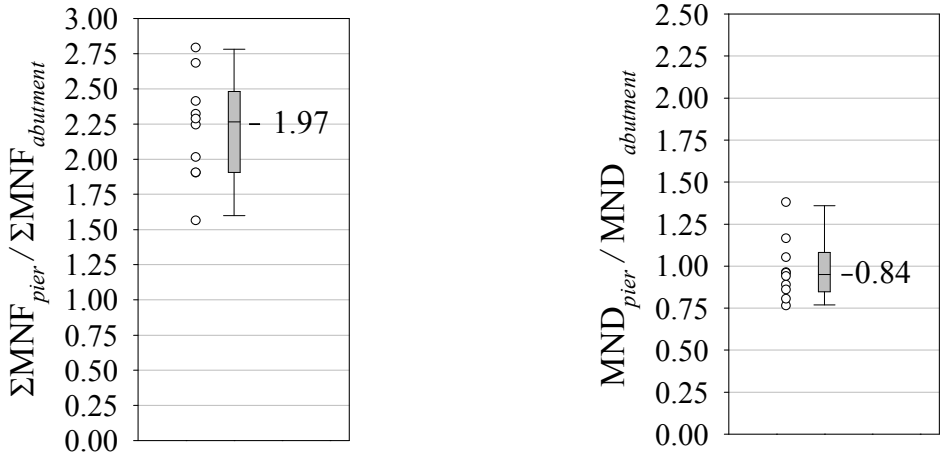

Figure 5.12 Comparison of the (a) total MNF transferred to the pier, ΣMNF_{pier}, and the total MNF transferred to the abutment, $\Sigma MNF_{abutment}$; (b) MND on top of the pier, MND_{pier}, and abutments, $MND_{abutments}$.

5.7 Conclusion

In this chapter, the modeling of a typical highway bridge seismically isolated with the FPS has been presented. The influence of FPS modeling assumptions on normal force, N, and friction coefficient, μ, orthogonal coupling and large deformation, P-Δ, effects in a seismically isolated multi-span continuous (MSC) steel girder bridge has been highlighted via nonlinear time-history (NLTH) analyses. The following conclusions are made:

(1) The simplified bilinear idealization of the FPS response was unable to capture the variability in the results. This model underestimated the maximum column drifts (d_{max}) by up to 31%. This was mainly a result of not accounting for the effects of vertical components of ground motions, bidirectional coupling and the variable magnitude of the friction coefficient.

(2) The uplift and pounding of the deck in the vertical direction had notable affects in the response of the FPS that in one case caused an increase of up to 3.51 times in the initial gravity load acting on the isolators (N_o).

(3) Excluding the bidirectional coupling of the FPS isolators generally resulted in overestimating the isolator maximum normalized forces (MNF) and underestimating the isolator maximum normalized displacements (MND). This indicates an overestimation of the stiffness of the isolators.

(4) The incorporation of the effects of orientation and the exact concave geometry of the FPS in to the response had negligible affects. This is mainly a result of the MND remaining under 0.20 for the suite of ground motions.

(5) The peak MND of the isolators among the suite of ground motions acquired negligible variations among all the modeling assumptions. However, the median MND was influenced by the assumptions in the magnitude of μ.

(6) The structural demands transferred by the isolators to the abutments and the piers were significantly different. Abutment forces were twice of those at the piers in the

median and the isolators acquired 18% larger deformations in the median at the abutments in comparison to those at the piers. This is a results of the uneven distribution of isolator stiffness properties along the bridge as a function of deck tributary mass.

CHAPTER 6

COMPARATIVE ASSESSMENT OF SLIDING VERSUS ELASTOMERIC SEISMIC ISOLATION FOR TYPICAL MULTI-SPAN BRIDGES

6.1 Introduction

This chapter compares sliding versus elastomeric seismic isolation of a typical Multi-Span Continuous Concrete Girder (MSCCG) bridge with advanced isolator models. The Friction Pendulum System (FPS) and the Lead Rubber Bearing (LRB) are selected as representative examples of sliding and elastomeric isolators, respectively. Isolators serve the common objective of lengthening the period of the structure and providing additional energy dissipation, however there exists considerable differences in their mechanisms. In spite of existing research findings on the dependency of LRB in-plane response to the magnitude of in-plane deformation and normal load, existing nonlinear models do not account for these effects. A detailed isolator model for the LRB that can account for the in-plane and vertical coupling of the response is developed in OpenSees. Particular emphasis is given to the distinct vertical load dependency modeling of the isolators. A seismic evaluation of the bridge, isolated in one case with the LRB and in another case with the FPS, is performed for a hazard level of 7% in 75 years using a nonlinear three-dimensional (3-D) analytical model. Maximum isolator forces and displacements, and column drifts are selected as response quantities.

6.2 The Lead Rubber Bearing (LRB)

The Lead Rubber Bearing (LRB) was invented in April 1975 by W H Robinson (Skinner et al. 1993). The LRB is one of the most commonly used elastomeric isolator

types in bridges (Buckle and Mayes 1990) (Figure 6.1). Analytical and experimental research and observed performances of bridges during earthquakes isolated with the LRB showed that the LRB may have a substantial impact on improving the structural performance of bridges prone to seismic loads (Jangid 2004; Kelly and Buckle 1986; DIS 1996; Lee et al. 2002; Ghobarah 1988). It has been also reported based on information provided by the manufacturers that the cost, size and energy dissipation of the FPS and LRB may be comparable in bridge applications (Dicleli, M 2002). Additionally, both isolators have been incorporated into the design codes (AASHTO 1999; International 2000).

(a)

(b)

Figure 6.1 Examples of LRB applications (a) Rio Vista Bridge, Califonia (b) Patria Acueducto, Mexico (courtesy of Dynamic Isolation Systems).

The LRB consists of steel plates, rubber and a lead core (Figure 6.2). A lead core is inserted in the center of the bearing for energy dissipation and stiffness (Priestley et al. 1996). Lead is a feasible option because it yields in shear at relatively low stresses, 10 MPa, and has good fatigue properties (Skinner et al. 1993). The steel layers placed between the rubber serves to limit the edge-bulging of the rubber (Tyler 1991). Additionally, the steel plates force the lead plug bearing to deform in shear (Naeim and Kelly 1996). The force-deformation response of the LRB is typically idealized as bilinear (Ghobarah 1987; AASHTO 1999; Naeim and Kelly 1996). The LRB provides the advantage of attaining versatile force-deformation characteristics via the geometrical variations of both the lead core and the rubber (see Figure 6.3) (Priestley et al. 1996).

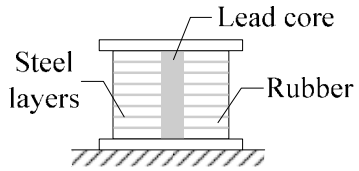

Figure 6.2 The Lead Rubber Bearing (LRB) interior elevation.

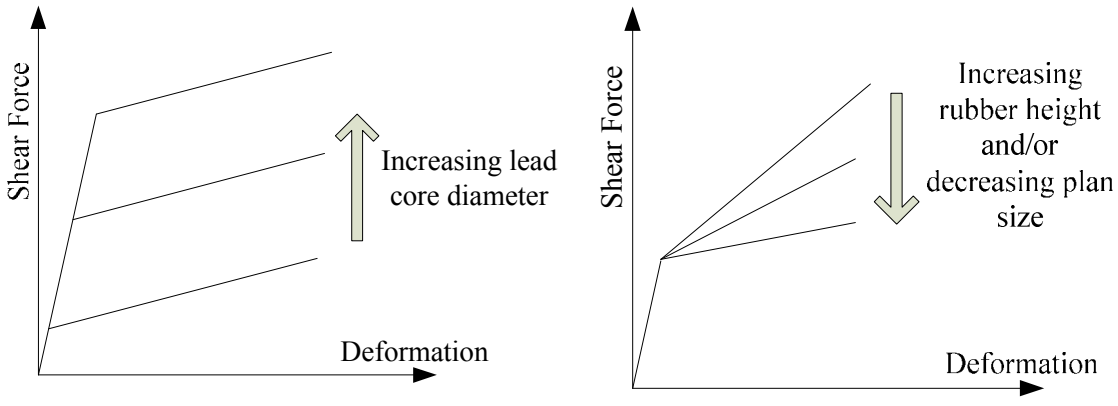

Figure 6.3 Effects of geometrical variations of the LRB on the force-deformation response (Priestley et al. 1996).

6.3 Force-Deformation Characteristics of the LRB

As a multilayered elastomeric type bearing, the LRB is susceptible to a buckling type of instability (Kelly 1997). The critical buckling load established from the elastic theory in undisplaced position is (Naeim and Kelly 1996):

$$P_{cro} = \sqrt{P_s P_e} \tag{6.1}$$

where

$$P_s = GA \tag{6.2}$$

and

$$P_e = \frac{\pi^2 (EI)_{\text{eff}}}{t_r^{\,2}} \tag{6.3}$$

where G is the shear modulus of the rubber, t_r is the total thickness of the rubber, A is the cross-sectional area of the isolator and $(EI)_{\text{eff}}$ is the effective rigidity. The critical buckling load capacity of the LRB reduces as the isolator deforms (Buckle and Liu 1993):

$$P_{cr} = P_{cro}\left[1 - \frac{\delta}{D}\right] \tag{6.4}$$

where D is the diameter of the isolator and δ is the lateral bearing displacement.

The LRB response softens and yield force increases with increasing level of N (Ryan and Chopra 2005). The post-yield stiffness of the LRB as a function of the N is (Buckle and Kelly 1986):

$$k_{p,LRB} = k_{po}\left[1 - \left(\frac{N}{P_{cr}}\right)^2\right] \tag{6.5}$$

where stiffness k_{po} is the nominal (meaning absent of N effects) post-yield stiffness. If the large deformation (P-Δ) effects described in Chapter 4 are neglected, the post yield stiffness of the FPS is:

$$k_{p,FPS} = \frac{N}{R}$$

The yield force of the LRB was observed to not achieve the theoretical strength under low N (Hwang and Hsu 2000). The yield force of the LRB is approximated as (Ryan and Chopra 2005):

$$F_{Y,LRB} = F_{Y\,\mathrm{o}}\left[1 - \mathrm{e}^{(-N/P_o)}\right] \tag{6.6}$$

where $F_{Y\,\mathrm{o}}$ is the nominal yield strength of the isolator which can be computed from the yield stress of the lead core, and P_o is the normal load corresponding to approximately 63% of nominal strength. The initial elastic stiffness of the LRB, $k_{i,LRB}$, is typically estimated as $10k_{p,LRB}$ (Naeim and Kelly 1996). The yield displacement of elastomeric isolators is typically larger compared to sliding isolators (Matsagar and Jangid 2004). The yield strength of the FPS is (Earthquake 2003):

$$F_{Y,FPS} = N\,\mu \tag{6.7}$$

The LRB compression stiffness is (Naeim and Kelly 1996):

$$k_v = \frac{E_c A}{h} \tag{6.8}$$

where E_c is the compression modulus and h is the total isolator height. The stiffness of the LRB remains elastic under tension with the same magnitude as in compression until reaching cavitation at strains $\varepsilon_c = 1/(2S^2)$, where S is the shape factor of the isolator (Kelly 2003; Mori et al. 1996). This behavior closely matches the response of a zero-length symmetrically elastic element bound by P_{cr} under compression and ε_c under tension:

$$f_e = \begin{cases} k_e\delta_e & \text{for} \quad \text{buckling} < \delta_e \le 0 \\ -k_e\delta_e & \text{for} \quad 0 < \delta_e < \text{cavitation} \end{cases} \tag{6.9}$$

where k_e is the vertical stiffness of the elastic element equal to that of the isolator, δ_e is the elastic deformation with a (-) and (+) sign for tension and compression, respectively.

This is a similar approach adopted for modeling of the FPS vertical response in Chapter 4.

6.4 Modeling of the Isolator Response

The bilinear idealization of the LRB force-deformation response is based on similar simplifications adopted for the bilinear idealization of the FPS response: (1) N is constant; (2) $F_{Y,LRB}$ is constant; (3) the horizontal response is uncoupled in the orthogonal directions; and (4) isolator deformations are small. It is possible to extend the model developed in Chapter 4 for the FPS to represent the nonlinear and coupled response of the LRB using the relationships described in the previous section.

The hysteretic force-deformation response of the LRB is modeled by implementing a 3-D zero-length *element* class and a complimentary *material* class in OpenSees. The procedure for this approach is essentially the same as the FPS modeling described in Chapter 4. The only difference is in evaluating the post-yield stiffness, yield force, and vertical response from Equations (6.5), (6.5) and (6.9), respectively. The large deformation affects are assumed to be negligible (as described in Chapter 5). The FPS model developed in Chapter 4 is used in the subsequent analyses with the only additional assumption of neglecting large-deformation effects. It has been shown that excluding the in-plane coupling of the orthogonal response for the LRB may result in significant underestimation of the displacements and forces (Jangid 2004). Consequently, this interaction is included in the response of the LRB using the methodology described in Chapter 4. In retrospect, the general force-deformation relationship in the x, y, and z directions for the FPS and the LRB are:

$$\mathbf{f} = \begin{bmatrix} f_x & f_y & f_z \end{bmatrix}^{\mathrm{T}} = \begin{bmatrix} k_p \delta_x + F_Y \eta_x & k_p \delta_y + F_Y \eta_y & N \end{bmatrix}^{\mathrm{T}} \tag{6.10}$$

where f and δ are the isolator forces and displacements in the direction denoted with the subscript, k_p is the post-yield stiffness, F_y is the yield force described by corresponding Equations in the previous section for the two isolators (Figure 6.4).

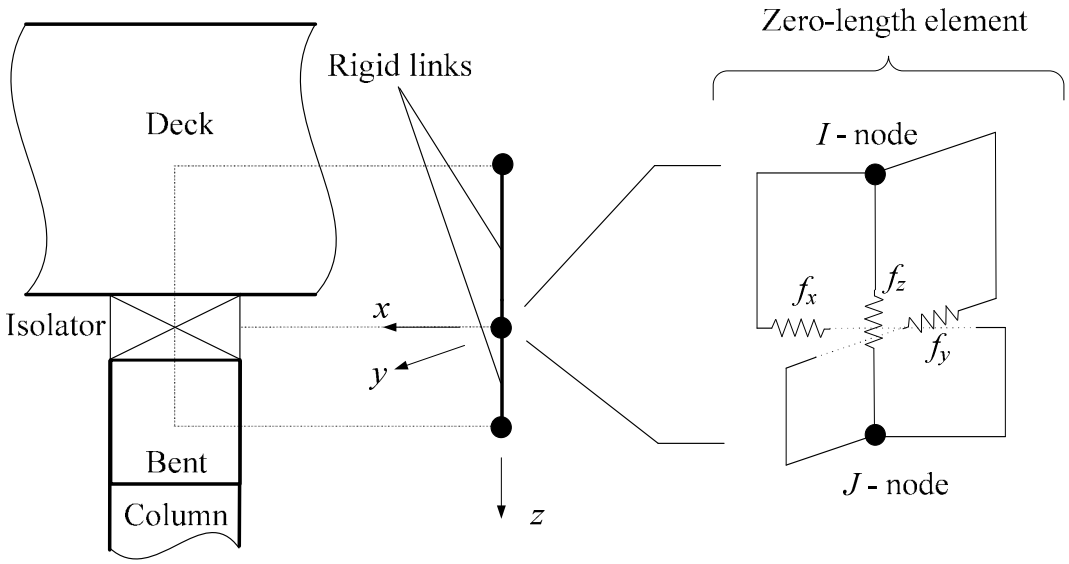

Figure 6.4 Isolator model.

6.5 Bridge Model

The Multi-Span Continuous Concrete Girder (MSCCG) bridge considered in this Chapter is essentially the same with the one used in Chapter 5 with the only difference in the geometric and material properties of the superstructure. The superstructure is comprised of a continuous slab-on-girder concrete deck with a total of eight concrete girders. The superstructure is expected to remain within the linear elastic range and modeled as a beam element. The total weight of the superstructure is W=12272 kN with a moment of inertia about the strong and weak axes as I_y=75.03 m^4 and I_x=0.12 m^4 and modulus of elasticity of E_c=25.6 GPa. Additionally, the pounding between the deck and

the abutments are neglected to focus on the differences in the response of the two isolators. Details of the substructure modeling of the bridge are given in Chapter 5.

6.6 Bridge Seismic Isolation

The seismic isolation of the bridge is achieved via placing isolators under each of the eight girders above the piers and abutments. It is assumed that a single isolator size is used throughout the bridge to save on the cost of an extra mold. According to AASHTO (1999) the isolation period is to be determined from the isolation system effective stiffness based on maximum design displacement. Due to the absence of maximum design displacement the period is determined with the k_p of the isolation system. The effective stiffness and k_p are correlative and typically close (Jangid 2004). Additionally, the k_p of the isolators are more influential for the seismic response of bridges compared to the initial stiffness (Dicleli and Buddaram 2005). To achieve a target isolation period of approximately T=2 seconds for a one-degree-of-freedom mass of W=12272 kN the stiffness is 123.7 kN/cm. Assuming an equivalent distribution of superstructure weight on 32 isolators, the stiffness of a single isolator is $k_i = 4.1$ kN/cm with a static weight of $W_i = 387$ kN. An approximate FPS design to match this k_i has R=99 cm and $\mu = 0.05$. The slider diameter is D_s=12.7 cm. The LRB design properties are chosen by considering: (1) a vertical load capacity of at least three times the initial gravity load, N_o, (2) a shape factor S>8 (3) a post-yield stiffness of approximately 4.1 kN/cm (4) a yield force of approximately the same value to the average FPS to acquire a comparative seismic isolation scheme. The following are the properties selected to achieve these design objectives: bearing diameter, D=35.6 cm, lead core diameter, D_c=5.8 cm, single

layer thickness for rubber, t=0.953 cm, number of layers, n=17, shear modulus, G=0.76 MPa of rubber. This design has an S=8.7 and a P_{cro}=1600 kN. The yield displacements for the FPS and the LRB are assumed to be at 0.026 cm and 0.585 cm respectively. The two systems possess a yield force of approximately F_y=19 kN for N=W_i. The variation of the P_{cr} as a function of δ is given in Figure 6.5.

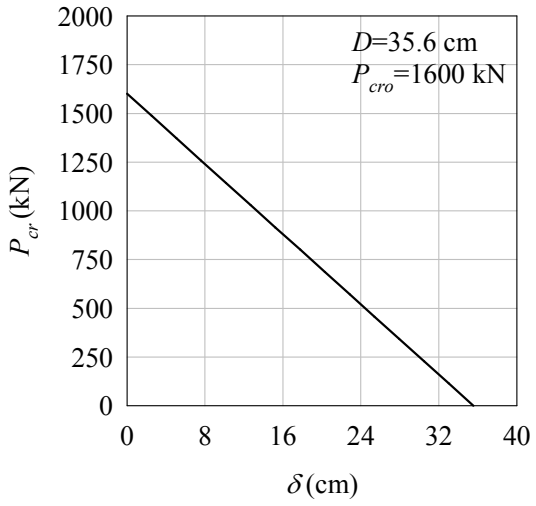

Figure 6.5 Variation of the buckling load, P_{cr}, as a function of isolator in-plane deformation, δ, for the LRB.

Two models of the bridge are generated and one is isolated with the LRB and the other is isolated with the FPS, using the design parameters described above. The yield force, F_y, and post-yield stiffness, k_p, of the two isolators as a function of the N are given in Figures 6.6 and 6.7 respectively. The tributary mass supported by each isolator varies once they are installed into the bridge and subjected to gravity loading. Each isolator above the pier and the abutments carry a gravity load, N_o, of approximately 258 kN and

512 kN respectively (neglecting the load variation between the bearings at the exterior and the interior ends at the same pier and abutment). The corresponding bilinear force-deformation idealization of the two isolation systems after gravity loading is given in Figures 6.8 and 6.9 respectively. It is observed that the FPS sustains a considerable variation of the F_y and k_p throughout the longitudinal axis of the bridge due to corresponding tributary gravity load from the superstructure. The F_y and k_p of the FPS isolators above the piers become twice in magnitude of those above the abutments. Consequently, the isolators above the piers become stiffer and the ones atop the abutments become more flexible compared to the initial design with W_i. Since the rate of dependency of the LRB response to N is weaker compared to FPS, the variation of the F_y and k_p located at different parts of the bridge are smaller. Another notable distinction is that the LRB isolators become stiffer at the abutments and more flexible at the piers compared to design with W_i because the k_p is inversely proportional to N in Equation 6.5.

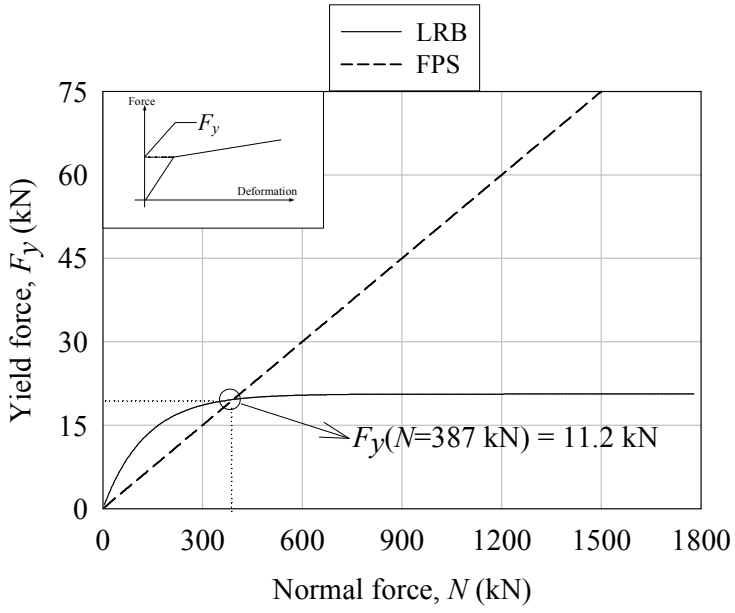

Figure 6.6 Variation of isolator yield force, F_y, as a function of applied compressive axial load, N.

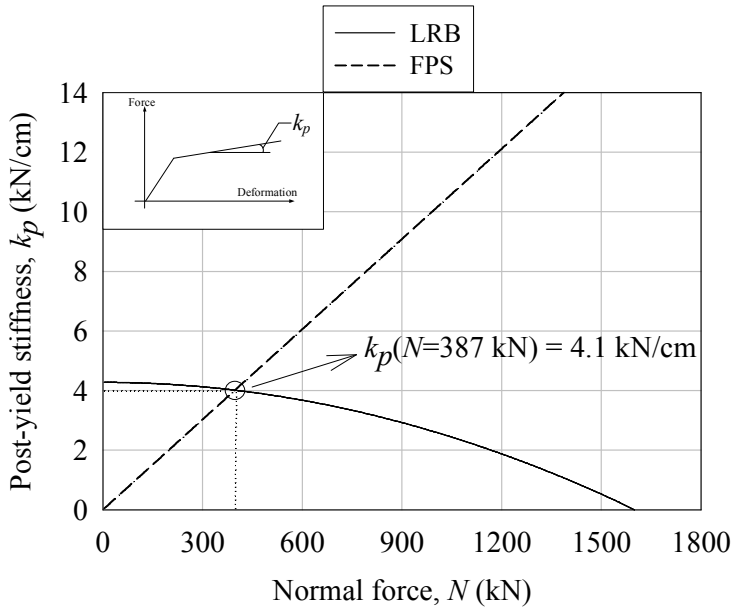

Figure 6.7 Variation of isolator post-yield stiffness, k_p, as a function of applied compressive axial load, N.

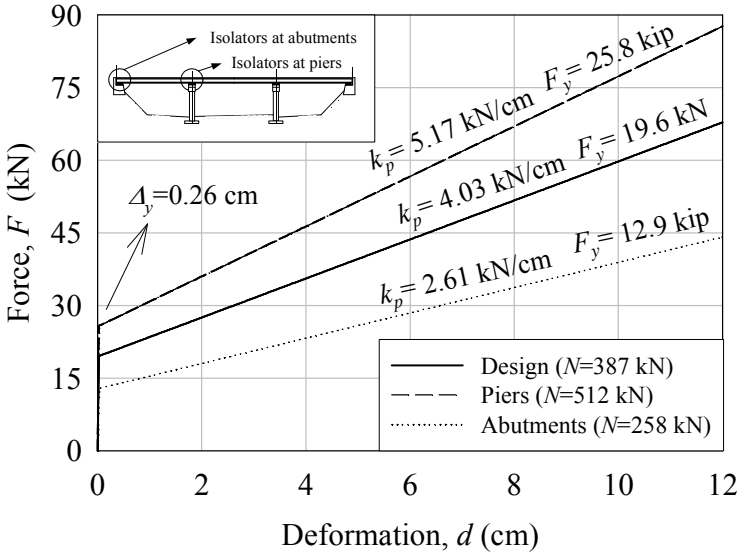

Figure 6.8 Bilinear idealizations of the FPS force-deformation characteristics after gravity loading in the bridge.

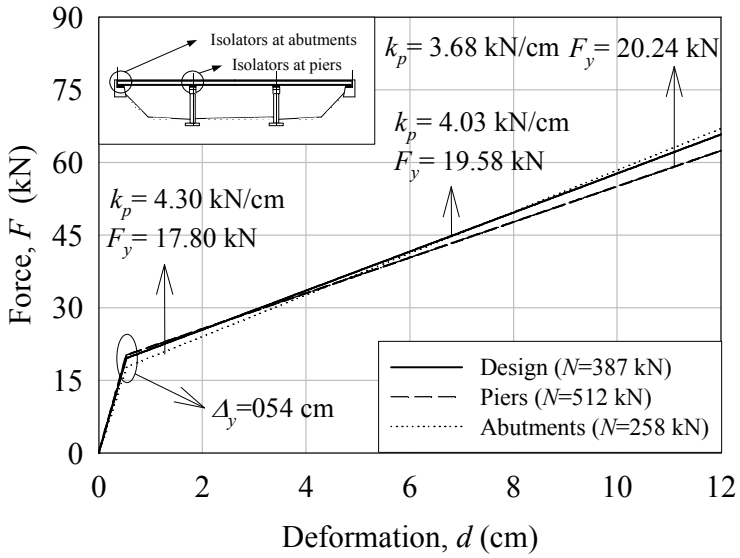

Figure 6.9 Bilinear idealizations of the LRB force-deformation characteristics after gravity loading in the bridge.

6.7 Dynamic Analysis

The structural periods of the two bridges utilizing either FPS or LRB were established per k_p of the isolators. The first three structural periods for the FPS-isolated and LRB-isolated bridge were T_1=2.38, T_2=2.26, T_3=2.00 and T_1=2.30, T_2=2.16, T_3=1.64, respectively. The first three mode shapes were those involving the seismic isolation and were essentially the same for the two bridges (Figure 6.10). The modal characteristics of the two bridges, isolated with the FPS in one case and with the LRB in the other, are considered to be sufficiently close for comparative assessment. A notable distinction among the vibration characteristics of the two bridges arises for the torsional mode, T_3. The FPS-isolated bridge acquired a higher period due to the more flexible isolators at the abutments compared to the LRB-isolated bridge.

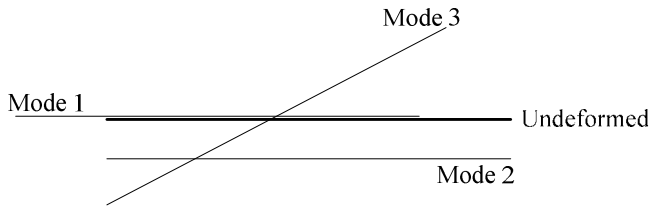

Figure 6.10 Mode shapes of the bridge deck from plan.

A suite of ten earthquake records from rock sites is used in the NLTH analysis of the bridges (Table 6.1). The geometric mean of the longitudinal and transverse component of each record is scaled to match the spectral value of 0.056g at a period of 2.44 s (arithmetic average of the T_1 of the two bridges) corresponding to a 7% probability of exceedance in 75 years hazard level earthquake in Memphis, TN. The response spectra of the scaled ground motion records for 5% damping, ξ, and their median are given in Figure 6.11. The three components of the acceleration histories of each scaled ground motion are applied to the models using NLTH analyses. The in-plane orthogonal components of the earthquakes are oriented to result in the maximum demands on the columns for all cases. The bridge models were also analyzed without the vertical acceleration history component of the ground motions, $\ddot{u}(t)_v$, to examine the effects of N variations on the response of the bridge and the isolators.

Table 6.1 Ground motion suite

No.	Earthquake record	Component PGA (g)			Scale
		Longitudinal	Transverse	Vertical	
1	Morgan Hill 1984/04/24	0.098	0.069	0.092	5.302
2	Northridge 1994/01/17	1.285	1.585	1.229	0.595
3	Whittier Narrows 1987/10/01	0.304	0.199	0.227	2.617
4	Loma Prieta 1989/10/18	0.473	0.411	0.209	0.845
5	Gazli, USSR 1976/05/17	0.718	0.608	1.264	0.290
6	N. Palm Springs 1986/07/08	0.492	0.612	0.471	1.135
7	Helena, Montana 1935/10/31	0.173	0.15	0.102	2.820
8	Loma Prieta 1989/10/18	0.453	0.501	0.507	0.814
9	Nahanni, Canada 1985/12/23	0.978	1.096	2.086	0.500
10	Landers 1992/06/28	0.721	0.785	0.818	0.320

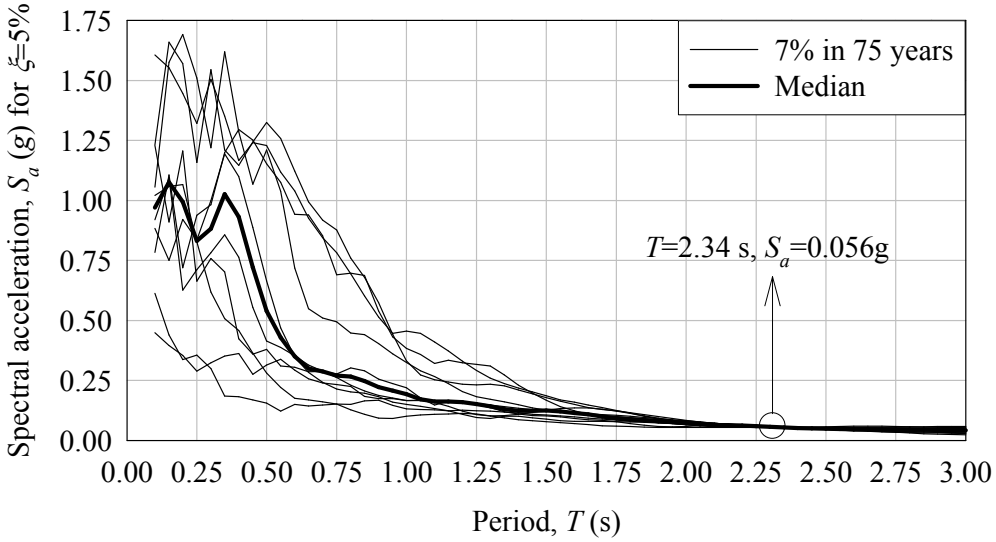

Figure 6.11 Response spectrums for the suite of ground motions.

6.8 Results

The structural response of the isolators and columns along the same transverse axis were essentially the same. Therefore, the results are presented for one of the isolators on top of the piers and the abutments and one of the columns. The main response quantities monitored for the isolators are the: (1) maximum isolator force, MIF = max($\sqrt{f_L^2 + f_T^2}$), where f_L is the longitudinal and f_T is the transverse isolator force, respectively; (2) the maximum isolator displacement, MID = max($\sqrt{\delta_L^2 + \delta_T^2}$), where δ_L is the longitudinal and δ_T is the transverse isolator displacement, respectively; and (3) maximum column drift, d_{max}, in a given earthquake time-history analysis. Maximum and minimum values of other response quantities are denoted by 'max(*response quantity*)' and 'min(*response quantity*)', respectively.

The LRB on top of the piers were observed to buckle ($N>P_{cr}$) under the Northridge earthquake record when the N increase due to $\ddot{u}(t)_v$ and P_{cr} reduction due to isolator deformation was considered in the models. When the bridge was analyzed without the $\ddot{u}(t)_v$ effect on the isolator, the buckling condition ($N>P_{cr}$) of the LRB did not prevail. It is concluded that neglecting the effects of $\ddot{u}(t)_v$ in the isolator model may result in overlooking a fundamental failure mode of the LRB. The f_L - δ_L history of the FPS with and without the $\ddot{u}(t)_v$ effects on the isolator located on top of the pier for the Northridge earthquake record is given in Figure 6.12. The time-history of the N/N_o for the same earthquake is given in Figure 6.13. It is observed that the N/N_o makes a notable drop to 0.14 which is proportional to the decrease of the $k_{p,FPS}$. This effect can be observed in Figure 6.12a as deviation from the idealized bilinear force-deformation path of the isolator. The analysis without the effects of $\ddot{u}(t)_v$ on the isolator models can not account for the increased flexibility of the isolator and consequently underestimated the

max($|\delta_L|$). The maximum allowable pressure stress of 275 MPa at the slider of the FPS was not exceeded in any of the analyses.

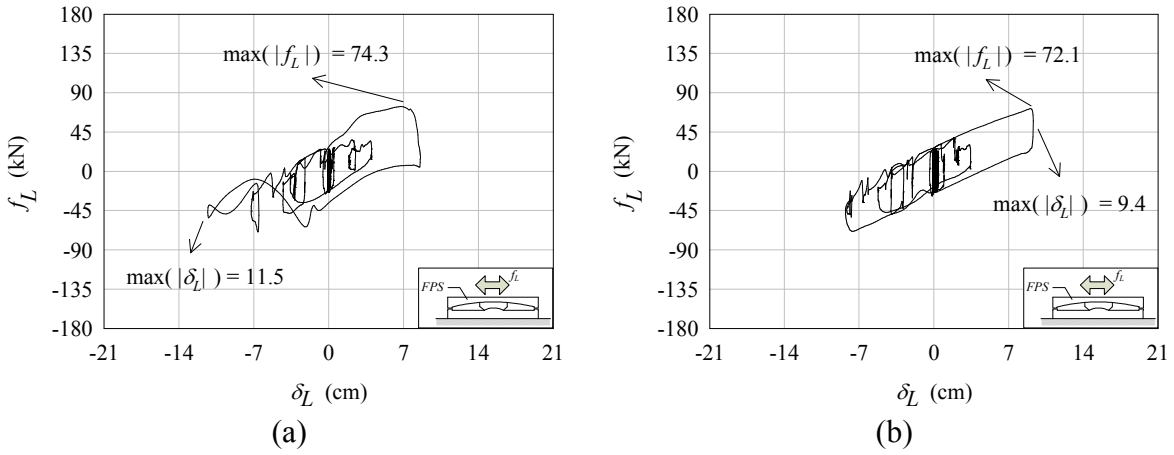

Figure 6.12 Force-deformation history of the FPS in the longitudinal direction on top of the pier for the Northridge earthquake record where the vertical component, $\ddot{u}(t)_v$, effect is (a) included (b) not included.

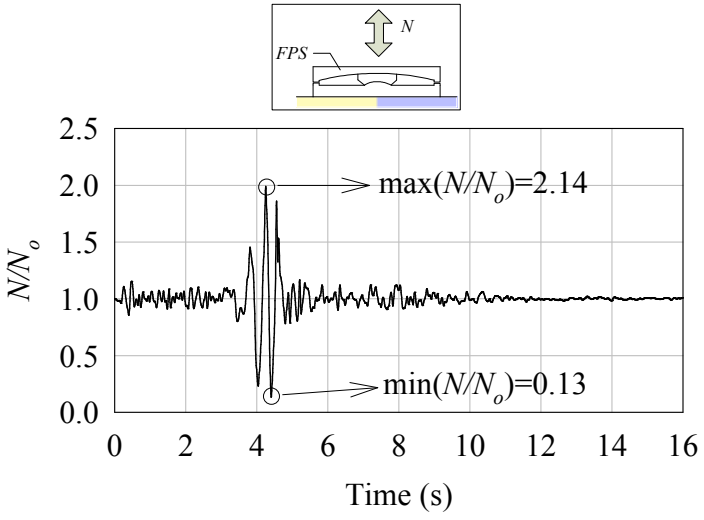

Figure 6.13 Time history of the N/N_o for the FPS during the Northridge earthquake record.

The f_L-δ_L history of the LRB with and without the $\ddot{u}(t)_v$ effect on the isolators located on top of the pier for the Whittier Narrows earthquake is given in Figure 6.14. It is observed that excluding the $\ddot{u}(t)_v$ resulted in an overestimation of the max($|f_L|$) and underestimation of the max($|\delta_L|$). This result can be explained via the time-history of the P_{cr} and the N of the isolator given in Figure 6.15. The reduction factor for the post-yield stiffness, $k_{pf} = 1 - (N/P_{cr})^2$, vary during the earthquake response of the isolator. An increase of the N by the random pulses of the $\ddot{u}(t)_v$ at large deformations compounds the reduction of the P_{cr} and results in smaller k_{pf}. The value of k_{pf} reaches a minimum of 0.27, which increases the flexibility and the MID of the isolator.

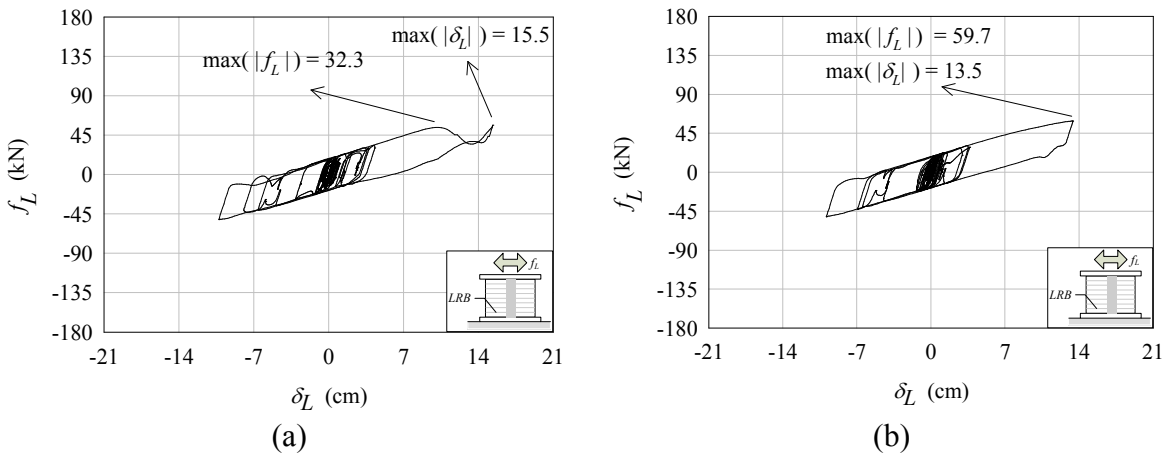

Figure 6.14 Force-deformation history of the LRB in the longitudinal direction on top of the pier for the Whittier Narrows earthquake record where the vertical component, $\ddot{u}(t)_v$, effect is (a) included (b) not included.

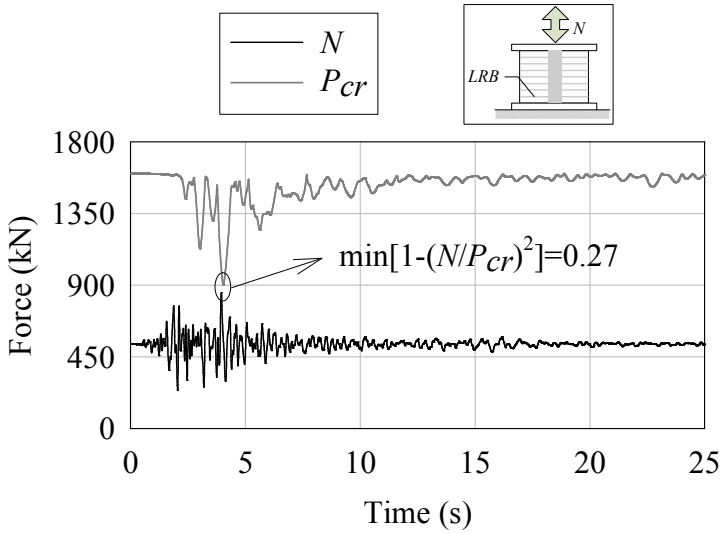

Figure 6.15 Time history of the LRB buckling load, P_{cr}, and normal force, N.

The MID of the LRB may also be overestimated by not including the $\ddot{u}(t)_v$ effect on the isolator models. Figure 6.16 gives the f_L-δ_L and f_T-δ_T of the LRB with and without the $\ddot{u}(t)_v$ effect on the isolator located on top of the pier for the Gazli earthquake. It is observed that although the longitudinal response of the LRB isolator was essentially the same with and without the $\ddot{u}(t)_v$ effect, there was a considerable difference in the transverse direction. The max($|\delta_T|$) with and without the $\ddot{u}(t)_v$ effect on the isolator was 4.4 cm and 8.7 cm, respectively. The reduction in the k_p from higher N corresponded to a more flexible response in the transverse direction thus attracting smaller earthquake induced displacements on the isolators in this direction.

.

$\ddot{u}(t)_{\mathrm{v}}$ included

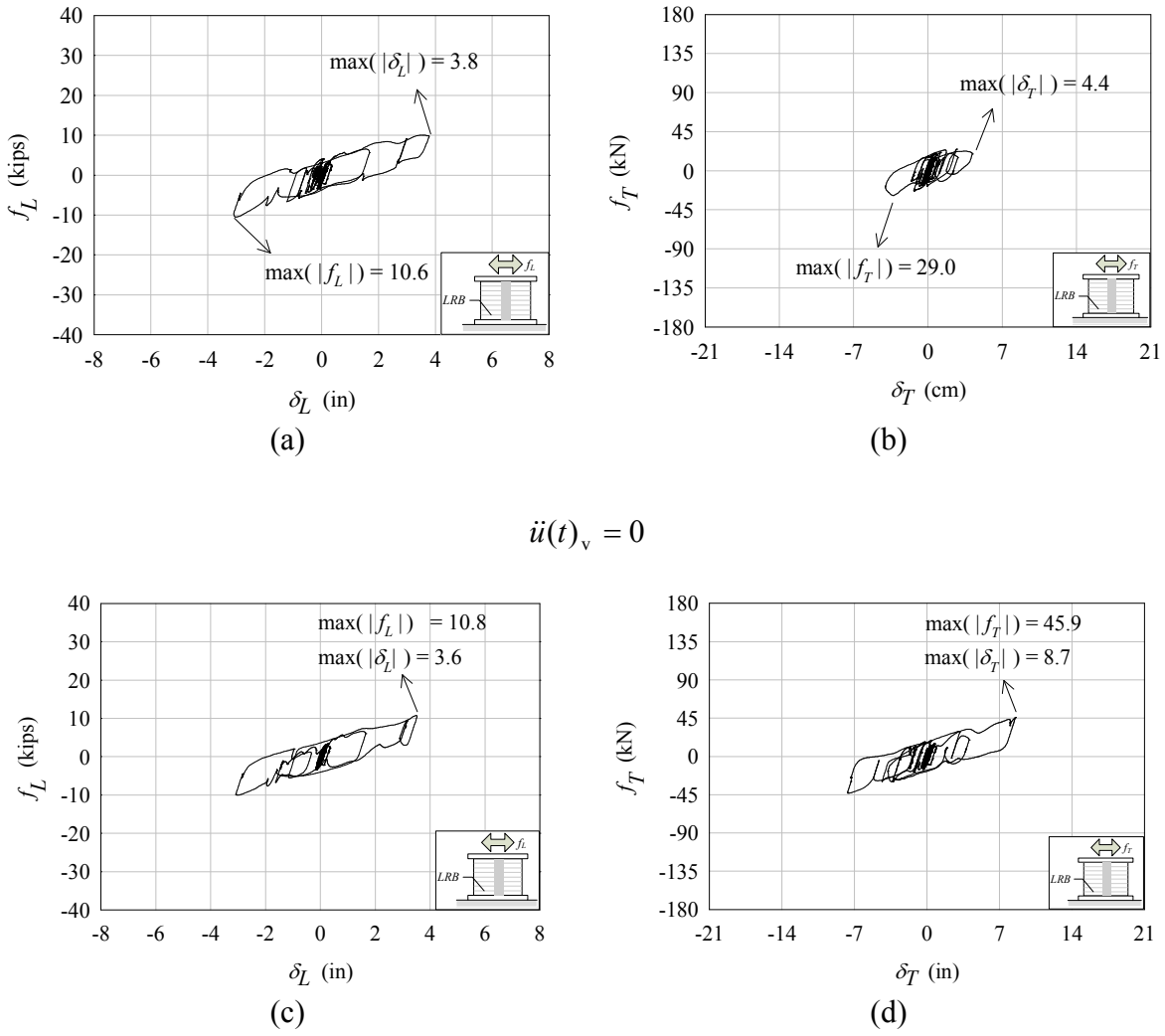

$\ddot{u}(t)_{\mathrm{v}} = 0$

Figure 6.16 Force-deformation history of the LRB on top of the pier for the Gazli earthquake in the (a), (c) longitudinal, and (b), (d) transverse directions.

The f_L-δ_L history of the FPS with and without the $\ddot{u}(t)_{\mathrm{v}}$ effect on isolator the isolator located on top of the pier for the Whittier Narrows earthquake is given in Figure 6.17. It is observed that the exclusion of the $\ddot{u}(t)_{\mathrm{v}}$ resulted in a slight overestimation of $\max(|\delta_L|)$, however, the $\max(|f_L|)$ was underestimated by approximately 47%. The

increase of the N by inertial forces from the $\ddot{u}(t)_v$ resulted in instantaneous but considerable stiffening of the FPS response. Although at no instance was there separation between the two surfaces of the FPS or was the maximum allowable pressure exceeded, the N reached a maximum of 837 kN and a minimum of 290 kN, which corresponds to a 61% increase and a 56 % decrease from N_o respectively.

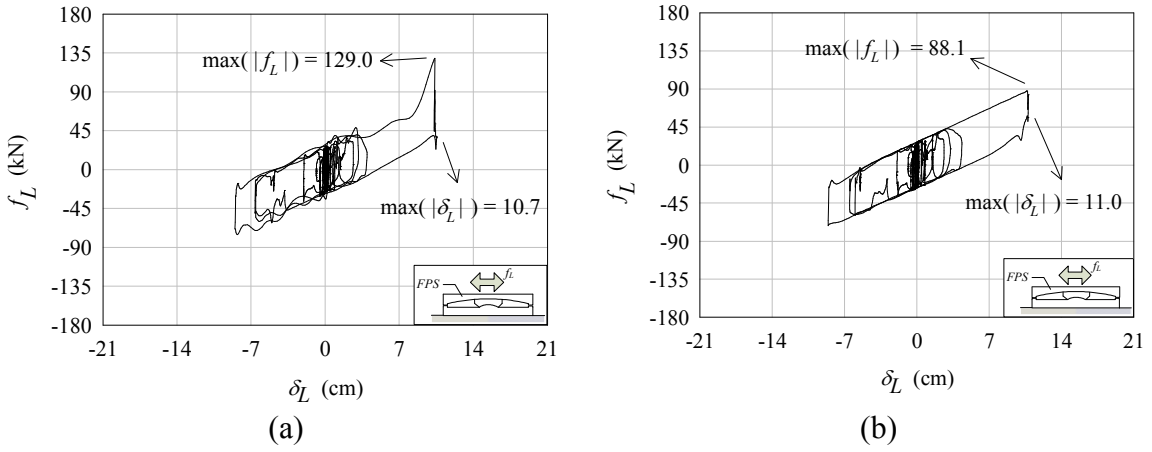

Figure 6.17 Force-deformation history of the FPS in the longitudinal direction on top of the pier for the Whittier Narrows earthquake record where the vertical component, $\ddot{u}(t)_v$, effect is (a) included (b) not included.

It is concluded from the aforementioned results that excluding the normal load-dependency of the isolators in modeling the force-deformation response may produce considerable errors in MIF and MID and mislead to similarities between the FPS and the LRB. The force-deformation histories of the LRB and the FPS given in Figures 11(a) and 14(a) show that there are notable differences in the response of the two isolators. In addition to acquiring a higher initial and post-yield stiffness, the FPS hysteresis has short duration wriggles compared to the LRB. This is attributed to the stronger dependency of

the FPS response to $\ddot{u}(t)_v$. It is observed from Figures 6.14(b) and 6.17(b) that the force-deformation response of the two isolators is smoother and similar to the bilinear idealization when the $\ddot{u}(t)_v$ effects in the isolator models are excluded.

Figure 6.18 illustrates the differences in the force-deformation responses of the FPS and LRB located on the same beam line but on top of the pier and the abutment for the Helena earthquake. It is observed that the longitudinal deformation of both types of isolators is larger at the abutments compared to those at the piers. This is attributed mainly to the torsional vibration of the bridges deck. However, the difference between the abutment and pier isolator deformations is greater for the FPS compared to the LRB. This indicates a larger torsional effect in the response of the FPS-isolated bridge. It is observed that the force-deformation hysteresis of the FPS gets shorter in width and deeper in height on top of the pier compared to the response on top of the abutment. This is an attribute of the strong fluctuation of the $k_{p,FPS}$ and $F_{Y,FPS}$ to N.

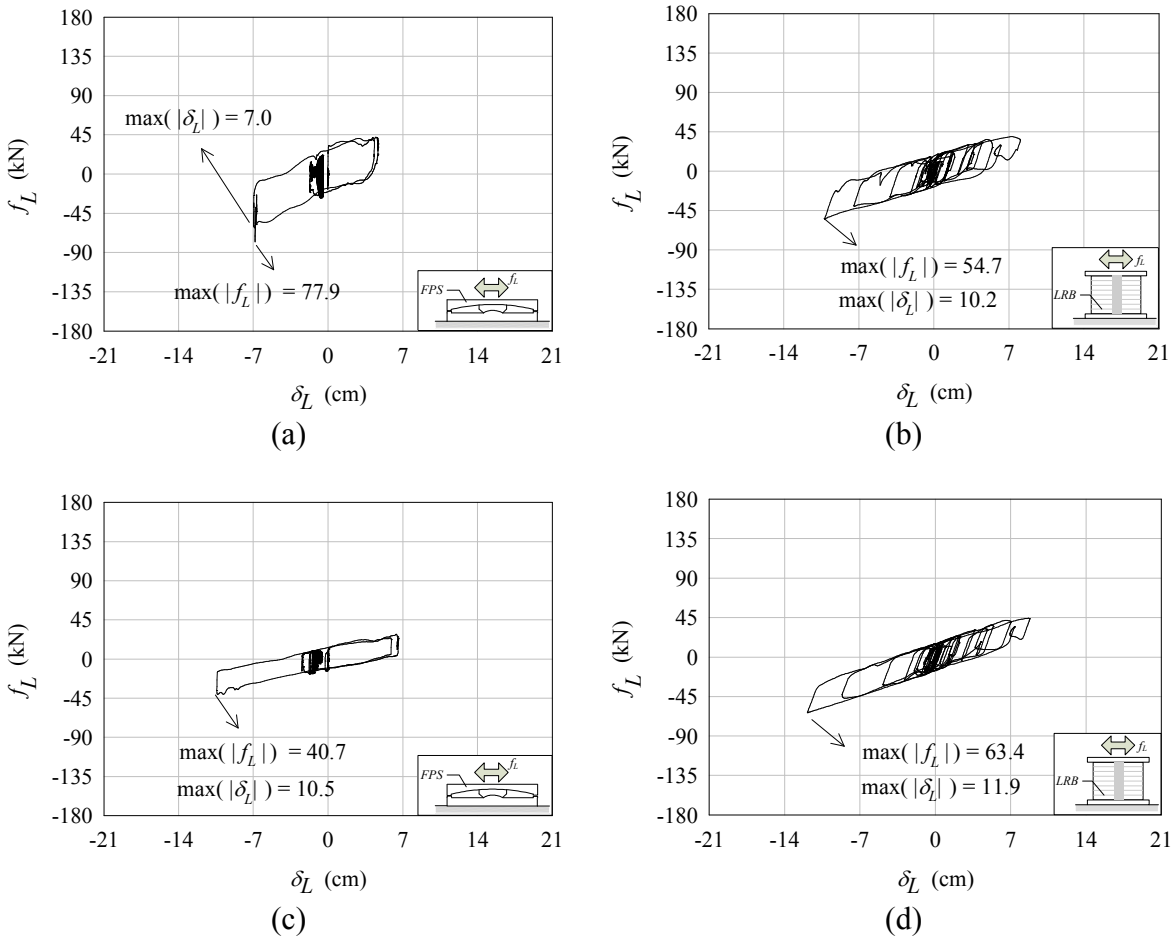

Figure 6.18 Force-deformation history of the FPS and LRB for the Helena earthquake (a),(b) on top of the pier and (c),(d) on top of the abutment.

Figure 6.19 shows the box plots for the ratio of the total MIF transferred to the pier, ΣMIF_{pier}, and the total MIF transferred to the abutment, $\Sigma MIF_{abutment}$; and MND on top of the pier, MND_{pier}, and abutments, $MND_{abutment}$ for the 9 earthquake NLTH analyses (the Northridge earthquake excluded from the initial 10 due to LRB buckling condition). The FPS inflicted more than twice the amount of force to the piers than the abutments on the median. A notable difference with the LRB is that the difference in the isolator forces transmitted to the abutments compared to the piers were closer in magnitude compared to

the FPS. Contrary to the FPS, the LRB transmitted larger forces to the abutments compared to the piers. The MID for both isolator types were larger on top of the abutments compared to the piers. This is attributed to the torsional motion of the bridge-deck. However, this effect was observed to a lesser extent with the LRB-isolated bridge because the stiffness distribution of the isolators along the longitudinal axis of the bridge was more uniform compared to the FPS-isolated bridge.

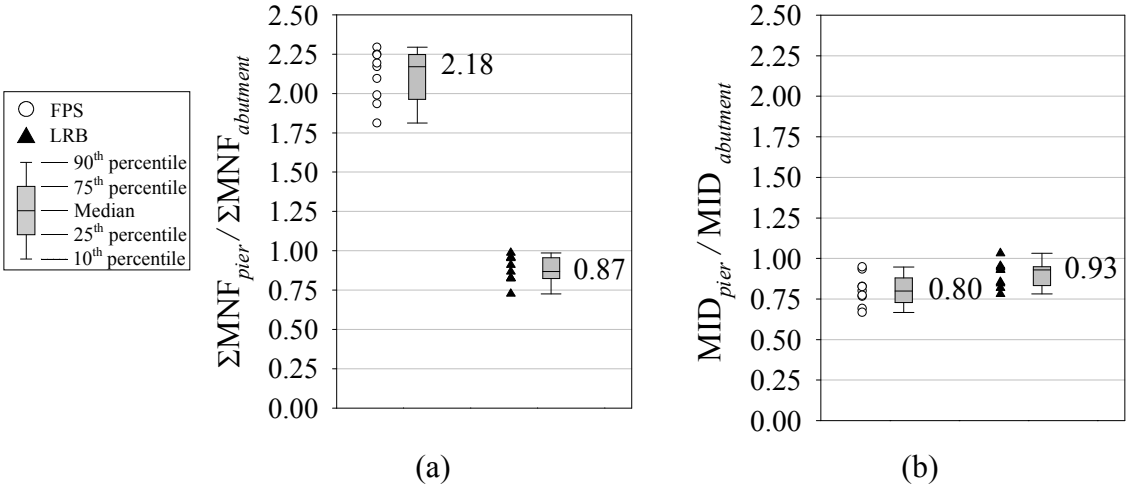

Figure 6.19 Comparison of the (a) total MNF transferred to the pier, ΣMNF_{pier}, and the total MNF transferred to the abutment, $\Sigma MNF_{abutment}$; (b) MID on top of the pier, MID_{pier}, and abutments, $MID_{abutments}$.

Figure 6.20 gives the total energy dissipated by FPS and LRB located on the same beam line but on top of the pier and the abutment for the 9 earthquake time-history analyses. It is observed that the median energy dissipation of the FPS at the abutment is approximately 55% of that at the abutment. The energy dissipation capacities of the LRB on top of the pier and the abutment are closer compared to the case in the FPS.

Furthermore, unlike the case in the FPS, the energy dissipation in the LRB is higher at the abutment compared to the pier.

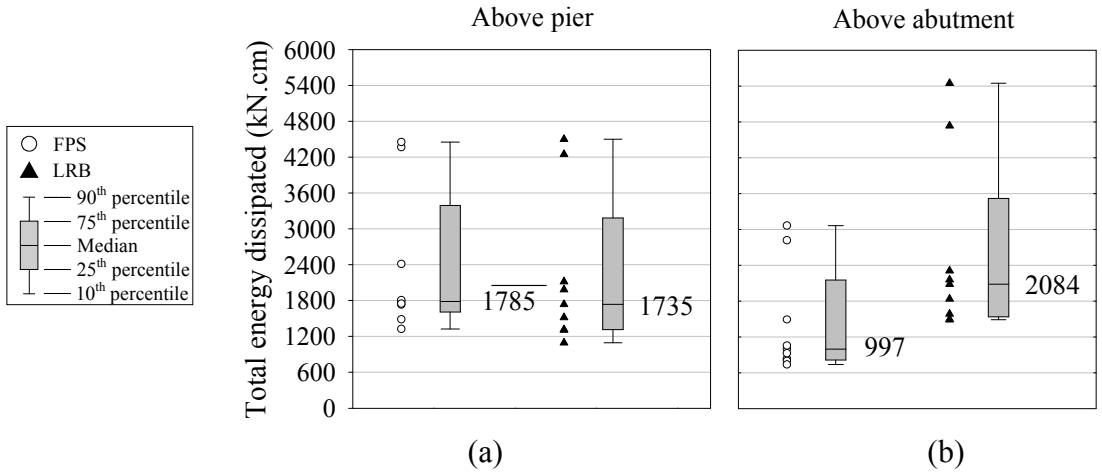

Figure 6.20 Total energy dissipated for by the isolators (a) on top of the pier (b) on top of the abutment.

The MIF and MID acquired on top of the pier for the 9 earthquake time-history analyses are given in Figures 6.21 and 6.22, respectively. The maximum column drifts, d_{max}, are given in Figure 6.23. The statistical interpretation of the results are presented with numerical values of the median and plots of the 10^{th}, 25^{th}, 10^{th}, 75^{th}, and 90^{th} percentile cumulative probabilities. A general comparative assessment from the median values in Figures 6.21 to 6.22 shows that the FPS acquired smaller MID and larger MIF, and placed larger demands on the columns compared to the LRB. It is observed from Figure 19 that the median MIF in the FPS are approximately 46% larger than the LRB. This difference reaches a peak of 139% for the Whittier Narrows earthquake where the MIF in the FPS and LRB were 116 kN and 50 kN, respectively. The MIF of the FPS for

the suite of ground motions is more scattered then the LRB. Exclusion of the $\ddot{u}(t)_v$ in the time-history analyses resulted in the underestimation of the median of the MIF in the two systems by approximately 15%. The median of the MID of the LRB was approximately 32% larger than the FPS. In particular, the difference between the FPS and LRB was maximum for the Nahanni earthquake with 8.2 cm and 4.6 cm. It is observed that the absence of $\ddot{u}(t)_v$ in MID prediction resulted in negligible difference in the FPS and slight overestimation in the LRB on the median. The median of the d_{max} in the FPS-isolated bridge is approximately 17% larger than the LRB-isolated bridge. However, similar to the results obtained for the MIF, the scatter for the FPS-isolated bridge d_{max} is higher. For example the d_{max}=0.78% in the FPS-isolated bridge for the Whittier Narrows earthquake is approximately 82% higher than the LRB-isolated bridge. The median of the d_{max} for the suite of ground motions did not change significantly by excluding the $\ddot{u}(t)_v$ for either isolator.

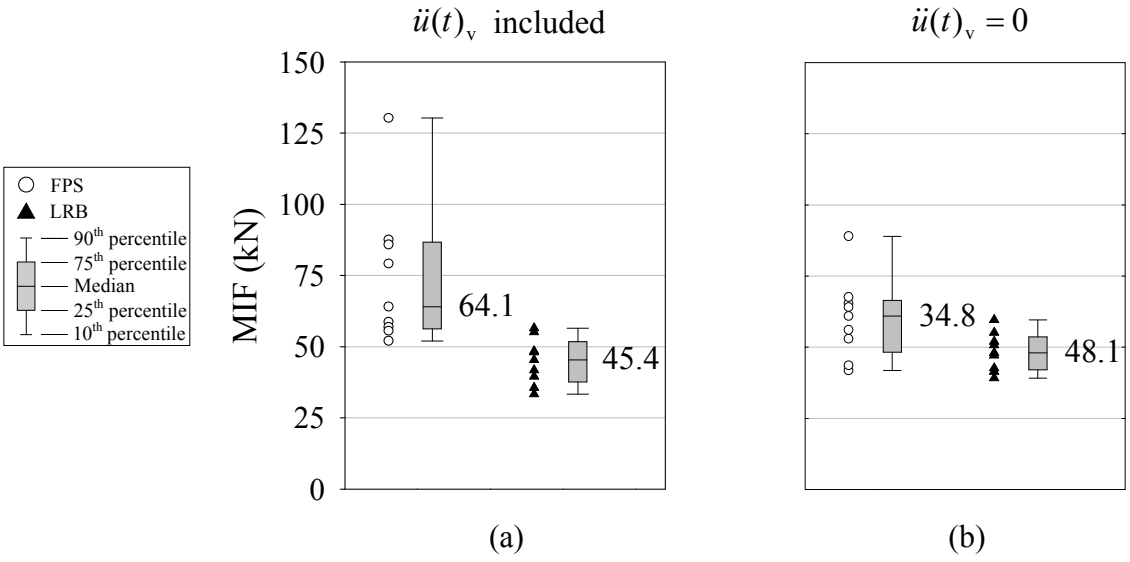

Figure 6.21 Maximum isolator forces (MIF) for the suite of ground motions on top of the pier with vertical component, $\ddot{u}(t)_v$, effect is (a) included (b) not included.

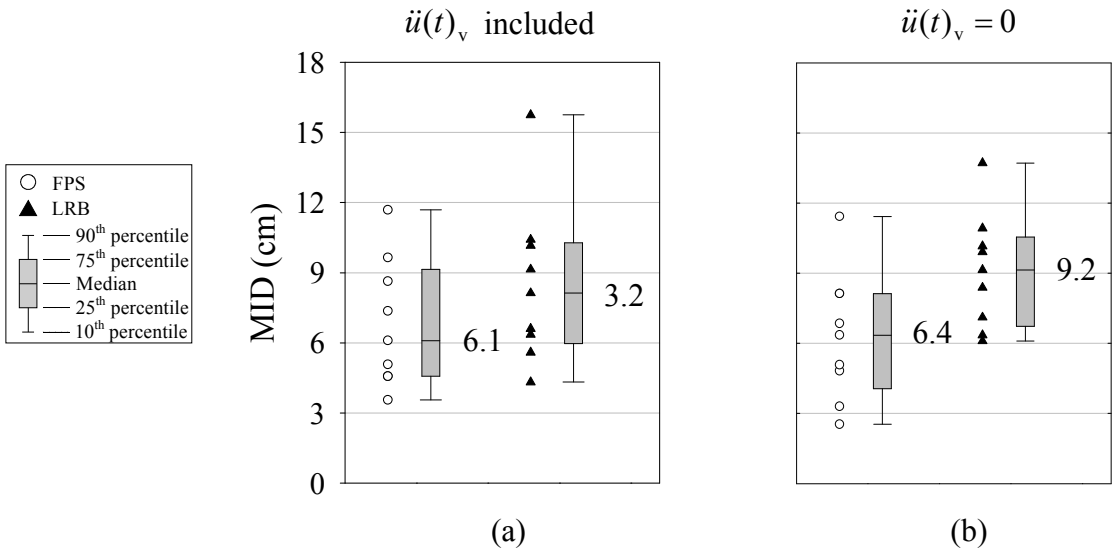

Figure 6.22 Maximum isolator deformations (MID) for the suite of ground motions on top of the pier with vertical component, $\ddot{u}(t)_v$, effect is (a) included (b) not included.

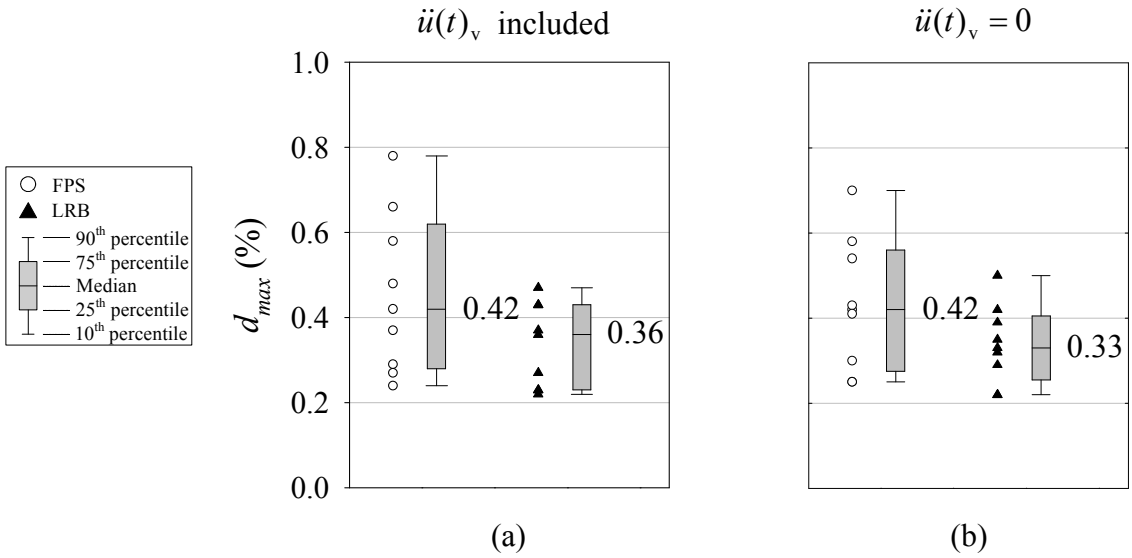

Figure 6.23 Maximum column drifts, d_{max}, for the suite of ground motions on top of the pier with vertical component, $\ddot{u}(t)_v$, effect is (a) included (b) not included.

Figure 6.24 gives the deformation histories of the FPS and LRB on top of the pier for the Morgan Hill earthquake. The displacement trajectories in Figure 6.24(a) and (b) reveal the fundamentally different responses of the two types of isolators. The LRB acquired a larger MID compared to the FPS. The total sum of the deformation of the LRB and the FPS are 29.1 cm and 47.9 cm, respectively. This can be explained further by Figure 6.24(c)-(d). The LRB deformation history has a higher frequency content compared to the FPS. Consequently, the LRB engages into motion at smaller dynamic vibrations compared to the FPS. This is attributed to lower elastic stiffness of the LRB compared to the FPS. It is concluded that the LRB is more sensitive to the frequency content of the ground motion compared to the FPS.

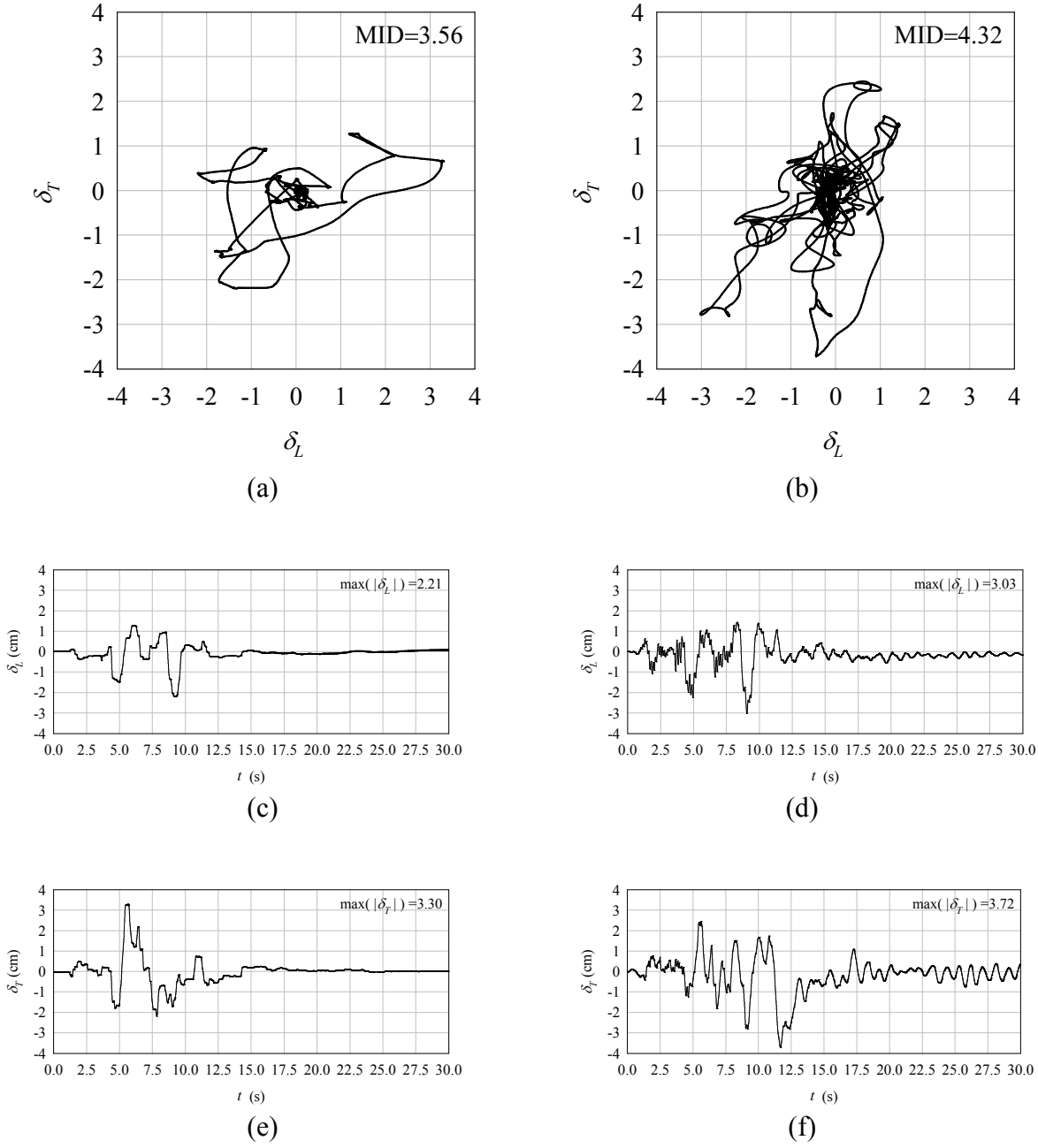

Figure 6.24 Deformation histories for the Morgan Hill earthquake of (a), (c), (e) FPS and (b), (d), (f) LRB located on top of the pier.

6.9 Conclusion

In this paper, the distinctions of the response characteristics of sample elastomeric and sliding isolator types, the Lead Rubber Bearing (LRB) and the Friction Pendulum System (FPS) respectively, have been highlighted. An LRB model to account for both the coupling in the in-plane and vertical directions has been developed. Two models of a three-dimensional (3-D) Multi-Span Continuous Concrete Girder (MSCCG) bridge, one isolated with the FPS and the other with the LRB, was generated. Nonlinear time-history analyses using a suite of 10 ground motions that corresponded to a hazard level of 7% in 75 years was performed for the two bridges. Following conclusions are made:

(1) Despite attaining similar seismic isolation periods, the choice between the LRB or the FPS resulted in considerable differences in the response of the bridge and the isolator forces and displacements.

(2) Excluding the vertical component of the ground motion in the analyses dampened the distinctions that exist between the force-deformation response of the FPS and the LRB. The median maximum isolator forces and displacement values were underestimated for both types of isolators in the absence of vertical components of the ground motions in the analyses. However, the effects of the vertical components of the ground motion on the isolator response had negligible effect on maximum column drifts.

(3) The LRB acquired higher displacements, however, placed smaller demands on the columns compared to the FPS.

(4) The LRB had a more uniform distribution of lateral stiffness throughout the bridge compared to the FPS. The FPS stiffened on top of the piers while the LRB was stiffer on top of the abutments. These distinctions arise from the variant dependency of the two isolators to normal loads.

(5) The FPS is capable of accommodating vertical components of the ground motion records that might result in a buckling failure of the LRB. Excluding the vertical component of the ground motion in the modeling and analysis phases of the LRB may result in overlooking a fundamental failure mode.

CHAPTER 7

ASSESSMENT OF THE INFLUENCE OF DESIGN PARAMETERS ON THE RESPONSE OF BRIDGES SEISMICALLY ISOLATED WITH FRICTION PENDULUM SYSTEM (FPS)

7.1 Introduction

Seismic isolation is applicable to a wide range of bridges that differ in geometric and material properties. Additionally, the design characteristics of the FPS may be modified to alter the seismic response of the bridge. A further understanding of the effects of design parameters will provide insight on both the level of complexity required in modeling and the seismic response for a wider range of bridge designs. This chapter investigates the effects of bridge design parameters and an innovative isolation design strategy on bridge seismic response. In the first section, the "single-factor" method and regression analyses are performed with nonlinear-time history (NLTH) analyses to quantify the significance of bridge design parameters on the system's response quantities. In the second section, a new seismic isolation strategy that involves a practical design modification to the FPS at the abutments is presented. This approach aims to improve the seismic response of the bridge by creating a more uniform response between the isolators located at the piers and the abutments. The implications of possible design variations in this new seismic isolation strategy are illustrated.

7.2 Influence of Bridge Design Parameters

To ascertain the effects of the design parameters of the typical highway bridges on the system's seismic response, an experimental design is constructed. The term "experimental design" can be defined as: "*the experimental structure used to generate*

practical data for interpretative purposes" (Gardiner and Gettinby 1998). The "single-factor design", which is a form of experimental design to analyze the influence of different levels of a controllable parameter on a measured response, is selected for this study (Gardiner and Gettinby 1998).

7.2.1 Analyses

The three-dimensional bridge model with FPS isolation developed in Chapter 6 is used as the base model to which the variation of the design parameters is compared. The details of this model are not repeated in this chapter. The design parameters of the base model are denoted by a subscript 'o'. The NLTH analyses are performed using the suite of ground motions described in Chapter 6 for four equally spaced values of selected bridge design parameters. These parameters are detailed in Table 7.1 and illustrated in Figure 7.1. The upper and lower bounds of the selected design parameters in Table 7.1 are selected from the bridge inventory analysis performed by Nielson (2005) for the Central and Southeastern United States. Reinforcement ratio and distribution is assumed to remain the same for the range of column height, L_c, considered. The span length is varied in two different ways: (1) mass adjusted to increasing length, L_d*, (2) mass kept constant at all lengths, L_d. Increasing the span length by keeping the mass and cross-section properties constant provides the opportunity to monitor the effects of superstructure flexibility. Given the wide range of material properties available, superstructure sections with the same structural characteristics may be constructed for constant mass. Adjusting the mass for the same cross-section in the superstructure provides insight on the influence of additional dead weight. The influence of pinned and fixed modeling assumptions for the base is illustrated to provide the bounds of the response (Figure 7.2). However, the results from this analysis are handled separately since this variation is associated with modeling assumptions as opposed to a design parameter in a bridge.

Table 7.1 Parameter variation ranges

Parameter	Abbreviation	Range
Degree of skew	α	0-40 (degrees)
Column height	L_c	3.6-7.5 (m)
Span length	L_d	20-60 (m)
Span length*	L_d*	20-60 (m)
Concrete nominal strength	f_c	20.7-48.3 (MPa)
Base conditions	-	Pinned, elastic, fixed

*Mass adjusted in accordance with increased length

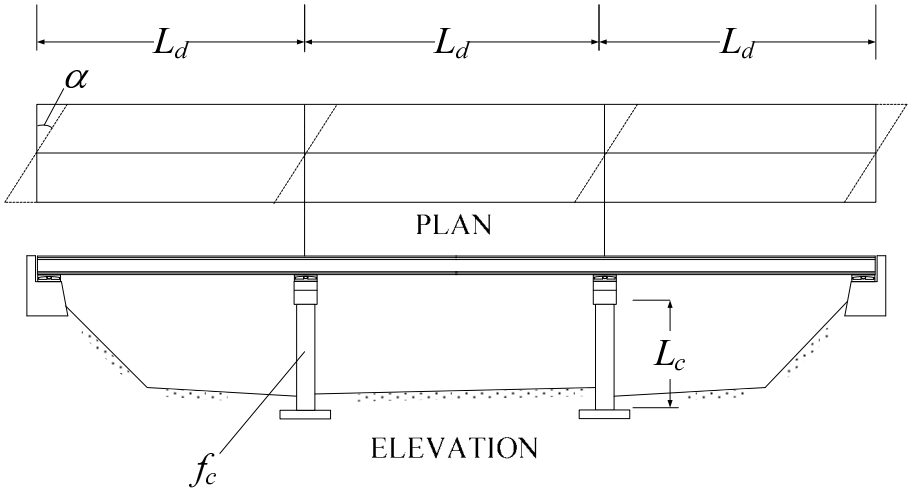

Figure 7.1 Bridge design parameters.

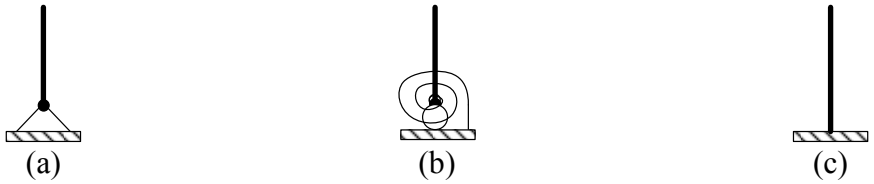

Figure 7.2 Base conditions for the substructure modeled as (a) pinned (b) partially-fixed (c) fixed.

Performance of the bridge is monitored via the maximum normalized force and displacement of the FPS isolators located on top of the pier, MNF and MND, maximum column drifts, d_{max}, the ratio of the total MNF transferred to the pier and the total MNF transferred to the abutment, ΣMNF_{pier} / $\Sigma MNF_{abutment}$, the ratio of the MND on top of the abutment and MND on top of the pier, MND_{pier} / $MND_{abutment}$. The variation of these response quantities is plotted against the selected design parameters for the ten ground motion records used in Chapter 6. Linear regression curves in the form: $y(x) = ax + b$, for the median values of the response quantities are developed. The slope of these regression curves, $a_{'response\ quantity'}$, is used to quantify the significance of the design parameters.

7.2.2 Results

Linear regression curves for the bridge response quantities as a function of the variation of the design parameters are given in Appendix B. Figure 7.3 summarizes the absolute values of the slope, $a_{'response\ quantity'}$ of the regression curves in Appendix B. The exact values of the slopes are denoted on top of the bars with the corresponding signs. Positive and negative signs indicate an increase and decrease of the linear regression curves as the design parameter magnitude increases, respectively. It is observed from Figure 7.3 that the two design parameters that have made the highest impact on the response quantities were L_c and L_d^*. The variation of these two parameters caused the largest shift in the fundamental vibration period of the structure (Table 7.7). The first three vibration periods for the base model were T_1=2.38 s, T_2=2.26 s, and T_3=2.00 s (see Figure 6.10). Although the shape of the first three modes of vibration remained the same with the base model, a notable change in the first period, T_1, was observed in the bridge as a function of L_c and L_d^*.

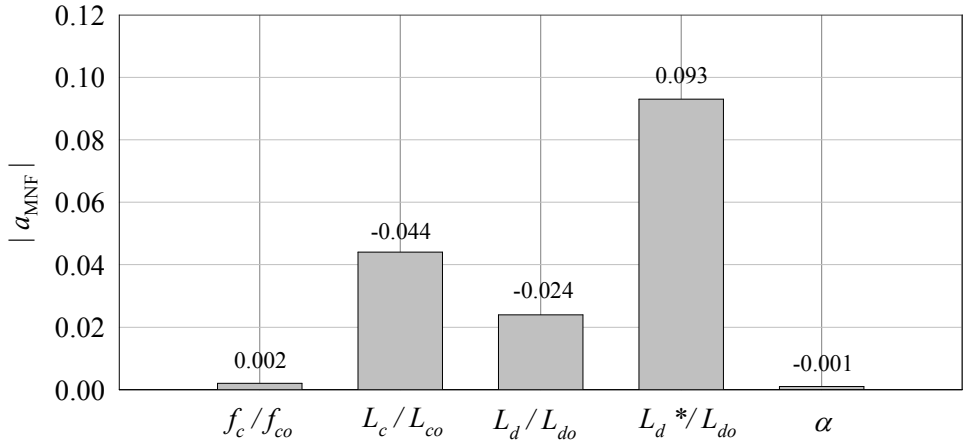
0.12
0.10
0.08
0.06
0.04
0.02
0.00
$|a_{MNF}|$
0.002
-0.044
-0.024
0.093
-0.001
f_c/f_{co}
L_c/L_{co}
L_d/L_{do}
L_d*/L_{do}
α

(a)

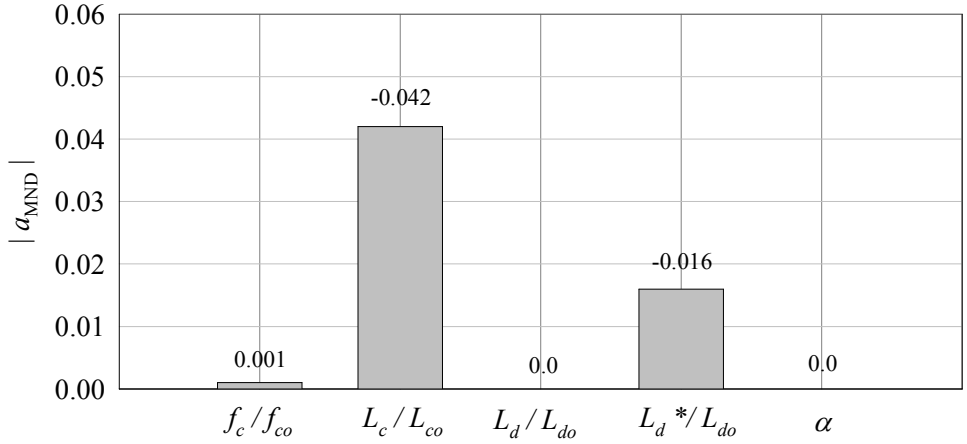
0.06
0.05
0.04
0.03
0.02
0.01
0.00
$|a_{MND}|$
0.001
-0.042
0.0
-0.016
0.0
f_c/f_{co}
L_c/L_{co}
L_d/L_{do}
L_d*/L_{do}
α

(b)

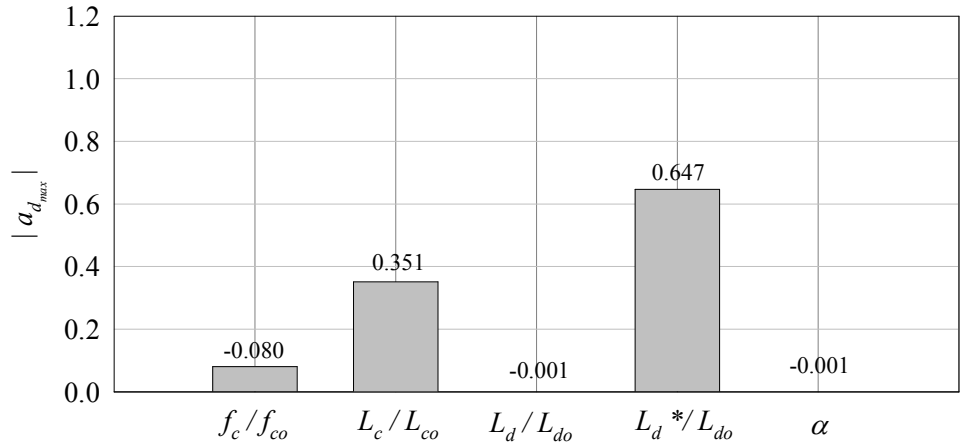
1.2
1.0
0.8
0.6
0.4
0.2
0.0
$|a_{d_{max}}|$
-0.080
0.351
-0.001
0.647
-0.001
f_c/f_{co}
L_c/L_{co}
L_d/L_{do}
L_d*/L_{do}
α

(c)

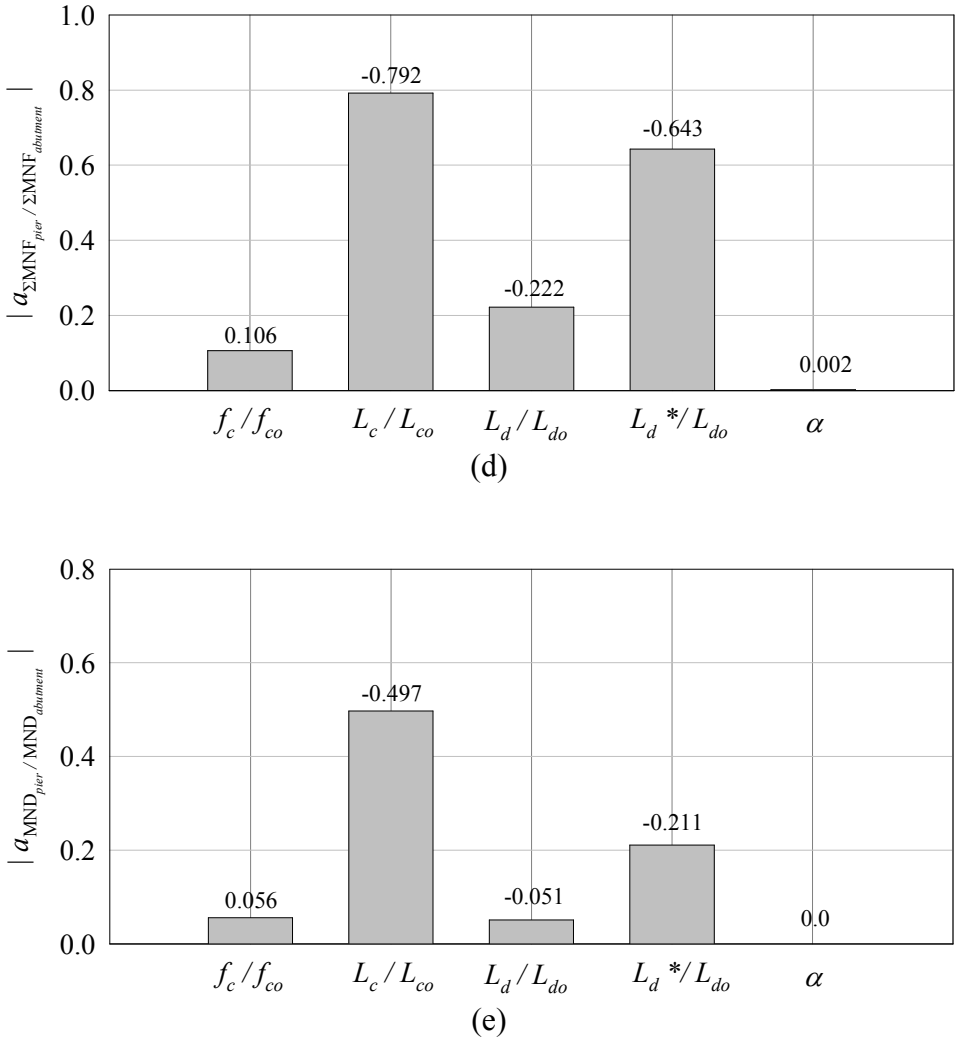

Figure 7.3 Slopes, $a_{,response\ quantity,}$ for the regression lines of the median design parameters.

Table 7.2 Vibration periods of the bridges as a function of design parameters

	L_c/L_{co}				L_d^*/L_{do}			
Period	0.8	1.2	1.4	1.6	0.75	1.25	1.5	1.75
T_1	2.328	2.461	2.551	2.654	2.343	2.427	2.454	2.592
T_2	2.274	2.303	2.32	2.354	2.268	2.296	2.307	2.519
T_3	1.999	1.999	2.008	2.018	1.98	2.008	2.019	2.327

The increase of L_c created a more flexible structure with increased fundamental vibration. Consequently, the bridge and attracted lower seismic forces. Figure 7.4 shows the longitudinal normalized force-deformation response of the FPS on top of the pier and the history of the column tip displacements, δ_{column}, for the Whittier Narrows earthquake record for the cases of stiff (L_c/L_{co}=0.8) and flexible (L_c/L_{co}=1.6) substructure. It is observed that the increased flexibility of the columns resulted in higher structural displacements of the substructure at the isolator level and dampened the effect of seismic isolation. Larger L_c/L_{co} resulted in flexible supports for the isolators located on top of the piers. However, the fixity of the supports for the FPS located on top of the abutments remained the same. Consequently, the terms indicating the difference in the responses between isolators at the piers and abutment, MND_{pier} / $MND_{abutment}$ and ΣMNF_{pier} / $\Sigma MNF_{abutment}$ increased considerably as the substructure flexibility increased. The magnitude of d_{max} increased with larger substructure flexibility.

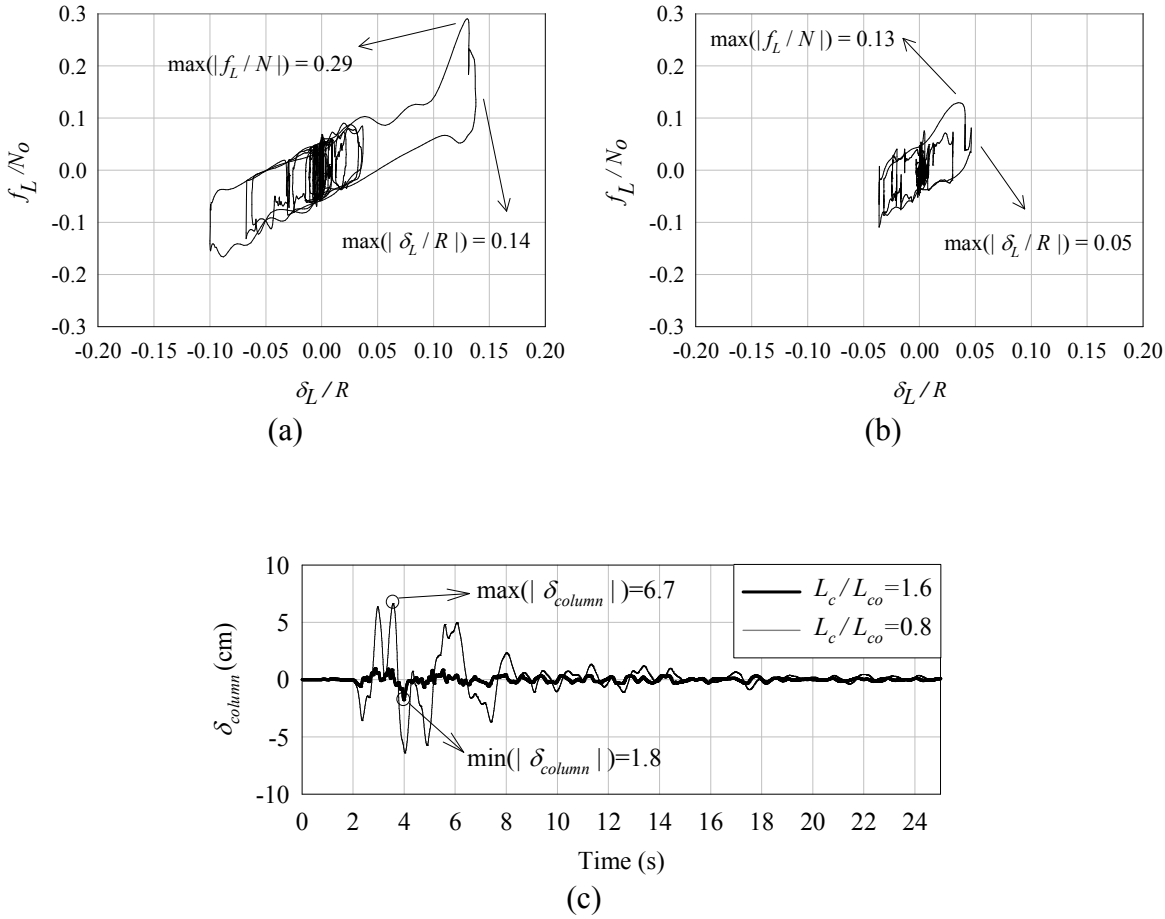

Figure 7.4 Force-deformation history of the FPS in the longitudinal direction on top of the pier for the Whittier Narrows earthquake record with (a) L_c/L_{co}=0.8 (b) L_c/L_{co}=1.6; (c) time-history of the longitudinal column tip deformations.

The influence of increased mass simulated via adjusted span length, L_d*, is unique. Although the larger gravity load has stiffened the response of the isolators and resulted in larger MNF, it has also increased the fundamental period of the structure. Figure 7.5 shows the longitudinal normalized force-deformation of the FPS on top of the pier for the Whittier Narrows earthquake record for the cases of L_d^*/L_{do}=0.75 and L_d^*/L_{do} =1.75). It is observed that larger N increased the stiffness and post-yield values of the

FPS and caused the isolators to deform less. Larger MNF was acquired with increased superstructure mass and this resulted in higher structural demands in the columns observed from increased values of d_{max}.

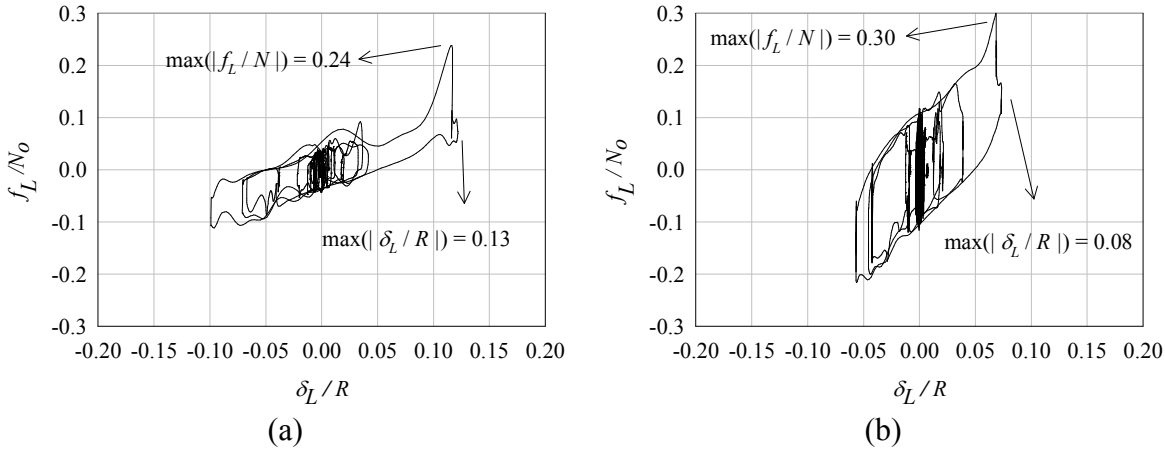

Figure 7.5 Force-deformation history of the FPS in the longitudinal direction on top of the pier for the Helena earthquake record with (a) L_d^*/L_{do}=0.75 (b) L_d^*/L_{do} =1.75.

Increased flexibility of the superstructure had negligible effect on d_{max} and MND. However, the MNF, MND_{pier} / $MND_{abutment}$, and ΣMNF_{pier} / $\Sigma MNF_{abutment}$ were moderately affected. Figure 7.6 shows the longitudinal normalized force-deformation and the N history normalized with the initial gravity load, N_o, of the FPS on top of the pier for the Northridge earthquake record for the cases of stiff (L_d/L_{do}=0.75) and flexible (L_d/L_{do} =1.75) superstructure. It is observed that the stiff superstructure caused considerably larger MND and MNF and resulted in the uplift of the isolator when compared to the flexible superstructure. This is attributed to the reduced vertical flexibility gained by larger L_d. As L_d increases the vertical flexibility of the structure increases and dampens the vertical effects of the ground motions. Consequently, it is

observed that the max(N/N_o) for the flexible superstructure is approximately 60% of the stiff superstructure. This stiffening affect increases MNF and d_{max}. This indicates that the vertical components of the ground motion are less influential for bridges with large superstructure flexibility.

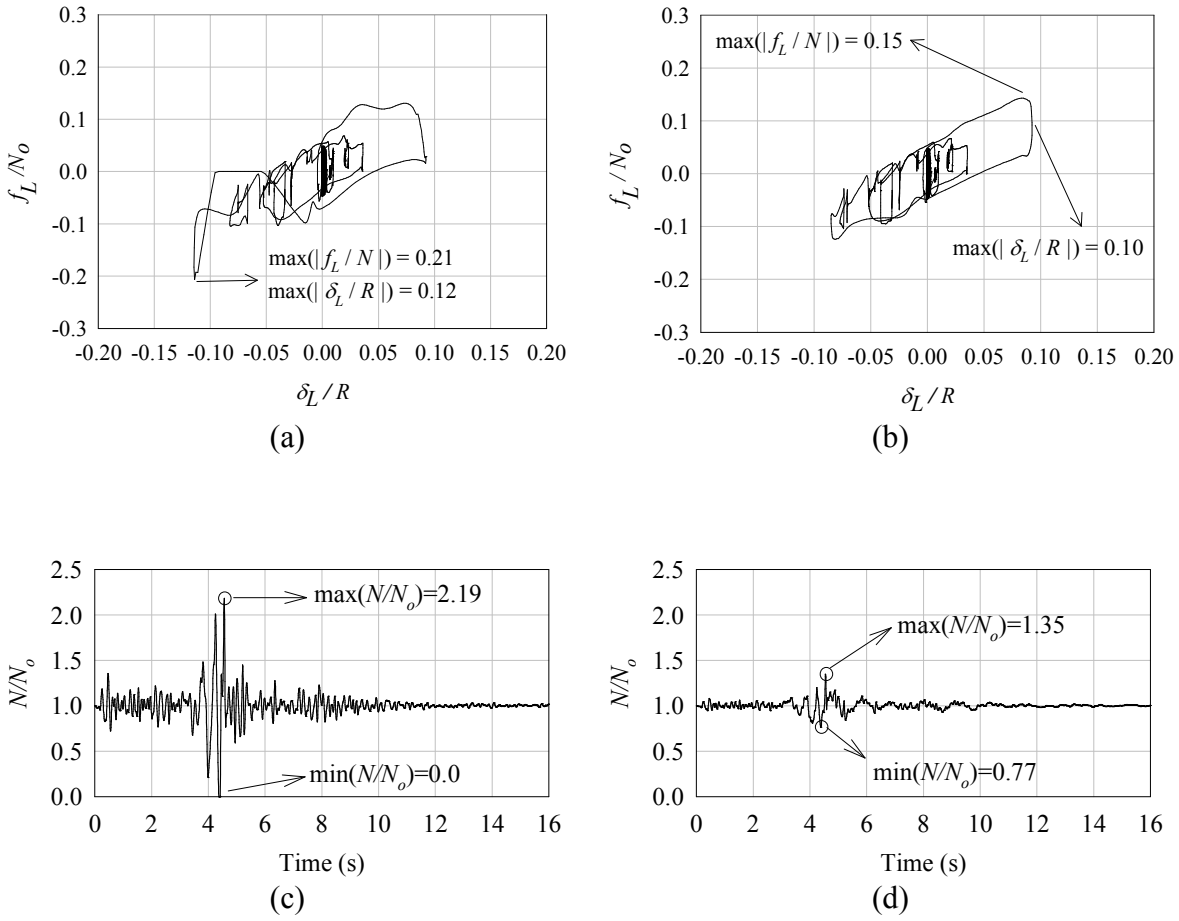

Figure 7.6 Force-deformation history of the FPS in the longitudinal direction on top of the pier for the Northridge earthquake record with (a) L_d/L_{do}=0.75 (b) L_d/L_{do} =1.75.

Bridge skew, α, had negligible effect on the response quantities of the bridge. This is attributed to the concentration of the seismic response at the isolators and the uncoupling of the superstructure from the substructure. Similarly, the influence of f_c on the structural response quantities was negligible.

The influence of pinned, partially-fixed, and fixed base modeling assumptions on the bridge response quantities is given in Figure 7.7. The first three vibration periods of the fixed-base and pinned-base were T_1=2.31 s, T_2=2.26 s, T_3=2.00 s and T_1=4.80 s, T_2=2.31 s, T_3=2.01 s, respectively. It is observed that the pinned-base modeling assumption results in substantial overestimation of the T_1 and a general underestimation of the response quantities compared to partially-fixed and fixed base modeling assumptions. The base bridge model response quantities are in general closer to the fixed-base modeling assumption.

In the pinned-base model, the effect of the isolators at the piers was reduced because the substructure flexibility allowed for accommodation of more of the seismic deflections compared to the fixed-base condition. Figure 7.8 illustrates this aspect using approximate deflected shapes of the bridge where the bases are modeled as either pinned or fixed. The isolators located on top of the piers in the pinned-base model attained negligible deformations due to the deformability of the substructure. Seismic deformations of the substructure were essentially resisted by the isolators on top of the abutments. This is a similar phenomenon to that observed with the increased values of L_c. Figure 7.9 shows the longitudinal and transverse normalized force-deformation history of the FPS on top of the pier for the Loma Prieta earthquake record for the pinned and fixed base conditions of the bridge model. It is observed that in the pinned base model, the longitudinal response of the isolators located on top of the piers become negligible in the longitudinal direction. The transverse action of the isolators is due to the frame rigidity of the piers in these directions. It is concluded that the pinned modeling assumption may result in considerable underestimation of isolator design parameters and

reduce the effectiveness of seismic isolation. Increased substructure flexibility contributes to the difference in the response of the isolators located at the piers and the abutments.

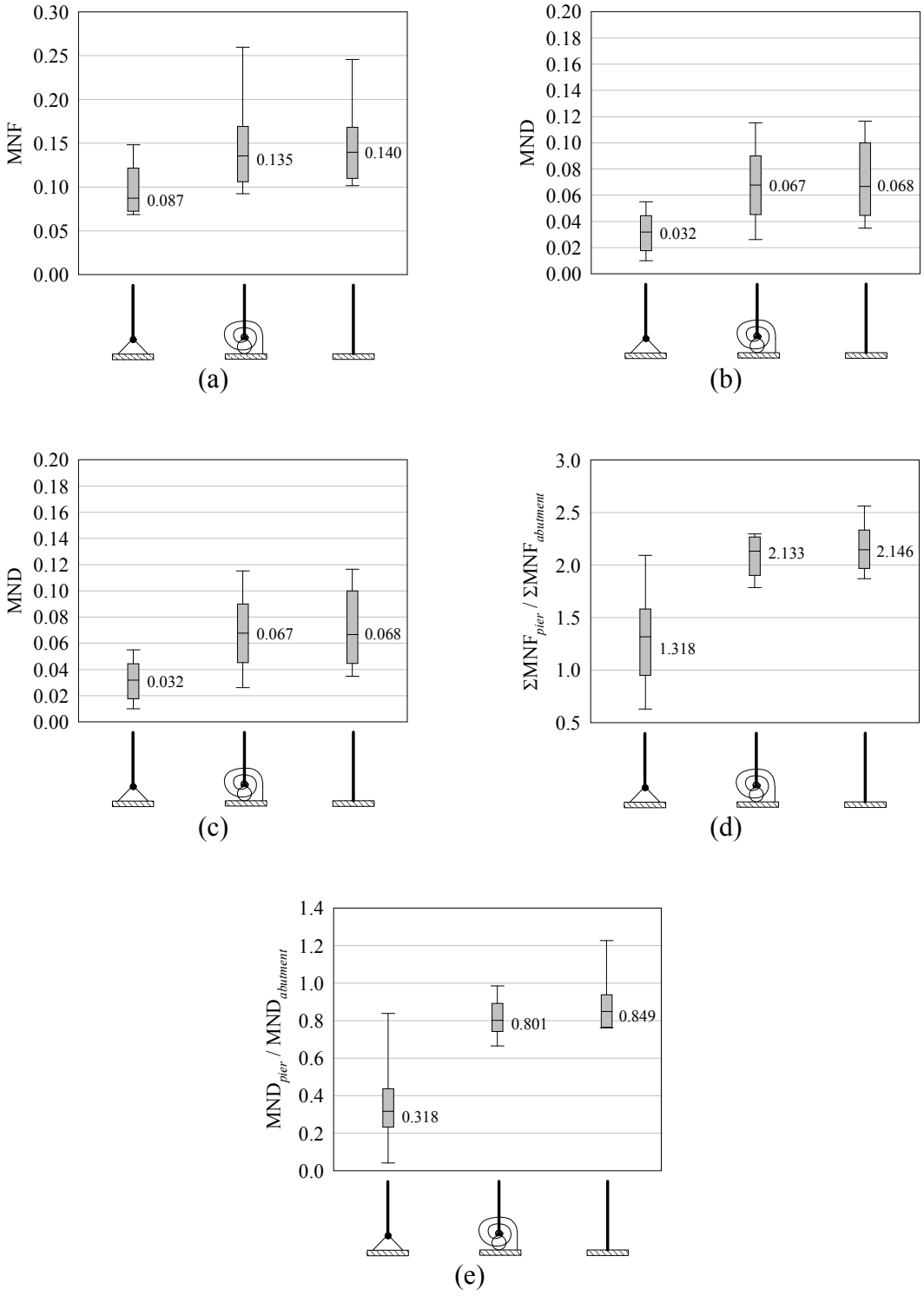

Figure 7.7 Median values of the response quantities of the bridge as a function of base modeling assumptions.

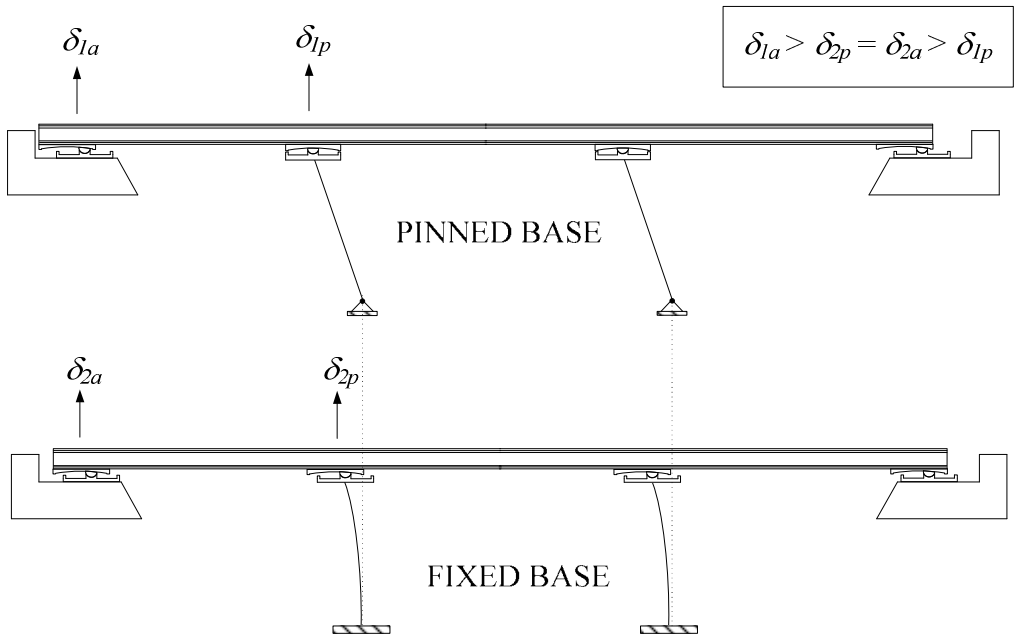

Figure 7.8 Structural bridge responses as a function of base modeling assumptions.

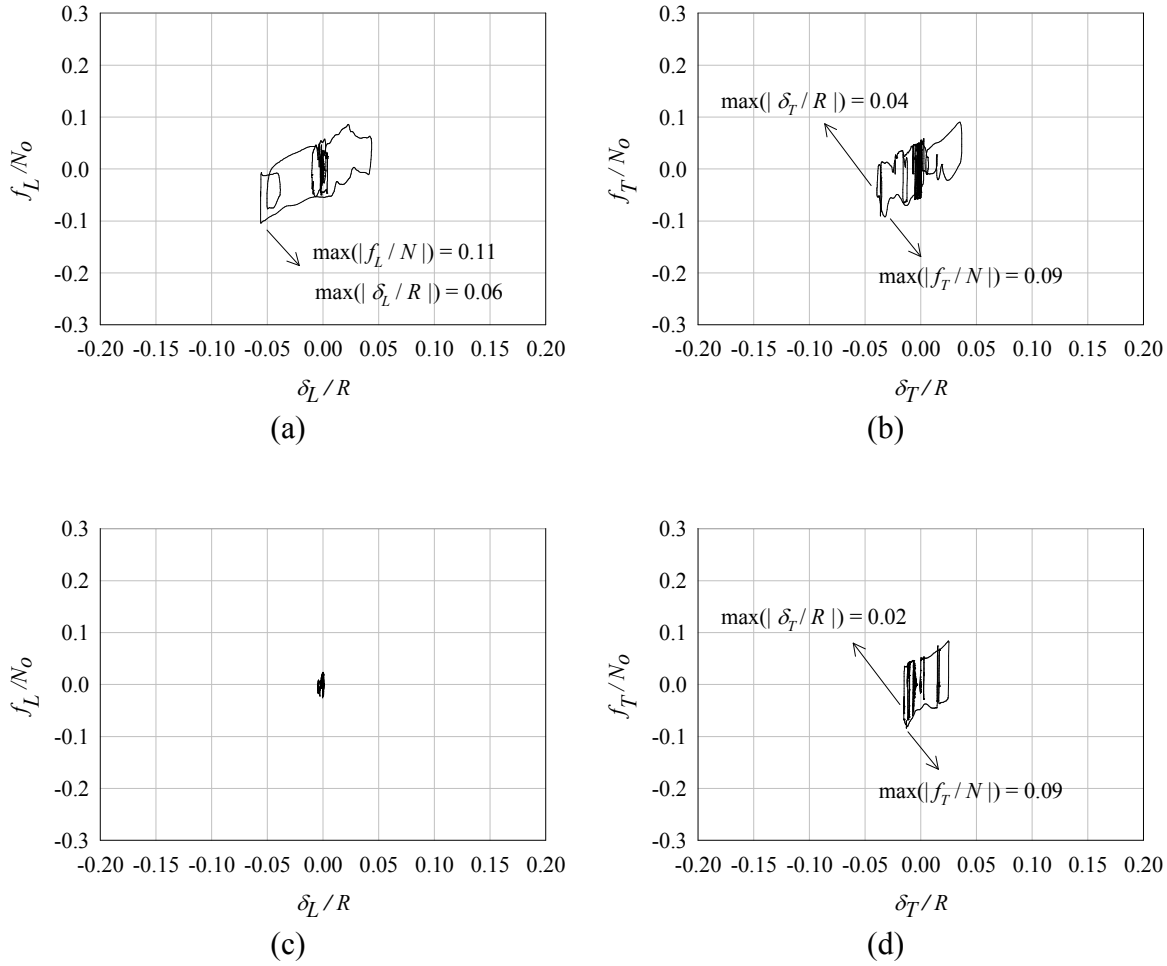

Figure 7.9 Force-deformation history of the FPS in the longitudinal and transverse directions on top of the pier for the Loma Prieta earthquake record with (a), (b) fixed base conditions; (c), (d) pinned base conditions.

7.3 Influence of a Modified Seismic Isolation Strategy

The FPS design parameters that can be investigated for a range of values are limited. A notable disadvantage of the FPS is that it is essentially a one-parameter system based on the radius of its concave dish, R (Naeim and Kelly 1999). It has been shown in Chapters 4 and 5 that achieving constant prescribed friction forces is difficult due substantial changes in the magnitude of the friction coefficient as a function of sliding

velocity and pressure. The smallest R of the FPS in standard manufacture by the Earthquake Protection Systems is 99 cm (Earthquake 2003). Isolators with smaller R have been manufactured, however, for experimental research purposes. Examples include R = 48 cm (Erdik and Uckan 2004), R = 56 cm (Constantinou et al. 1993), and R = 76 cm (Mosqueda et al. 2004). An important implication of smaller R is the reduction of maximum lateral deformation capacity, Δ_{max}, of the isolator. Standard radii in manufacture for the FPS are 99, 155, 224, 305, 396, and 620 cm. It has been shown in Chapters 5 and 6 that the vibration characteristics of bridges are essentially a function of the isolator properties. Hence, using larger R for the FPS without additional measures may shift the fundamental period of the structure to a region out of interest in the design spectra.

It has been shown in Chapters 5 and 6 that there exists a notable variation in the stiffness and yield force properties of the FPS isolators located above the piers and abutments. Specifically, the isolators at the abutments acquired smaller yield force and post-yield stiffness compared to those located at the piers. This lead to torsional modes of vibration of the superstructure during earthquake induced loads. Additionally, larger displacement demands and lower transfer of seismic forces were observed at the isolators located at the abutments compared to those located at the piers. A more favorable response may be obtained by acquiring stiffer FPS force-deformation response at the structurally stronger abutments compared to the piers.

One option to increase the stiffness and yield force of the FPS located above the abutments is to increase the magnitude of the normal force, N. Kasalanati and Constantinou (2005) showed that the FPS isolators can be effectively prestressed to achieve higher N. However, the primary objective of this approach is the prevention of tensile force and uplift of the isolators. Additionally, tendons must be configured to sustain a limited amount of tensile strain as shown in Figure 7.10. This setup may not be practical for the configuration of the isolators located at the abutments

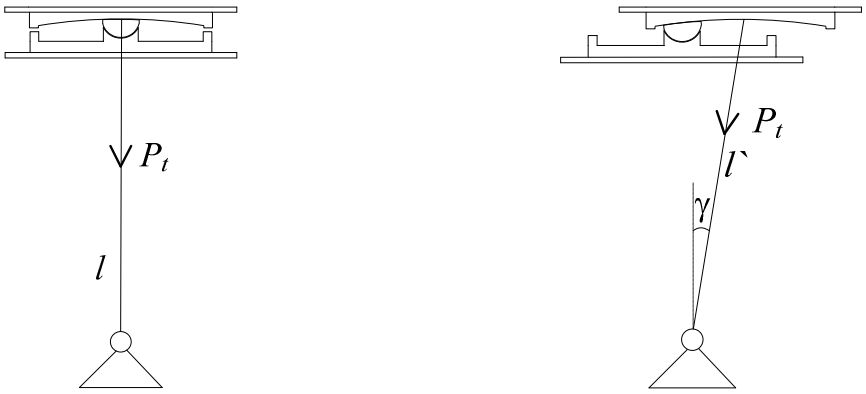

(a) (b)

Figure 7.10 Prestressing the FPS (Kasalanati and Constantinou 2005).

7.3.1 Proposed Design

Considering the limitations on the design parameters of the FPS explained above, a modified approach for the seismic isolation of the bridge is proposed. The objective of the design is to:

1) Contribute more to reducing the structural demands on the columns by achieving smaller d_{max}
2) Create a more balanced $\Sigma MNF_{pier} / \Sigma MNF_{abutment}$ and $MND_{pier} / MND_{abutment}$

The primary constraint is to maintain the same R for all the isolators in the bridge to avoid additional mold costs.

The proposed bridge seismic isolation approach consists of increasing the R throughout the isolators in the bridge and introducing a modified design to the isolators at the abutments. The conceptual drawing of the proposed design modification for the FPS located at the abutments is given in Figure 7.11. This simple modification consists of the introduction of extension spring elements around the perimeter of the isolator (Figure 7.12). The objective of this supplemental design approach is to generate a stiffer force-

deformation response for the isolators at the abutments. The springs are pin-connected to the upper and lower steel plates of the isolator and provide supplemental source of stiffness and energy dissipation as the isolator displace (Figure 7.11). Additionally, the vertical position of the springs also provides tensile restraint in the event of uplift. The number of springs may be varied as a function of the required amount of supplemental stiffness and energy dissipation. Extension springs are proposed for the task because of their existing widespread use in a vast variety of industries, capability to undergo deformations that are of interest to isolators, and wide range of design parameters (Carlson 1978; Chironis 1961). Other alternatives, such as rubber springs, may further be explored; however, this is outside the scope of this study (see Göbel and Brichta 1974).

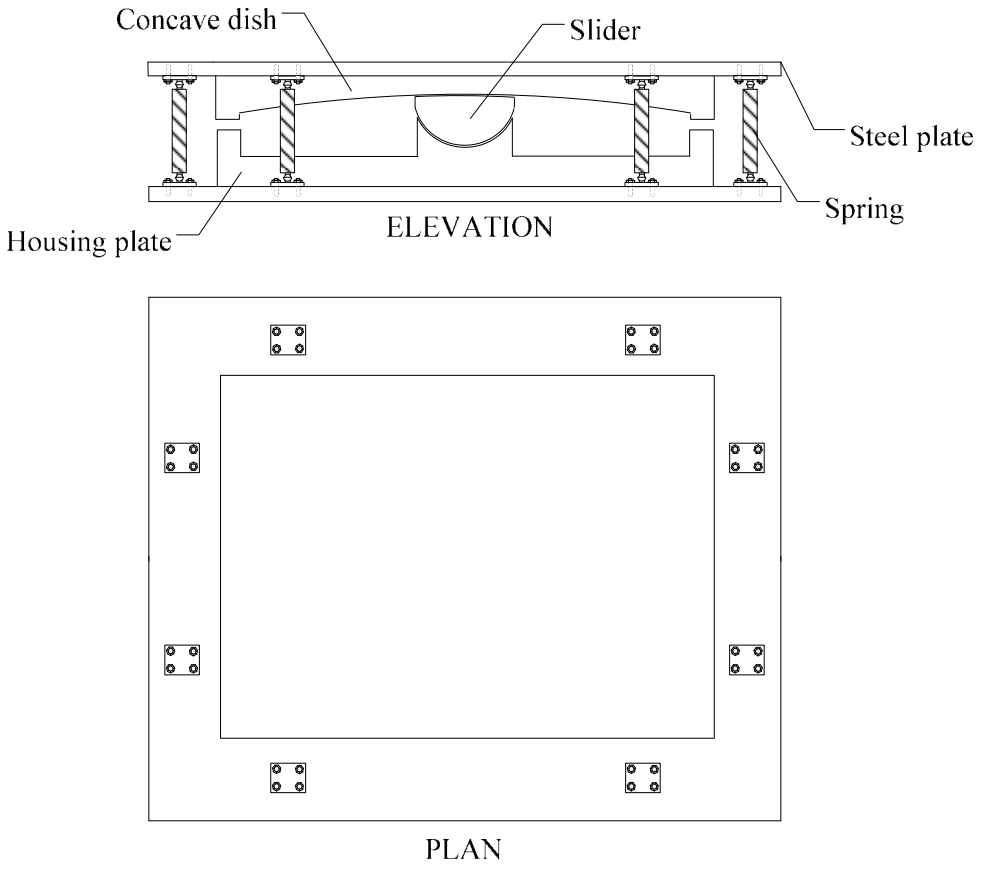

(a)

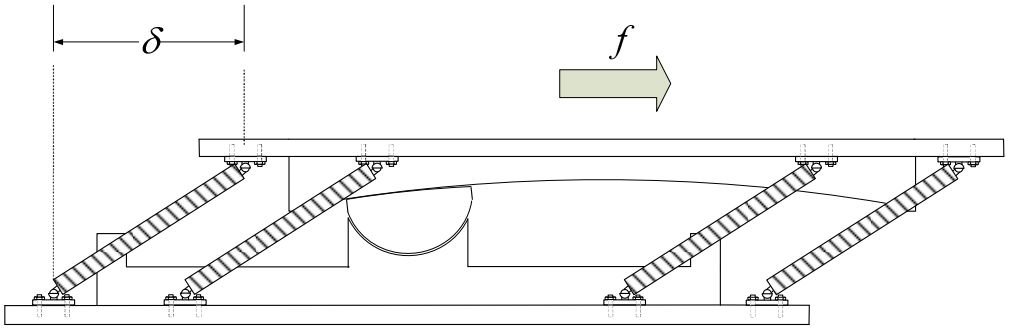

(b)

Figure 7.11 Proposed modified design for the FPS above the abutments in (a) undeformed (b) deformed state.

Figure 7.12 Sample spring element to be used in the proposed modified design of the FPS at the abutments.

The force deformation-response of the springs is assumed to be elastic. Although it is possible to design extension springs for pretensioned loads, this property is neglected. The influence of the supplemental spring in the force-deformation response of the FPS is analyzed for the displacement-controlled load history given in Figure 7.13. It is assumed that a single FPS isolator with the design properties used in the analyzed bridge and N=258 kN, is introduced in the supplemental springs that have a stiffness, k_s=1.286 kN/cm. Figure 7.14 gives the force-deformation response of the FPS, spring and the combined FPS and spring response. It is observed that the addition of the elastic spring increases the post-yield stiffness and the energy dissipation capacity of the isolator.

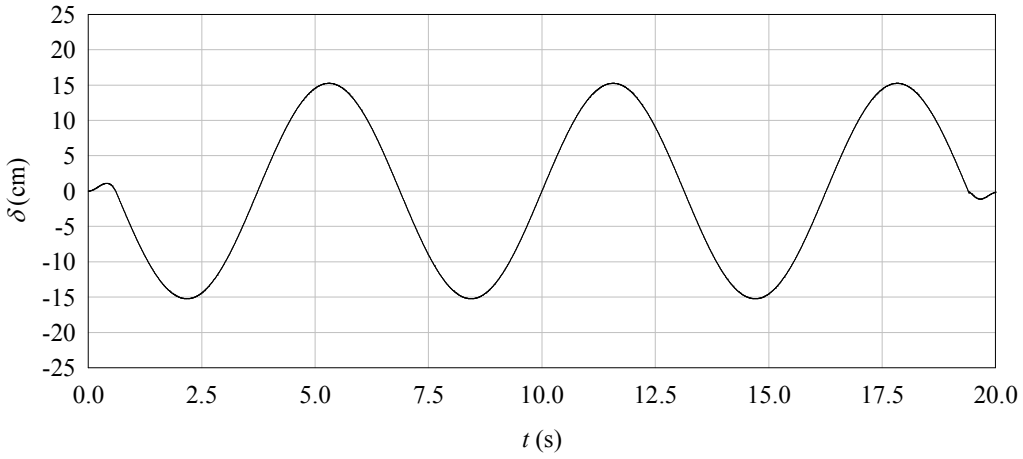

Figure 7.13 Displacement-controlled load history

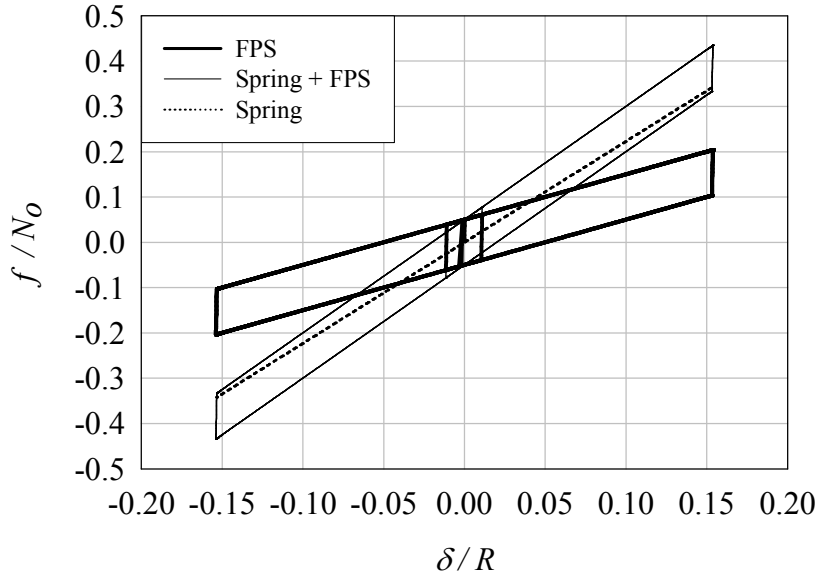

Figure 7.14 Force-deformation response of the isolator with modified design.

Figure 7.15 shows the configuration and the modeling of the modified FPS design in the 3-D bridge model. The supplemental springs are modeled in OpenSees as zero-length elements with elastic uniaxial material object in the x, y and z directions. The response of the springs in the three main directions is uncoupled. This is an additional advantage of the proposed design because it allows for the assignment of separate stiffness characteristics in different directions to give more control over the seismic response over the isolator. The spring element essentially acts in parallel in all three principal directions to the response of the FPS isolator.

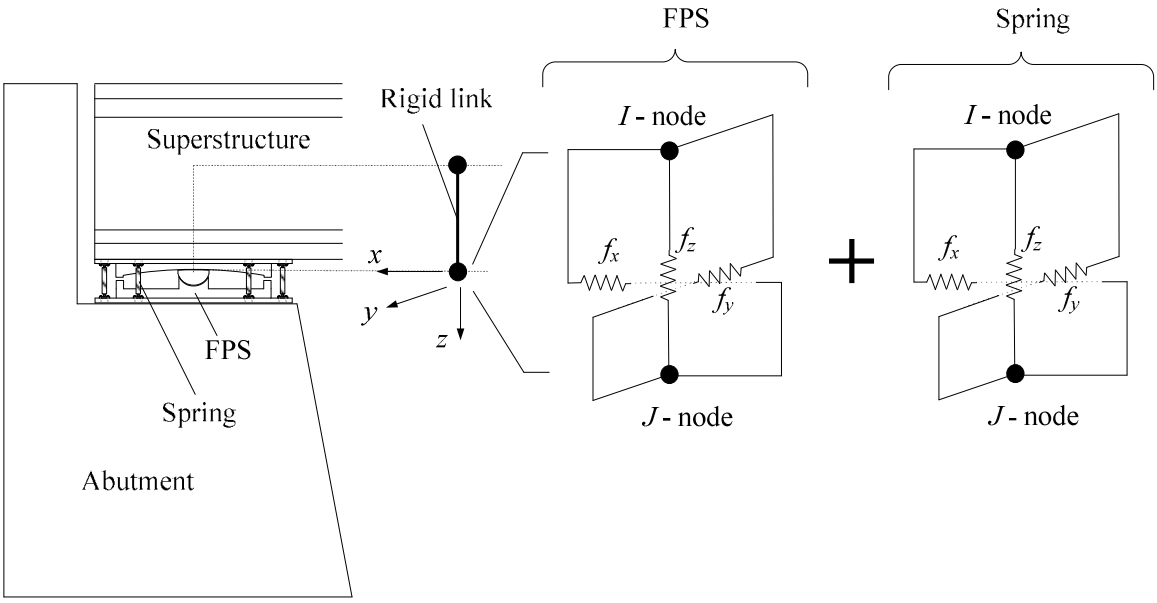

Figure 7.15 Modified isolator design modeling at the abutments.

7.3.2 Analyses

The bridge seismically isolated with the proposed modified design is analyzed with the same methodology used in the previous sections for a range of R and k_s. The

objective is to quantify the effects of the modified bridge seismic isolation approach. The fundamental period of the base bridge model was T_1=2.38 s. Five new modified designs are introduced. Each design is attained by one of the standard *R*'*s* of the isolators provided by the manufacturing company. The stiffness of the supplemental springs in the isolators located at the abutments is selected to result in the same fundamental seismic isolation period of the bridges (Table 7.3).

Table 7.3 Modified isolator design properties to achieve a fundamental period of T_1=2.38 s

R	k_p / k_s
99	-
155	0.640
224	0.287
305	0.176
396	0.120
620	0.070

Although the shape of the vibration modes in the modified isolation designs remained the same, the period of the third mode shapes of the bridges had notable differences compared to the base model. The value of the T_3 of the bridges for the five values of the *R* ranging from 155 cm to 620 cm in Table 7.3 were, 1.62, 1.48, 1.42, 1.38 and 1.34 s, respectively. This indicates that the torsional vibration characteristics of the modified designs are stiffer than the base model. It is also observed that although the post-yield stiffness of the isolators is reduced with increasing *R*, the torionsal stiffness increases. This is an attribute of the supplemental stiffness provided at the abutment

isolators to acquire the same fundamental period in the bridges isolated with the modified design approach.

7.3.3 Results

The median of the response quantities as a function of the R of the isolators are given in Figure 7.16. It is observed that the new seismic isolation strategy may result in considerable improvements in the response of the bridge. The median values of the MNF and d_{max} reduces and reaches a flatter plateau as the R increases. Additionally, the highest value of the d_{max} among the suite of ground motions reduces with the new seismic isolation strategy. The increased R implies more flexible isolators at the piers and consequently the MND slightly increases. However, the MND_{pier} / $MND_{abutment}$ is increased with the new isolation strategy. The ratio ΣMNF_{pier} / $\Sigma MNF_{abutment}$, reduces, indicating more energy and force transfer to the abutments. This ratio becomes approximately equal to 1, implying a completely uniform MND distribution throughout the isolators, for approximately R = 620 cm. Similar uniformity in the MNF is captured at approximately R = 244 cm.

Figure 7.17 shows the longitudinal force-deformation, of the FPS on top of the pier and abutment for the Helena earthquake record for the cases of conventional design with R = 99 cm and the new design with R = 620 cm. It is observed that the new design allows for considerable reduction in the MNF and stiffness on top of the isolator located on top of the pier. This is the fundamental principle underlying the objective of the new design. However, the stiffness of the isolator on top of the abutment has increased. This allowed higher isolator forces to be transferred to the abutments, which are typically structurally stronger components compared to the piers. Additionally, the isolator deformations of the abutment slightly reduced.

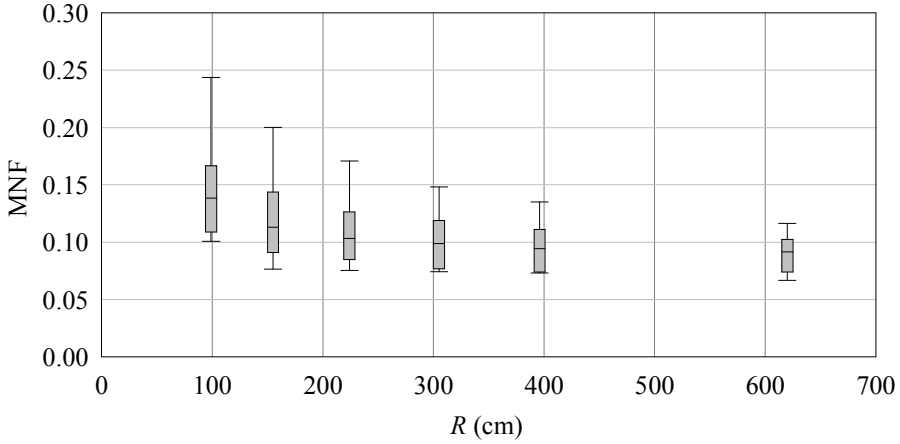
0.30
0.25
0.20
0.15
0.10
0.05
0.00
MNF
0
100
200
300
400
500
600
700
R (cm)

(a)

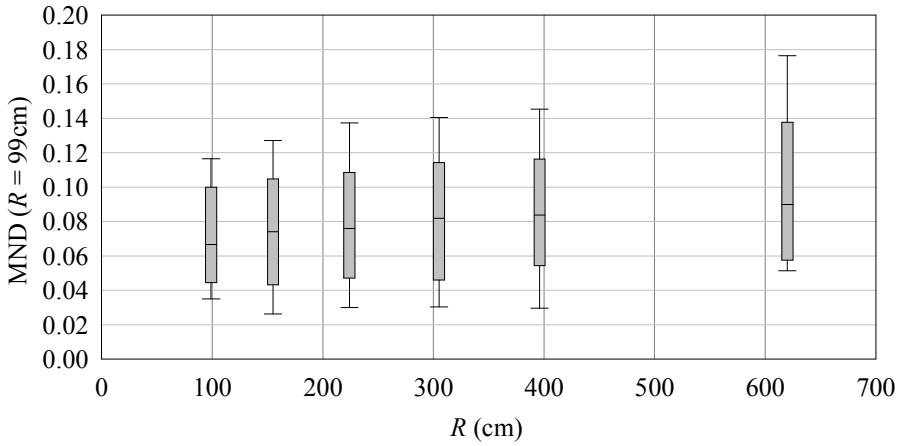
0.20
0.18
0.16
0.14
0.12
0.10
0.08
0.06
0.04
0.02
0.00
MND (R = 99cm)
0
100
200
300
400
500
600
700
R (cm)

(b)

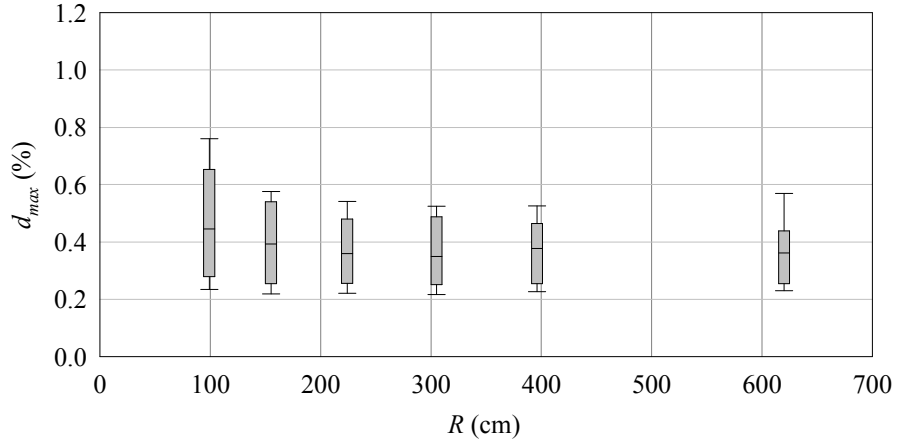
1.2
1.0
0.8
0.6
0.4
0.2
0.0
d_max (%)
0
100
200
300
400
500
600
700
R (cm)

(c)

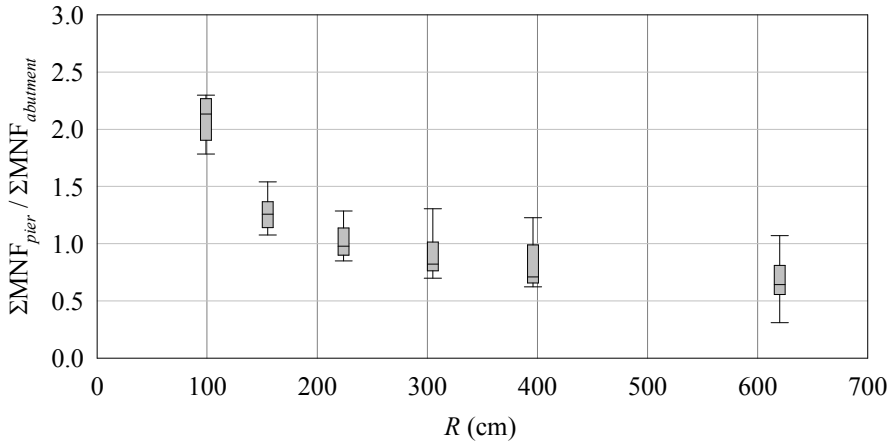

(d)

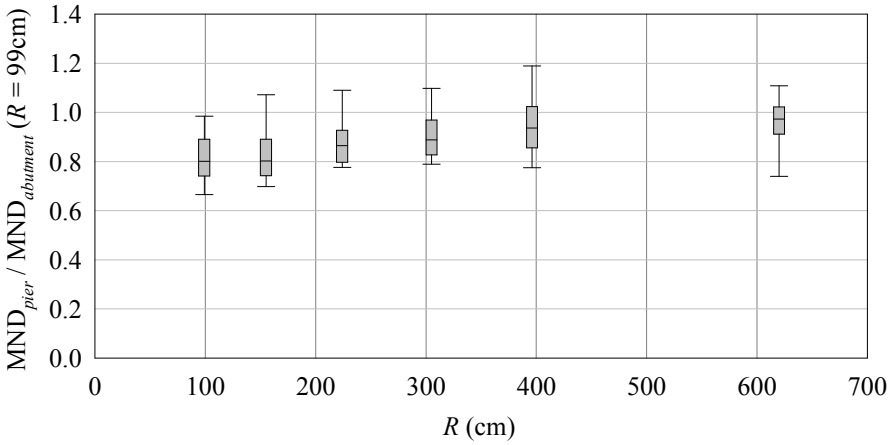

(e)

Figure 7.16 Variation of bridge response quantities as a function of FPS design parameters.

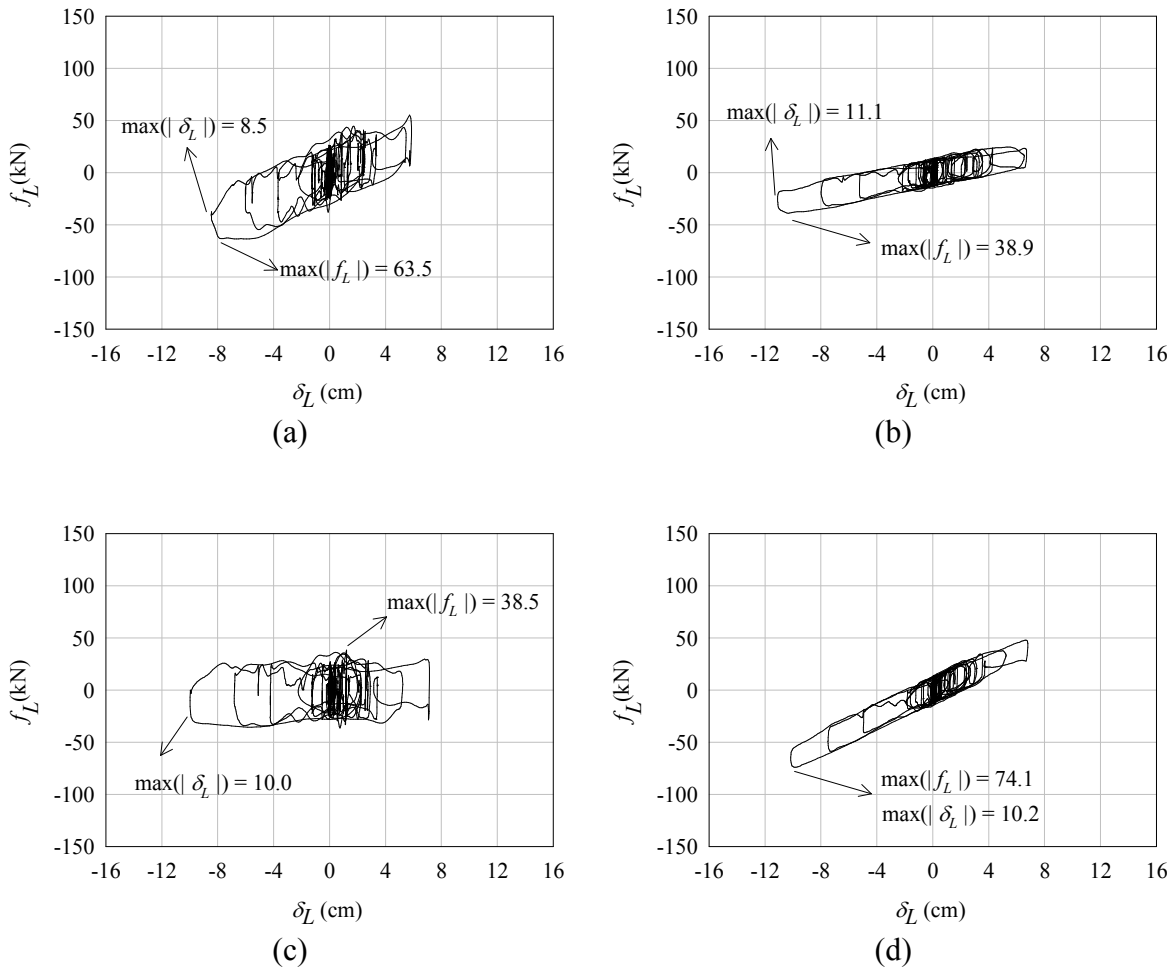

Figure 7.17 Force-deformation history of the FPS in the longitudinal direction for the Helena earthquake (a), (b) conventional design with R = 99 cm; (c), (d) new design with R = 621 cm; (a), (c) on top of the pier; (b), (d)on top of the abutment.

7.4 Conclusion

In this Chapter the influence of the common bridge design parameters on the system's response quantities have been investigated. A new seismic isolation strategy using a modified FPS design at the abutments has been presented. The influence of the design parameters in this new seismic isolation approach has been parametrically investigated. The following conclusions have been made:

1) The two design parameters that had the highest effect on the response quantities of the SIB were column height, L_c, and superstructure dead weight which was imposed via additional superstructure length, L_d^*. Both design parameters also had a notable effect on the fundamental period of the bridge
2) Larger substructure flexibility may result form base modeling assumptions or longer piers. SIBs with flexible substructures acquire higher vibration periods thus lower earthquake forces. However, flexible substructure reduces the effectiveness of seismic isolation. As the flexibility of the substructure of SIBs increase, the capacity to utilize the isolators at the piers tend to reduce and the deviation between the responses of the isolators located on top of the piers and abutments increase.
3) SIBs with larger superstructure mass acquire higher vibration periods. Increased superstructure mass, reduces the isolator deformations and increases the demands on the substructure components.
4) Increased superstructure flexibility acquired via longer span length dampens the inertial loads caused by the vertical components of the superstructure. This results in lower isolator forces and structural demands on the substructure. However, increased superstructure flexibility contributed to the variation between the responses of the isolators located on top the piers and the abutments.
5) Bridge skew has negligible effect on SIBs. This is mainly due to the uncoupling of the superstructure from the superstructure. The substructure nominal concrete strength had negligible effect on the response of the bridge.
6) The modified isolator design effectively increases the post-yield stiffness and energy dissipation capacity of the FPS utilizing springs widely found in the industry. This new design can be tailored to achieve different isolator force-deformation properties by changing the design, material and number of springs.

7) The new seismic isolation strategy allowed for a more balanced distribution of isolator forces and displacements throughout the bridge. This was achieved using the standard isolator dimensions manufactured by the parent company.
8) When compared to the conventional seismic isolation approach, the new strategy reduced the isolator deformation demands by utilizing the isolators more evenly at the abutments and piers.

CHAPTER 8

SUMMARY, CONCLUSIONS, AND FUTURE RESEARCH

8.1 Summary and Conclusions

Seismic isolation is an effective tool for improving the structural performance of bridges susceptible to earthquake induced loads. The dynamic response of bridges may be shifted towards higher periods via isolators to attract lower seismic forces. Isolators typically govern the dynamic characteristics of bridges and may be a powerful tool to calibrate the system's seismic response to a desired level by the designer. Currently, seismic isolators are classified as sliding and elastomeric. Despite being considered a relatively mature technology, sliding seismic isolation has been incorporated in bridge design codes only in 1997 and has not found wide-spread use particularly in the highway bridge community. One reason for this is the absence adequate analytical models that can capture the highly nonlinear behavior of the isolators. In addition, current seismic isolation design codes do not provide any guidance about the selection of isolator types. Examination of the affects of bridge and isolator design parameters on the system's seismic response has been limited. The objective of this study is to enhance the understanding of the structural response of bridges utilizing sliding seismic isolation via models that can capture the complex behavior of the isolators. This study was intended to provide support for seismic risk mitigation and insight for the analysis and design of SIBs by quantifying response characteristics. The Fiction Pendulum System (FPS) was selected as the representative isolator and given particular emphasis in the analyses.

The review of the current-state-of-the-art on bridge seismic isolation studies showed that there are three issues that need further clarification:

1) The level of accuracy required for modeling the force-deformation behavior of isolators;

2) The comparative response of the two main types of seismic isolators (i.e. sliding and elastomeric);
3) The influence of bridge and isolator design parameters on the system's response.

The influence of seismic isolation in a simplified bridge model was examined via modal analysis. It was shown that: (1) dynamic loads are substantially reduced via the insertion of a flexible element between the substructure and the superstructure; (2) vibration modes are governed by those involving the isolators; (3) the characteristics of the isolators are an important determinant of the dynamic response of the bridge. The nonlinear time-history (NLTH) analysis was selected as the method for further examination of SIB response.

A new finite element (FE) model of the FPS was implemented into the existing library of OpenSees. New C++ material and element classes were developed and compiled into the open source framework of OpenSees to model the response of the FPS. This model makes use of the existing research findings on the response components of the FPS. Unlike previous models in the literature, this model can account simultaneously for the variation in the normal force and friction coefficient, large deformation effects, and the coupling of the vertical and horizontal response during motion. The FE model was validated using experimental data from shake table tests of structures seismically isolated with the FPS. The influence of the modeling assumptions on the force-deformation response of the FPS was monitored on the developed for the verification study.

The response of typical highway bridges isolated with the FPS was investigated as a function of isolator modeling assumptions. A Multi-Span Continuous Steel Girder (MSCSG) bridge was used for this purpose. Three-dimensional (3-D) model of the bridge isolated with the FPS was developed. The bridge was modeled with a high degree of detail of the substructure components, and base and other boundary conditions. The new

FE model developed for the FPS was incorporated into the bridge model. Seven other models of the SIB were generated with the only difference in the FPS modeling assumptions. Each model Isolator and bridge response characteristics were monitored under NLTH analyses that utilized 2% in 50 years hazard level earthquakes. It was concluded that, the most important modeling aspects of the FPS in bridge applications are the normal force and friction coefficient variations, and bidirectional coupling. These parameters may have considerable effects on isolator design. However, the effects of the accuracy of these modeling parameters on bridge structural response are weak to moderate. Large deformation effects of the isolators were found to be negligible for the systems considered in this study. Pounding between the deck and the abutments may occur due to increased deformations at the isolator level. This occurrence limits the effectiveness of the isolators and may lead to unanticipated structural damage.

The seismic response characteristics of a Multi-Span Continuous Concrete Girder (MSCCG) bridge with: (a) sliding (b) elastomeric seismic isolation was compared using advanced isolator models. The FPS and the Lead-Rubber Bearings (LRB) were selected as representative isolators for sliding and elastomeric seismic isolators types, respectively. A new FE model of the LRB has been implemented into the existing library of OpenSees using a similar approach adopted for the FPS. In addition to accounting for bidirectional coupling effects available in models found in the literature, this model can account simultaneously for the variation in the normal force and large deformation effects. Two models of a Multi-Span Continuous Concrete Girder (MSCCG) bridge were generated and one was isolated with the LRB and the other was isolated with the FPS with approximately the same seismic isolation periods. The two bridge models were subjected to NLTH with a suite of 7% probability of exceedance in 75 years hazard level earthquake records. The influence of vertical components of the ground motions on the two isolators was assessed. Isolator and bridge response characteristics were monitored for the two seismic isolation schemes. It was concluded that unlike the FPS, the LRB

force-deformation response is significantly affected from large deformations. There is a notable loss of lateral stiffness in LRB at large deformations that may lead also lead to buckling. The influence of normal load variations on the force-deformation characteristics of the LRB was weak. The choice of elastomeric or sliding seismic isolation of bridges may have considerable effects despite attaining similar vibration periods. The LRB acquired higher displacements, however, placed smaller demands on the columns compared to the FPS. The FPS is capable of accommodating vertical components of the ground motion records that might result in a buckling failure of the LRB. The LRB possesses a more uniform response among isolators located at the abutments and piers in comparison to the FPS.

The influence of the design characteristics of the bridge and the isolators on the system's seismic response was examined. The previously established MSCCG bridge models were used for this task. Five bridge design parameters were selected. The range of these design parameters were established based on previous inventory analyses performed in the Central and Southeastern United States. Nonlinear time history analyses were performed by changing the design parameters within the four equally spaced values of their established bounds. Previously selected suite of 7% probability of exceedance in 75 years hazard level earthquake records were used in the analyses. Linear regression curves for the median values of the response quantities were developed from the results of the analyses. The slope of these regression curves were used to quantify the significance of the design parameters on the system's response. A new bridge seismic isolation strategy that involves a practical modification in the design of the FPS was proposed. The objective was to increase the effectiveness of seismic isolation with the FPS by achieving a more uniform response among isolators located at the piers and the abutments. The implications of the proposed design on the FPS force-deformation response were examined. The seismic response of the system was investigated as a function of different parameters of this new seismic isolation strategy. It was concluded

that seismic isolation with the FPS is less effective for bridges that have flexible substructure characteristics, compared with those that are less flexible. Base conditions and column height were identified as the two parameters to impact substructure flexibility the most. Bridges with large superstructure flexibility tend to be effected less from the effects of the vertical components of the ground motions. Bridges with large superstructure mass acquires less isolator displacements but place larger demands on the load carrying elements in the substructure. Unlike non-isolated bridges, the seismic response characteristics of bridges seismically isolated with the FPS were not affected by skew. The two disadvantages of the FPS are: (1) the limitation of the design parameters to attain desired force-deformation response characteristics and; (2) the significant variation in the force-deformation responses characteristics of the isolators located at the piers and the abutments. A new design approach for the FPS is proposed to overcome these limitations. This modification involves installing supplemental springs around the isolator to provide latitude for alternate force-deformation characteristics. It was possible to reduce structural demands on the load carrying elements of the bridge by creating a more uniform response among isolators located at the piers and abutments via the new design.

8.2 Future Research

The following are possible areas which this research can be extended to:

- Ground motions have a wide range of variability in their characteristics stemming from proximity, frequency content and directivity. The influence of ground motion characteristics on the seismic response of SIBs should be examined.
- Seismic isolation is applicable to virtually any type of bridge. The structural and dynamic characteristics of these bridges may have significant variations. The effectiveness of isolators on different bridge types should be quantified.

- A cost-benefit analysis should be performed for a range of isolator and bridge types. This will contribute to the wider application of the seismic isolation technology by making these elements a catalog commodity for design.
- Buildings typically possess larger overturning moments compared to bridges. Additionally, the design objectives and the placement of isolators in buildings have significant differences from bridges. The influence of isolator modeling assumptions and the selection of the type of seismic isolator on building response should be investigated.
- Possible improvements with hybrid seismic isolation schemes should be explored. In addition to considering different isolator types, these scenarios should include retrofit techniques based on strengthening such as jacketing, and other protective devices such as dampers.

APPENDIX A

METHOD OVERRIDING IN C++

Open System for Earthquake Engineering Simulation (OpenSees) is an open source software framework for simulating the earthquake response of structural and geotechnical systems (Mazzoni et al. 2006). OpenSees has an open source object-oriented architecture in the C++ programming language that maximizes its modularity, thus making it a viable choice for research purposes. This framework has been used to simulate the complex force-deformation response of the FPS and the LRB isolators. Despite the availability of versatile *material* and *element* models inside the library of OpenSees, none has the capability of effectively modeling the complex force-deformation response of the isolators described in chapters 4 and 6. A material class, *FPSmaterial,* and a zero-length element class, *FPSelement*, has been added to the existing library of OpenSees to model the force-deformation response of the FPS (McKenna 2005a; McKenna 2005b). These classes were derived as child classes of the existing generic *UniaxialMaterial* and *ZeroLength* parent classes. A critical approach used to achieve this task was 'overriding'.

The parent *UniaxialMaterial* class has a method called: `setTrialStrain` which is designed to take in two parameters: (1) strain (`strain`) and; (2) strain rate (`strainRate`) at step *i* of the analysis and update the values of trial stress (`Tstress`) and trial tangent stiffness (`Ttangent`) values based on the predefined constitutive relationship for step *i+1*. The `setTrialStrain` method defined in the parent *UniaxialMaterial* class is pure virtual base class thus no objects of it's type can be instantiated. Classes derived from the *UniaxialMaterial* class must implement the `setTrialStrain` method to avoid a compiler error. However, the constitutive relationship defined for the FPS in

Chapter 4 requires additional parameters to the default ones. To achieve this, the `setTrialStrain` is kept inside the code but designed to not function by:

```
int FPSMaterial::setTrialStrain(double strain, double strainRate)
{return 0;}
```

A new `setTrialStrain method` to override the existing default one in *FPSmaterial* is generated from:

```
int FPSMaterial::setTrialStrain(double frictionC, double Alpha, double
zz, double n_modified, double strain, double strainRate)
```

where `frictionC` is μ (Equation 4.3), `Alpha` is α (Equation 4.12), `zz` is the corresponding parameter of $\boldsymbol{\eta}$ (Equation 4.8), `n_modified` is *N* (Equation 4.2). This overriding method is also added to the header file of the parent *UniaxialMaterial* class:

```
virtual int setTrialStrain (double frictionC, double Alpha, double zz,
double n_modified, double strain, double strainRate) {return 0;}
```

The utilization of the new `setTrialStrain` method inside the *FPSelement* is as following:

```
for (int mat=0; mat<3; mat++) {
  if(mat==0){
     strain     = this->computeCurrentStrain1d(0,diff);
     strainRate = this->computeCurrentStrain1d(0,diffv);

     ret += theMaterial1d[mat]-
>setTrialStrain(frictionC_x,Alpha,y1,n_modified,strain,strainRate);}

  else if(mat==1) {
     strain     = this->computeCurrentStrain1d(1,diff)
     strainRate = this->computeCurrentStrain1d(1,diffv);

     ret += theMaterial1d[mat]-
>setTrialStrain(frictionC_y,Alpha,y2,n_modified,strain,strainRate);}

  else {
     strain     = this->computeCurrentStrain1d(mat,diff );
     strainRate = this->computeCurrentStrain1d(mat,diffv);

     ret += theMaterial1d[mat]->setTrialStrain(strain,strainRate);}
            }
```

APPENDIX B

REGRESSION LINES FOR THE EFFECTS OF BRIDGE DESIGN PARAMETERS ON SYSTEM RESPONSE

The following figures present the variation of maximum normalized force and displacement of the FPS isolators located on top of the pier, MNF and MND, maximum column drifts, d_{max}, the ratio of the total MNF transferred to the pier and the total MNF transferred to the abutment, $\Sigma MNF_{pier} / \Sigma MNF_{abutment}$, the ratio of the MND on top of the abutment and MND on top of the pier, $MND_{pier} / MND_{abutment}$, for the earthquakes used in chapter 7. The bridges design parameters considered are column height, L_c, length of the superstructure with constant mass, L_d, length of the superstructure with adjusted mass, L_d*, degree of skew, a, and the nominal concrete strength of the substructure, f_c. Figures a re given as a ratio of the design parameters to the base model design values denoted by a subscript 'o' of the design parameter. The term a denotes the slope of the linear regression curve established from the median values of the response quantities as a function of the design parameters. The term R^2 is the coefficient of multiple determination used to measure the amount of reduction in the variability of the response quantity median by the design parameter variables.

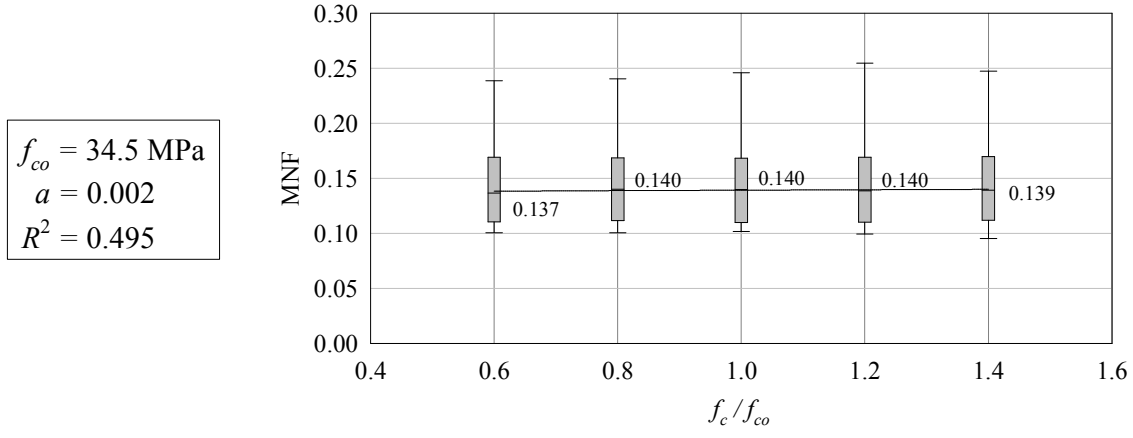

(a)

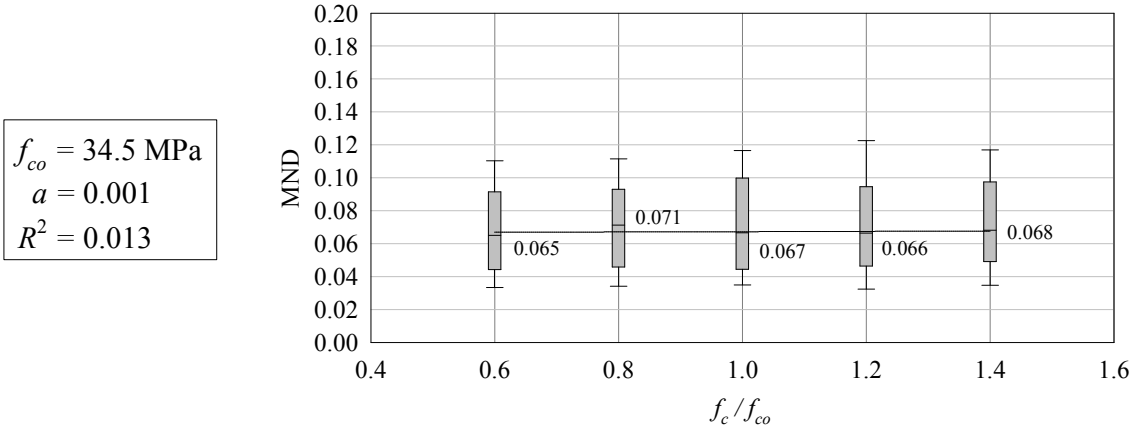

(b)

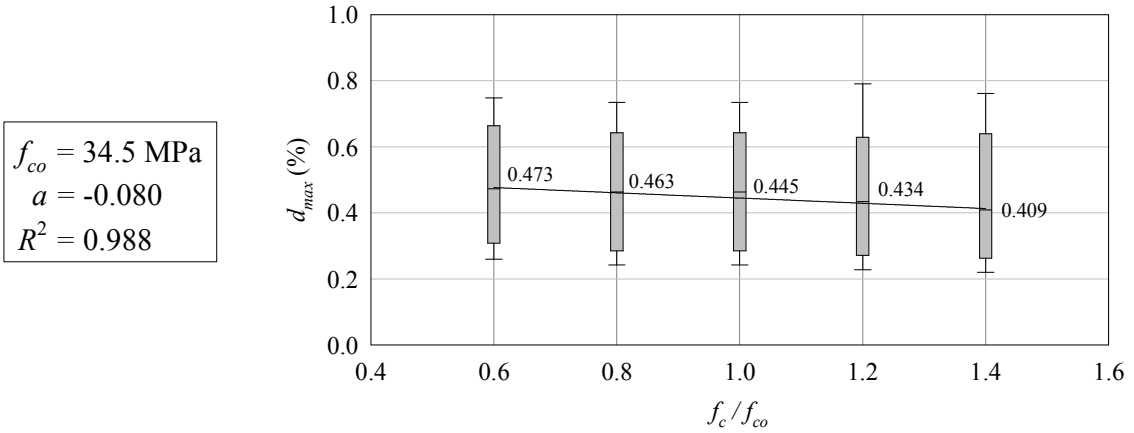

(c)

Figure B.1 The influence of the pier concrete compressive strength, f_c, on (a) MNF (b) MND (c) d_{max} (d) ΣMNF_{pier} / $\Sigma MNF_{abutment}$ (e) MND_{pier} / $MND_{abutment}$

f_{co} = 34.5 MPa
a = 0.106
R^2 = 0.912

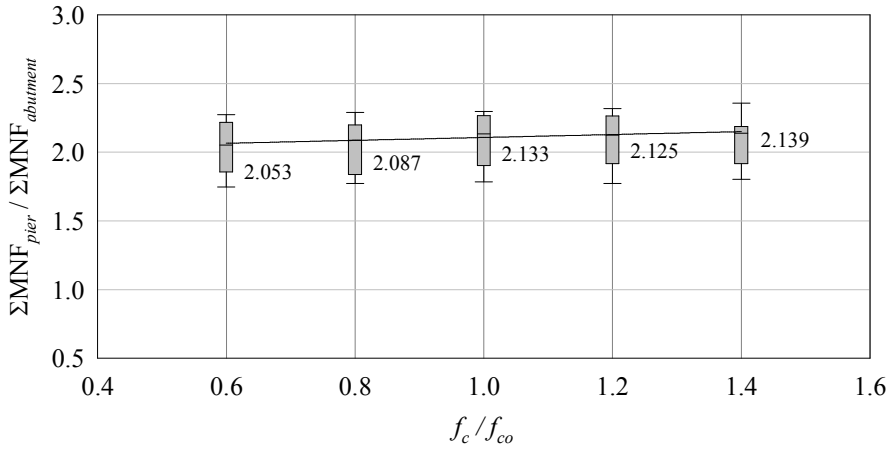

(d)

f_{co} = 34.5 MPa
a = 0.056
R^2 = 0.896

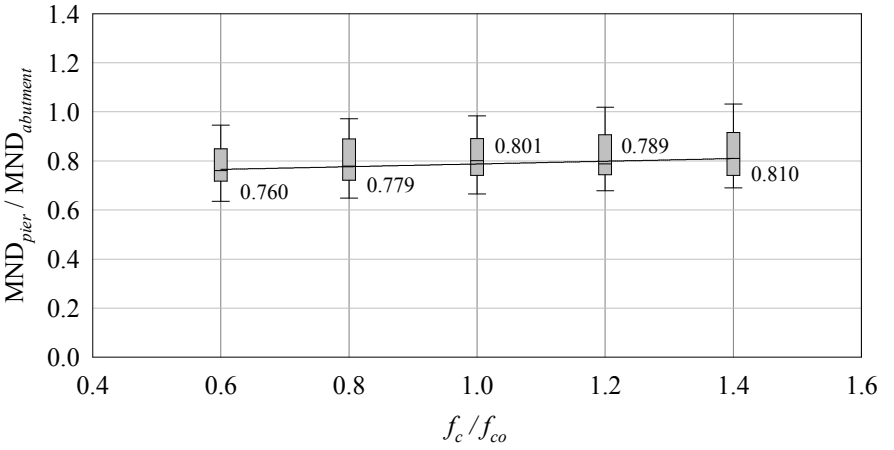

(e)

Figure B.1 continued

L_{co} = 4.6 m
a = -0.044
R^2 = 0.906

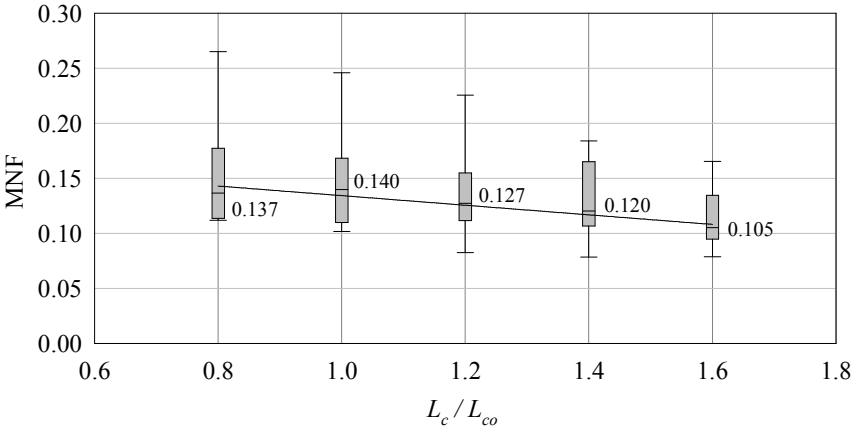

(a)

L_{co} = 4.6 m
a = -0.042
R^2 = 0.972

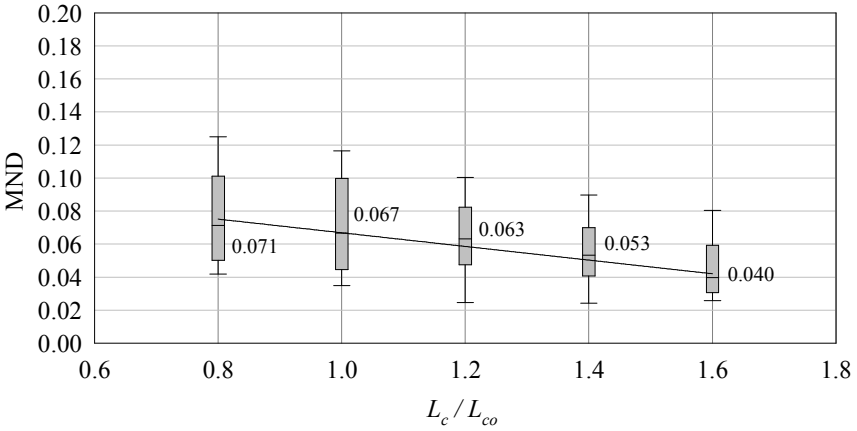

(b)

L_{co} = 4.6 m
a = 0.351
R^2 = 0.965

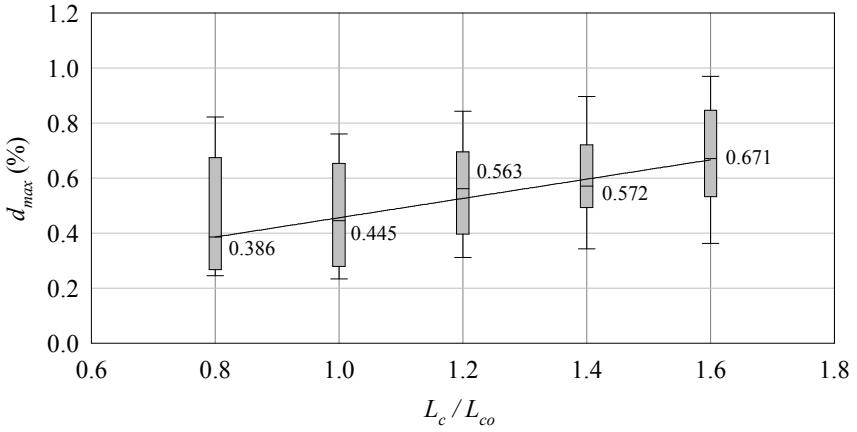

(c)

Figure B.2 The influence of the column length, L_c, on (a) MNF (b) MND (c) d_{max} (d) ΣMNF_{pier} / $\Sigma MNF_{abutment}$ (e) MND_{pier} / $MND_{abutment}$

L_{co} = 4.6 m
a = -0.792
R^2 = 0.954

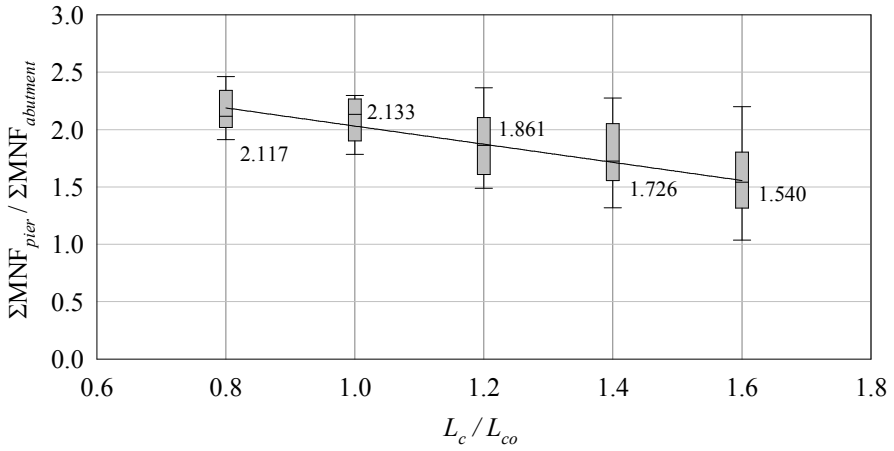

(d)

L_{co} = 4.6 m
a = -0.497
R^2 = 0.994

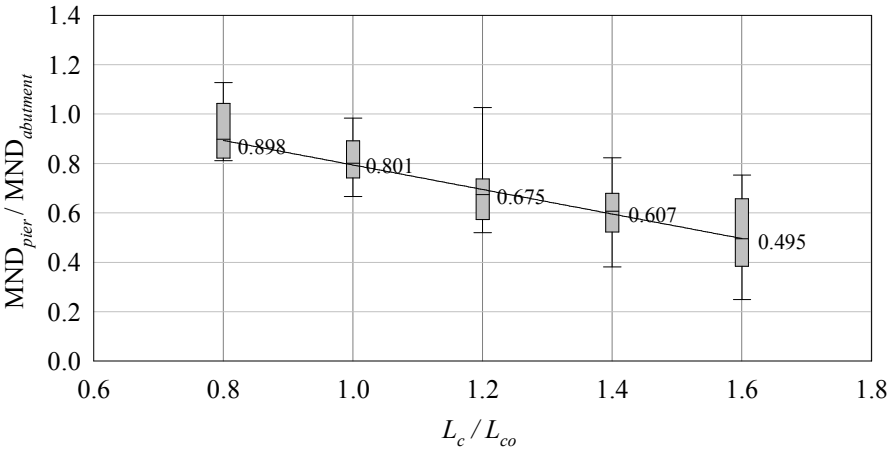

(e)

Figure B.2 continued

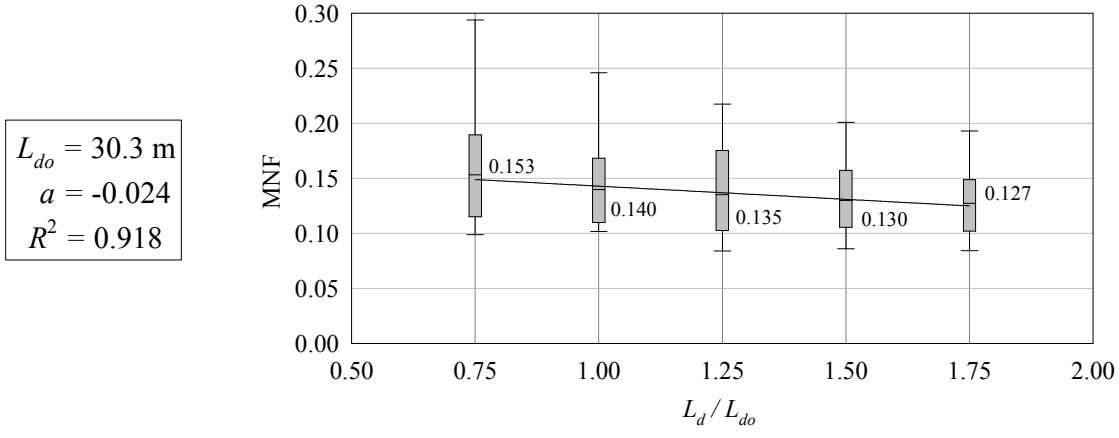

(a)

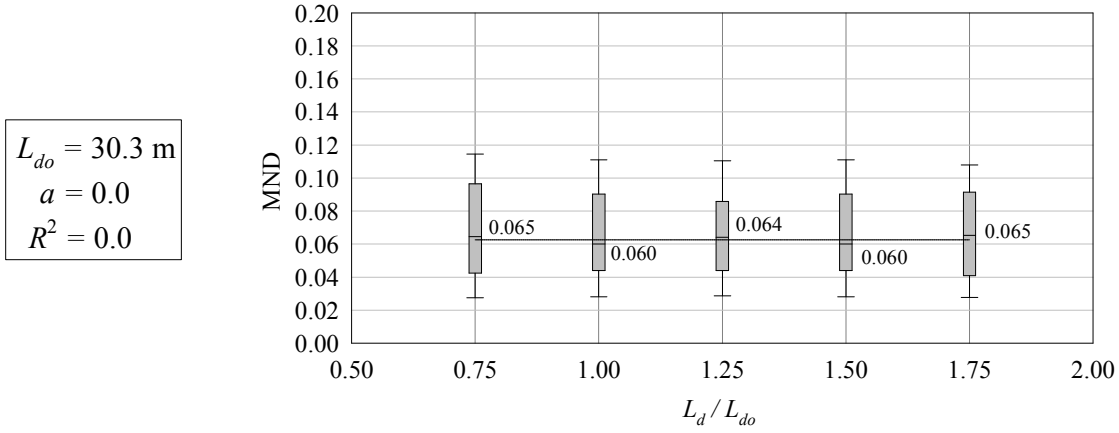

(b)

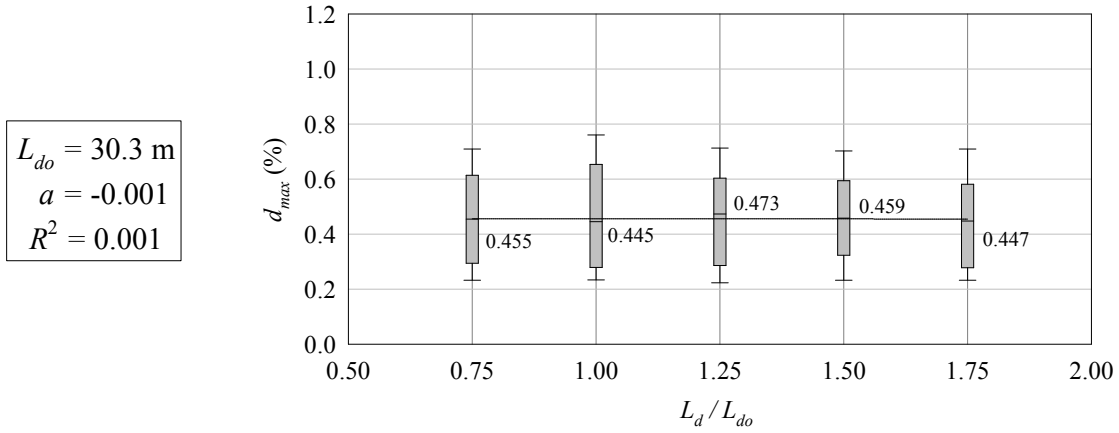

(c)

Figure B.3 The influence of longitudinal deck length, L_d, with constant mass on (a) MNF (b) MND (c) d_{max} (d) ΣMNF_{pier} / $\Sigma MNF_{abutment}$ (e) MND_{pier} / $MND_{abutment}$

L_{do} = 30.3 m
a = -0.222
R^2 = 0.708

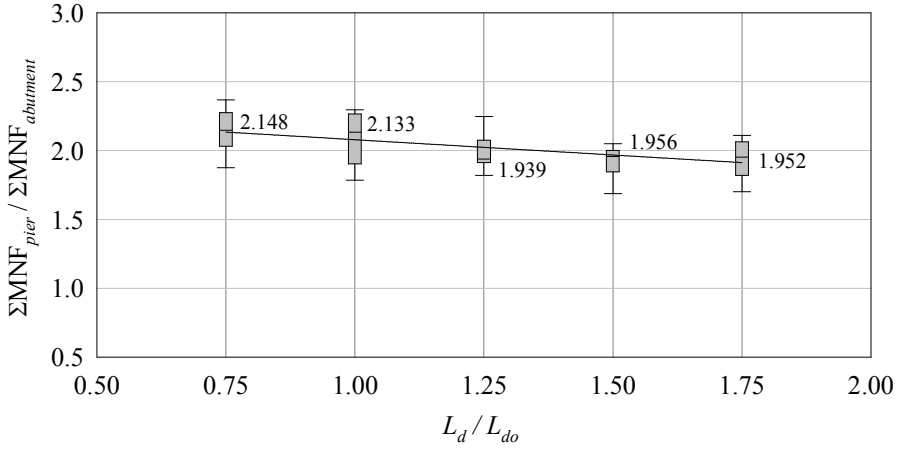

(d)

L_{do} = 30.3 m
a = -0.051
R^2 = 0.466

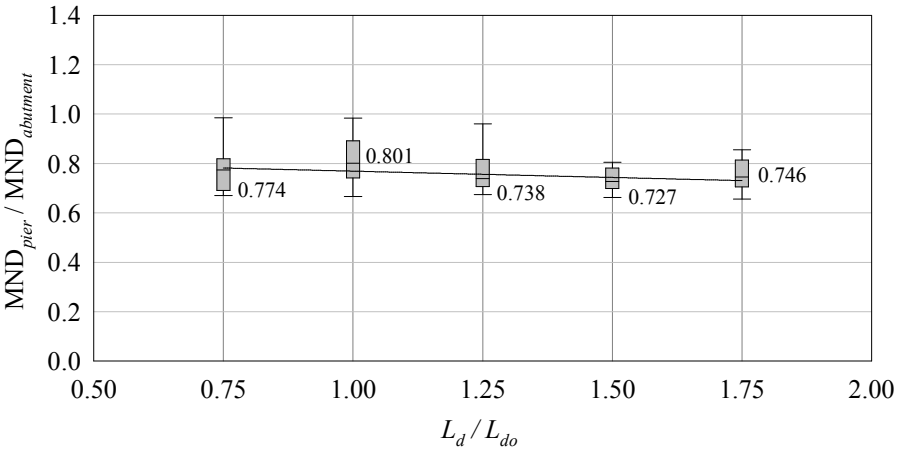

(e)

Figure B.3 continued

L_{do} = 30.3 m
a = 0.093
R^2 = 0.975

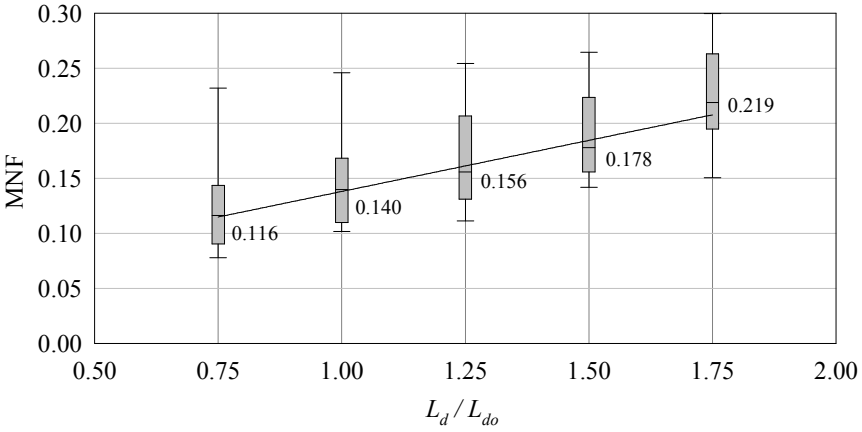

(a)

L_{do} = 30.3 m
a = -0.016
R^2 = 0.796

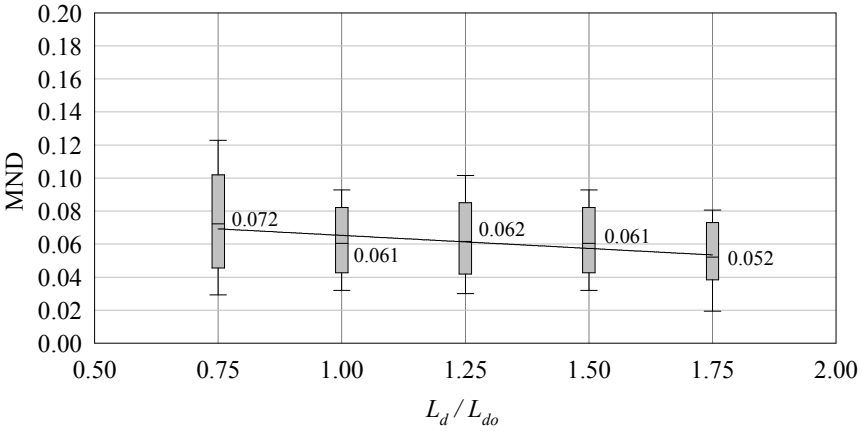

(b)

L_{do} = 30.3 m
a = 0.674
R^2 = 0.987

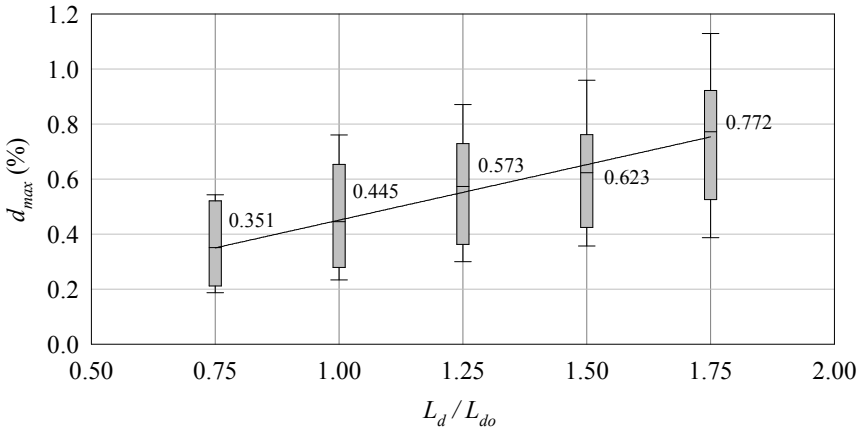

(c)

Figure B.4 The influence of longitudinal deck length, L_d, with adjusted mass on (a) MNF (b) MND (c) d_{max} (d) ΣMNF_{pier} / $\Sigma MNF_{abutment}$ (e) MND_{pier} / $MND_{abutment}$

L_{do} = 30.3 m
a = -0.643
R^2 = 0.978

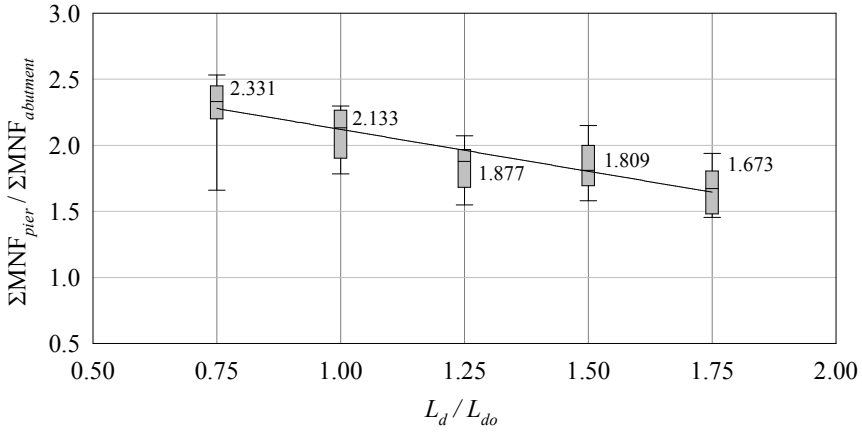

(d)

L_{do} = 30.3 m
a = -0.211
R^2 = 0.979

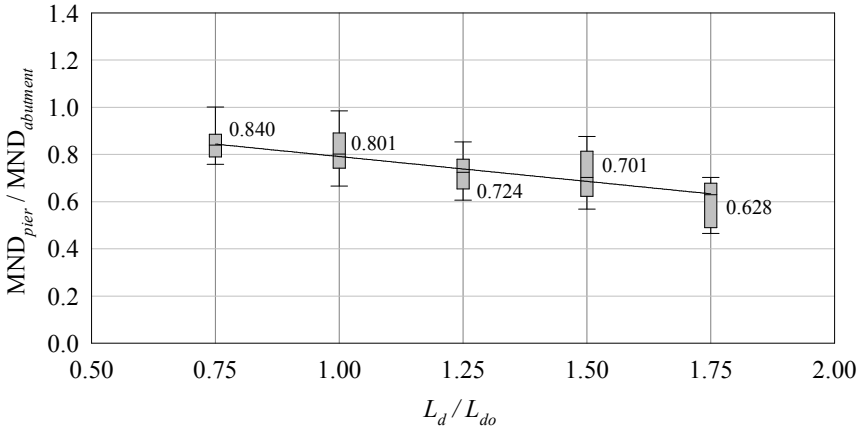

(e)

Figure B.4 continued

$\alpha_o = 0^o$
$a = -0.001$
$R^2 = 0.200$

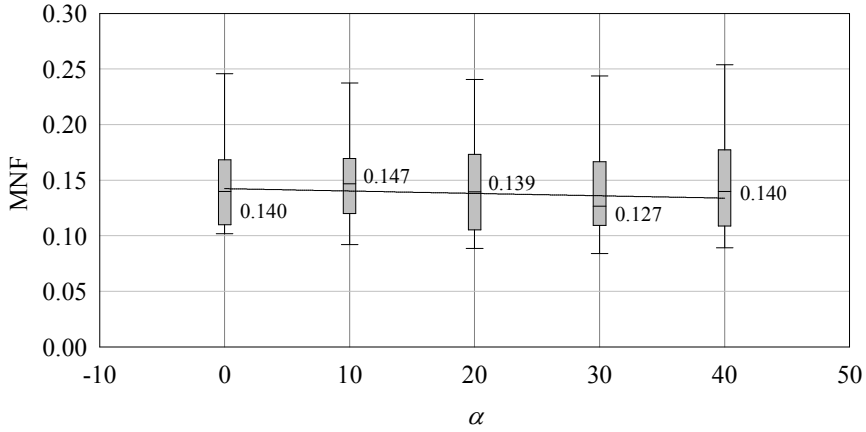

(a)

$\alpha_o = 0^o$
$a = 0.0$
$R^2 = 0.0$

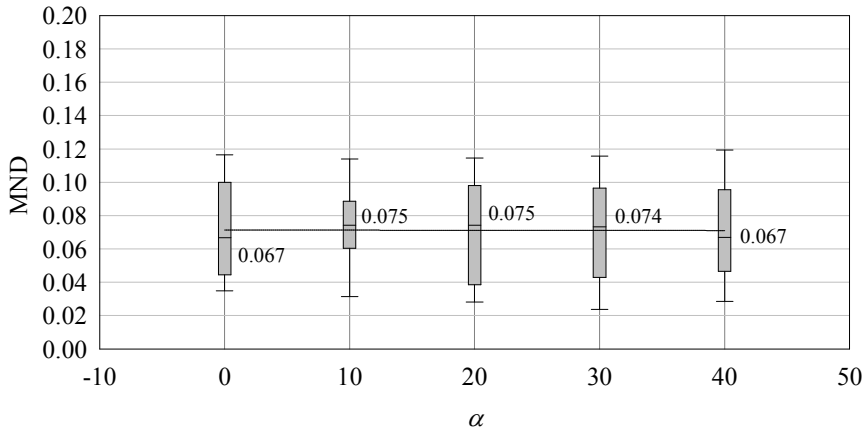

(b)

$\alpha_o = 0^o$
$a = -0.001$
$R^2 = 0.530$

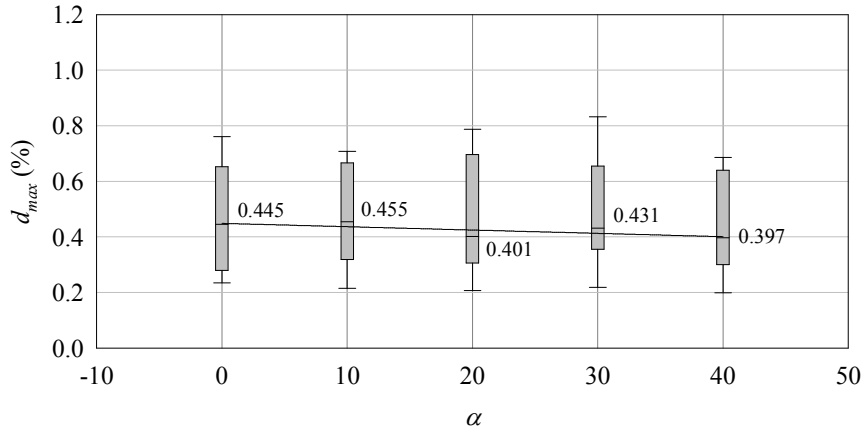

(c)

Figure B.5 The influence of skew angle, α, on (a) MNF (b) MND (c) d_{max} (d) ΣMNF_{pier} / $\Sigma MNF_{abutment}$ (e) MND_{pier} / $MND_{abutment}$

$\alpha_o = 0^o$
$a = -0.002$
$R^2 = 0.157$

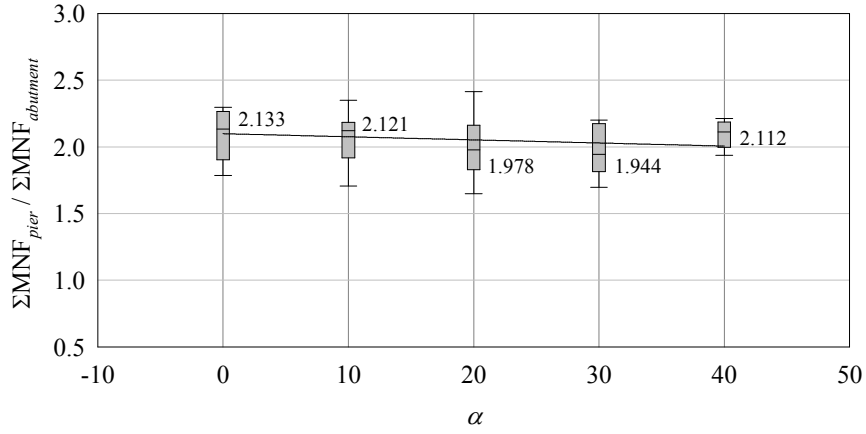

(d)

$\alpha_o = 0^o$
$a = 0.0$
$R^2 = 0.003$

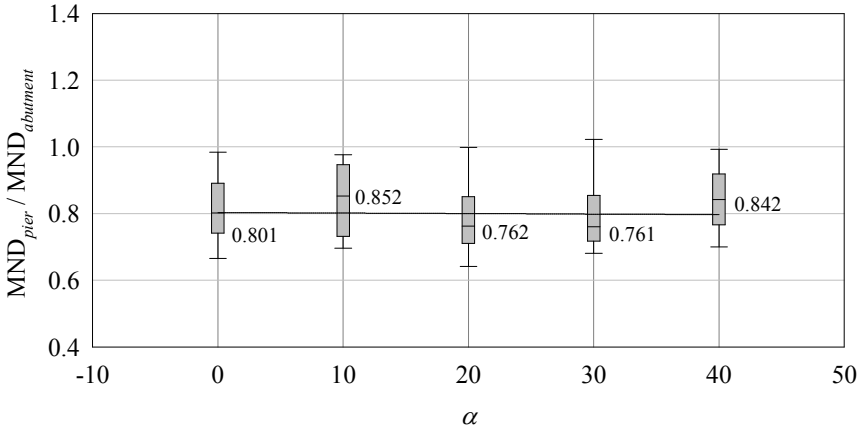

(e)

Figure B.5 continued

REFERENCES

AASHO (1965). *Standard specifications for highway bridges*, Washington D.C.

AASHTO (1999). *Guide specifications for seismic isolation design*, Washington, D.C.

Almazan, JL, Llera, JCDL, and Inaudi, JA (1998). "Modeling aspects of structures isolated with the frictional pendulum system," *Earthquake Engineering and Structural Dynamics,* 27, 845-867

Almazan, JC and Llera, JCDL (2002). "Analytical model of structures with frictional pendulum isolators," *Earthquake Engineering and Structural Dynamics,* 31, 305-332

Almazan, JC and Llera, JCDL (2003). "Physical model for dynamic analysis of structures with FPS isolators," *Earthquake Engineering and Structural Dynamics,* 32, 1157-1184

Anderson, EL, and Mahin, A (2004). "An evaluation of bi-directional earthquake shaking on the provisions of the AASHTO Guide Specifications for Seismic Isolation Design," *13th World Conference on Earthquake Engineering*, Vancouver, B.C., Canada

Buckle, IG, Constantinou, MC, Dicleli, M, and Ghasemi, H (2006). *Seismic isolation of highway bridges*, Technical Report MCEER-06-SP07, Multidisciplinary Center for Earthquake Engineering Research, State University of New York at Buffalo

Buckle, IG and Liu, H (1993). "Stability of elastomeric seismic isolation systems," ATC *Seminar on Seismic Isolation, Passive Energy Dissipation and Control,* Redwood City, California

Buckle, IG and Mayes, RL (1990). "Seismic isolation: history, application and performance – a world review," *Earthquake Spectra,* 6(2)

Buckle, IG and Kelly, JM (1986). "Properties of slender elastomeric isolation bearings during shake table studies of a large-scale model bridge deck," *Joint Sealing and Bearing Systems for Concrete Structures (ACI)*, Vol. 1, 247-269

Button, MR, Cronin, CJ, Mayes, RL (2002). "Effect of vertical ground motions on seismic response of highway bridges," *Journal of Structural Engineering*, 128(12), 1551-1564

Carlson, H (1978). *Spring designer's handbook,* Marcel Dekker, New York

Chironis, NP (1961). *Spring designer and application,* McGraw Hill, New York

Chopra, AK (2001). *Dynamics of structures theory and applications to earthquake engineering,* 2nd Ed., Prentice Hall, New Jersey

Collier, CJ and Elnashai, AS (2001). "A procedure for combining vertical and horizontal seismic action effects," *Journal of Earthquake Engineering*, 5(4), 521-539

Constantinou, MC, Mokha, A, Reinhorn, A (1990). "Teflon bearings in base isolation. II: modeling," *Journal of Structural Engineering*, 116(2), 455-474

Constantinou, MC, Tsopelas, P, Kim, Y-S, and Okamoto, S (1993). *NCEER-Taisei corporation research program on sliding seismic isolation systems for bridges: experimental and analytical study of a friction pendulum system (fps),* Technical Report NCEER-93-0020, National Center for Earthquake Engineering Research, State University of New York at Buffalo

Cook, RD, Malkus, DS, Plesha, ME, and Witt, RJ (2002). *Concepts and applications of finite element analysis,* 4th Ed., Kohn Wiley & Sons, New York

Cooper, J, Friedland, IM, Buckle, IG, Nimis, RB, and Bobb, NM (1994). "The Northridge: progress made, lessons learned in seismic design of bridges," *Public Roads*, 58(1)

DIS (1996). *Earthquake performance of structures on lead-rubber isolations system*, Lafayette, California

Dicleli, M and Buddaram, S (2006). "Effect of isolator and ground motion characteristics on the performance of seismic-isolated bridges," *Earthquake Engineering and Structural Dynamics,* 35, 233-250

Dicleli, M, Albhaisi, S and Mansour, MY (2005). "Static soil-structure interaction effects in seismic-isolated bridges" *Practice Periodical on Structural Design and Construction,* 10(1), 22-33

Dicleli, M and Mansour, MY (2003). "Seismic retrofitting of bridges in Illinois using friction pendulum seismic isolation bearings and modeling procedures," *Engineering Structures,* 25, 1139-1156

Dicleli, M (2002). "Seismic design of lifeline bridge using hybrid seismic isolation," *Journal of Bridge Engineering*, 7(2), 94-103

Earthquake Protection Systems (2003). *Technical Characteristics of Friction Pendulum Bearings*, Vallejo, California

Erdik, M, and Uckan (2004). "Earthquake response of a 1:4 scaled three story steel structure seismically isolated by the FPS type sliding isolation system," *Proceedings of the Third European Conference on Structural Control*, Vienna, Austria

FEMA (1997). "NEHRP Recommended Provisions for Seismic Regulations for New Buildings and Other Structures, Part 1: Provisions." *Report No. FEMA 302*, Federal Emergency Management Agency

Fenves, GL (2005). "Brief notes on object-oriented software design and programming with C++," *OpenSees Developer`s Workshop*, Berkeley, California

Gardiner, WP, and Gettinby, G (1998). *Experimental design techniques in statistical practice,* Horwood Publishing Limited, West Sussex, England

Ghobarah, A and Ali, HM (1988). "Seismic performance of highway bridges," *Engineering Structures*, 10, 157-166

Ghobarah, A (1988). "Seismic behavior of highway bridges with base isolation," *Canadian Journal of Civil Engineering*, 15, 72-78

Göbel, EF and Brichta, AM (1978). *Rubber spring design,* Newnes-Butterworths, London

Hwang, JS and Hsu, TY (2000). "Experimental study of isolated building under triaxial ground excitations," *ASCE Journal of Structural Engineering*, 126(8), 879-886

Iemura, H, Taghikhany, T, Takahashi, Y and Jain, SK (2005). "Effect of variation of normal force on seismic performance of resilient sliding isolation systems in highway bridges," *Earthquake Engineering and Structural Dynamics*, 34, 1777-1797

International Code Council (2000). *International building code*, Falls Church, Virginia

Jangid, RS (2004). "Seismic response of isolated bridges," *Journal of Bridge Engineering,* Vol. 9, No. 2, 156-166

Jangid, RS (2004). "Optimum friction pendulum system for near-fault motions," *Engineering Structures,* 27(3), 349-359

Jangid, RS and Kelly, JM (2001). "Base isolation for near-fault motions," *Earthquake Engineering and Structural Dynamics*, 30, 691-707

Kasalanati, A and Constantinou, MC (2005). "Testing and modeling of prestressed isolators," *ASCE Journal of Structural Engineering*, 131(6), 857-866

Kelly, J (2003). "Tension buckling in multilayer elastomeric bearings," *Journal of Engineering Mechanics*, December, 1363-1368

Kelly, J (1997). Earthquake-*resistant design with rubber*, Springer-Verlag, London

Kelly, JM, Buckle, IG, Tsai, HC (1986). *Earthquake simulator testing of a base-isolated bridge deck*, Report No. EERC 1985-09, University of California, Berkeley

Kreyszeig, E (1999). *Advanced engineering mathematics,* 8th Ed., John Wiley & Sons, New York

Lee, HJ, and Schiesser, WE (2004). *Ordinary and partial differential equation routines in C, C++, Fortran, Java, Maple, and Matlab*, Chapman & Hall/Rc, Boca Raton

Lee, GC, Kitane, Y and Buckl, IG (2002). "Literature review of the observed performance of SIBs," *Research Progress and Accomplishments: 2001-2003, MCEER,* University at Buffalo State University of New York

Liao, W, Loh, CH, and Lee, BH (2004). "Comparison of dynamic response of isolated and non-isolated continuous girder bridges subjected to near-fault ground motions," *Engineering Structures,* 26(2004), 2173-2183

Maleki, S (2001a). "Free vibration of skewed bridges," *Journal of Vibration and Control*, 7, 935-952

Maleki, S (2001b). "Effects of diaphragms on seismic response of skewed bridges," *1First MIT Conference on Computational Fluid and Solid Mechanics*, June 12-15 2001

Mander, JB, Kim, DK, Chem, SS, and Premus, GJ (1996). "Response of steel bridge bearings to the reversed cyclic loading," Report *No. NCEER 96-0014*, NCEER, Buffalo, NY

Matsagar, VA and Jangid, RS (2004). "Influence of isolator characteristics on the response of base-isolated structures," *Engineering Structures*, 26, 1735-1749

Mayes, R (2002). "Impediments to the implementation of seismic isolation," *ATC Seminar on Response Modification Technologies for Performance-Based Seismic Design,* Los Angeles, California

Mazzoni, S, McKenna, FT, Scott, MH and Fenves, GL (2007). "Open System for Earthquake Engineering Simulation User Manual," <http://peer.berkeley.edu/~silvia/OpenSees/manual/html/>

McKenna, F (2005a). "Introducing a new uniaxial material into OpenSees," *OpenSees Developer`s Workshop*, Berkeley, California

McKenna, F (2005b). "Adding an element into OpenSees," *OpenSees Developer`s Workshop*, Berkeley, California

Mokha, AS, Constantinou, MC, Reinhorn, AM (1991). "Verification of friction model of Teflon bearings under triaxial load," *ASCE Journal of Structural Engineering*, 119(1), 240-261

Mokha, AS, Constantinou, MC, Reinhorn, AM (1991). "Further results on frictional properties of teflon bearings," *Journal of Structural Engineering*, 117(2), 622-626

Mokha, AS, Constantinou, MC, Reinhorn, AM (1990). "Teflon bearings in base isolation. I: testing." *Journal of Structural Engineering*, 116(2), 455-475

Mokha, AS, Constantinou, MC, Reinhorn, AM (1990). "Teflon bearings in base isolation. II: modeling." *Journal of Structural Engineering*, 116(2), 439-454

Montgomery, DC (2005). *Design and analysis of experiments,* 6th Edition*,* John Wiley & Sons, U.S.A.

Mosqueda, G, Whittaker, AS, Fenves, GL (2004). "Characterization and modeling of friction pendulum bearings subjected to multiple components of excitation," *Journal of Structural Engineering*, 130(3), 433-442

Muthukumar, S. (2003). "A Contact Element Approach with Hysteresis Damping for the Analysis and Design of Pounding in Bridges," PhD thesis, Georgia Institute of Technology.

Naeim, F and Kelly, J (1996). *Design of seismic isolated structures,* 1st Ed., Wiley, New York

Nakajima, K, Iemura, H, Takahashi, Y, Ogawa, K. (2000). "Pseudo dynamic tests and implementation of sliding bridge isolators with vertical motion," *12th World Conference on Earthquake Engineering*, Vancouver, Canada

Nielson, B (2005). "Analytical Fragility Curves for Highway Bridges in Moderate Seismic Zones," PhD thesis, Georgia Institute of Technology.

Ordonez, D, Foti, D and Bozzo, L (2003). "Comparative study of the inelastic response of base isolated buodings," *Earthquake Engineering and Structural Dynamics,* 32, 151-164

Palfalvi, B, Amin, A, Mokha, A, Fatehi, H, and Lee, P (1993). "Implementation issues in seismic isolation retrofit of government buildings." *ATC-17-1 Seminar on Seismic Isolation, Passive Energy Dissipation and Active Control,* San Francisco, CA, March.

Papazoglou, AJ and Elnashai, AS (1996). "Analytical and field evidence of the damaging effect of vertical earthquake ground motion," *Earthquake Engineering and Structural Dynamics,* 25, 1109-1137

PEER Strong Motion Database. (2000). Retrieved October 10, 2007 from http://peer.berkeley.edu/smcat/

Press, WH, Vetterling, WT, Teukolsky, SA, and Flannery, BP (2003). *Numerical recipes in C++: the art of scientific computing*, Cambridge University Press, Cambridge

Priestley, MJN, Seible, F and Calvi, GM (1996). *Seismic design and retrofit of bridges,* John Wiley and Sons, New York

Pritchard, PJ (1998). *MathCad: a tool for engineering problem solving*, McGraw-Hill Science

Rosenbrock, HH (1963). "Some general implicit processes for the numerical solution of differential equations" The Computer Journal, 5(4), 329-330

Ryan, KL and Chopra, AK (2005). *Estimating the seismic response of base-isolated buildings including torsion, rocking and axial-load effects,* Report No. EERC 2005-01, University of California, Berkeley

Saadeghvaziri, MA, and Futch, DA (1991). "Dynamic behavior of R/C highway bridges under the combined effect of vertical and horizontal earthquake motions," *Earthquake Engineering and Structural Dynamics,* 20, 535-549

Shenton, HW (1996). *Guidelines for pre-qualification, prototype and quality control testing of seismic isolation systems*, National Institute of Standards and Technology, Gaithersburg, Maryland

Shampine, LF, Gladwell, I, and Thompson, S (2003). *Solving ODEs with Matlab*, Cambridge University Press, New York

Silva, WJ (1997). "Characteristics of vertical strong ground motions for applications to engineering design," *Proceedings of the FHWA/NCEER Workshop on the National Representation of Seismic Ground Motion for New and Existing Highway Facilities*, Technical Report NCEER-97-0010

Skinner, RI, Robinson, WH, and McVerry, GH (1993). *An introduction to seismic isolation,* John Wiley & Sons, New York

Stanton, JF (1998). "The 1997 AASHTO seismic isolation guide specification," *Proceedings of the U.S.-Italy Workshop on Seismic Protective Systems for Bridges*, Technical Report MCEER-98-0015, New York

Stanton, J and Roeder, C (1991). "Advantages and limitations of seismic isolation," *Earthquake Spectr*, 7(2), 301-323

Stevens, A (1997). *Teach yourself C++,* 5th Edition, Henry Holt & Co., New York

Takahashi, Y, Iemura, H, Yanagawa, S, Hibi, M (2004). "Shaking table test for frictional isolated bridges and tribological numerical model of frictional isolator," *13th World Conference on Earthquake Engineering*, Vancouver, Canada

Taylor, AW and Igusa, T (2004). *Primer on seismic isolation,* 1st Ed., American Society of Civil Engineers, Virginia

Thakkar, SK and Maheshwari R (1995). "Study of seismic base isolation of bridge considering soil structure interaction", *Third Int. Conf. on Recent Advances in Geotechnical Earthquake Engineering and Soil Dynamics*, Univ. of Missouri-Rolla, Rolla, Missouri, Vol. 1, 397-400

Tsopelas, P and Constantinou, MC (1996). "Experimental study of FPS system in bridge seismic isolation," *Earthquake Engineering and Structural Dynamics,* 25, 65-78

Turkington, DH, Cooke, N, Moss, PJ and Carr, AJ (1989). "Development of design procedure for bridges on lead-rubber bearings", *Engineering Structures*, Vol. 11, 3-8

Tyler, RG (1991). "Rubber bearings in base-isolated structures – a summary paper," *Bulletin of the New Zealand National society for Earthquake Engineering*, 24, 251-274

Tyler, RG and Robinson, WH (1984). "High-strain tests on lead-rubber bearings for earthquake loadings," *Bulletin of the New Zealand National society for Earthquake Engineering*, 17(2), 90-105

Vlassis, AG and Spyrakos, CC (2001). "SIB piers on shallow soil stratum with soil-structure interaction," Computers and Structures, 79, 2847-2861

Warn, GP and Whittaker, AS (2004). "Performance estimates in SIB structures." *Engineering Structures,* 26, 1261-1278

Yashinsky, M and Karshenas, MJ (2003). *Fundamentals of seismic protection for bridges,* 1st Ed., Earthquake Engineering Research Institute, California

Yashinsky, M (1998). "Performance of bridge seismic retrofits during Northridge earthquake," *Journal of Bridge Engineering*, 3(1), 1-14

Zayas, VA and Low, S (1999). "Seismic isolation for extreme cold temperatures," *8th Canadian Conference on Earthquake Engineering,* Canadian Association for Earthquake Engineering, Vancouver, 391-395

Zayas, VA and Low, SS, and Mahin, SA (1987). *The fps earthquake resisting system experimental report*, Report No. EERC 1987-01, University of California, Berkeley

VITA

Murat Eröz was born on November 3, 1980 in Susurluk, Turkey. He earned a B.S. degree in Civil Engineering from Istanbul Technical University, Istanbul, Turkey in 2002. He earned an M.S. degree in 2003 from the Structural Engineering, Mechanics, and Materials group of Civil Engineering, Georgia Institute of Technology. He continued to pursue a Ph.D. degree in the same department. His major concentration was in the area of earthquake engineering and seismic isolation of structures, with a minor in Structural Mechanics.